INDIAN INSTITUTE OF SCIENCE EDUCATION AND RESEARCH, PUNE (IISER-PUNE)

DOCTORAL THESIS

Hierarchical And Synergistic Self Assembly of Wormlike Micelle-Nanoparticle System: A Computational Investigation

---

Author:
Mubeena Shaikh

Supervisor:
Dr. Apratim CHATTERJI

A thesis submitted in fulfilment of the requirements for the degree of PhD.

in the

Computational Soft Matter Group
Department Of Physics

22-11-2019

Certificate

This is to certify that this dissertation entitled "Hierarchical And Synergistic Self-Assembly of Wormlike Micelle-Nanoparticle System: A computational Investigation" is submitted towards the fulfilment of the PhD degree programme at the Indian Institute of Science Education And Research, Pune, represents the original work carried out by Mubeena Shaikh, IISER-Pune, under the supervision of Dr Apratim Chatterji, Associate Professor - Physics, IISER-Pune, during the academic year 2019.

Name of the supervisor: **Dr. Apratim Chatterji**

Signature of the supervisor:

Declaration Of Committee Members

WE, THE UNDERSIGNED MEMBERS OF THE COMMITTEE HAVE APPROVED THIS DOCTORAL THESIS,

---

Hierarchical And Synergistic Self Assembly of Wormlike Micelle-Nanoparticle System: A Computational Investigation

Author:
Mubeena Shaikh

Supervisor:
Dr. Apratim CHATTERJI

Department Of Physics

INDIAN INSTITUTE OF SCIENCE EDUCATION AND RESEARCH, PUNE (IISER-PUNE)

Committee members

Dr. Guruswamy kumaraswamy (Polymer science and engineering division, NCL, Pune) _____

Dr. Arijit Bhattacharya (Physics deparment, IISER-Pune) _____

Dr. Apratim Chatterji (Physics department, IISER-Pune) _____

_____ _____

Head of the department Head of the Institute

22-11-2019

Declaration of Authorship

I, Mubeena Shaikh, declare that this thesis titled, "Hierarchical And Synergistic Self Assembly of Wormlike Micelle-Nanoparticle System: A Computational Investigation" and the work presented in it are my own. I confirm that:

- This work was done wholly or mainly while in candidature for a research degree at this University.
- Where any part of this thesis has previously been submitted for a degree or any other qualification at this University or any other institution, this has been clearly stated.
- Where I have consulted the published work of others, this is always clearly attributed.
- Where I have quoted from the work of others, the source is always given. With the exception of such quotations, this thesis is entirely my own work.
- I have acknowledged all main sources of help.
- Where the thesis is based on work done by myself jointly with others, I have made clear exactly what was done by others and what I have contributed myself.

Signed:

Date: 22-11-2019

"Without data you are just another person with an opinion."

W. Edwards Deming

Indian Institute Of Science Education And Research, Pune (IISER-Pune)

Abstract

Dr. Apratim Chatterji
Department Of Physics

Doctor of Philosophy

Hierarchical And Synergistic Self Assembly of Wormlike Micelle-Nanoparticle System: A Computational Investigation

by Mubeena Shaikh

We use a Wormlike micelle model that uniquely gives us the control parameter to change its excluded volume. We show that the model successfully captures the characteristic behaviour of the Wormlike micellar system. Using the Monte Carlo technique, the model Wormlike micellar system is observed to undergo an isotropic-nematic transition. We also investigate the self-assembly of model nanoparticles inside the matrix of model equilibrium polymers (or matrix of Wormlike micelles) as a function of the polymeric matrix density and the excluded volume parameter between polymers and nanoparticles. In this thesis, we show morphological transitions in the system architecture via synergistic self-assembly of nanoparticles and the equilibrium polymers by employing Monte Carlo simulations. In synergistic self-assembly, the resulting morphology of the system is a result of the interaction between both nanoparticles and the polymers, unlike the polymer templating method. We report the morphological transition of nanoparticle aggregates from percolating network-like structures to non-percolating clusters as a result of the change in the excluded volume parameter between nanoparticles and polymeric chains. In parallel with the change in the self-assembled structures of nanoparticles, the matrix of equilibrium polymers also shows a transition from a dispersed state to a percolating network-like structure formed by the clusters of polymeric chains. We show that the shape anisotropy of the nanoparticle clusters formed is governed by the polymeric density resulting in rod-like, sheet-like or other anisotropic nanoclusters. It is also shown that the pore shape and the pore size of the porous network of nanoparticles can be changed by changing the minimum approaching distance between nanoparticles and polymers. We provide a theoretical understanding of why various nanostructures with very different morphologies are obtained.

Acknowledgements

I would like to express my sincere gratitude to the vibrant research environment and facilities provided by IISER-Pune, India. I acknowledge the use of the computer cluster provided by Nano-Science unit in IISER-Pune, funded by DST, India by Project No. SR/NM/NS-42/2009 and the Yuva Cluster provided by National Param Super Computing Facility (NPSF), CDAC, Pune, India.

My sincere acknowledgement to Dr. Apratim Chatterji for guiding me to learn computational techniques at the start of my PhD. I also thank my guide for his non-veg parties, Diwali sweets and biryanis and kebabs.

I am very thankful for the helpful discussions with Dr. Guruswamy Kumaraswamy, Dr. Arijit Bhattacharya and Dr. Deepak Dhar and their insightful comments, support and encouragement.

I would like to acknowledge that my greatest source of all kind of help, information, guidance and my PhD lifeline is "Google" along with the all-time internet facility by IISER-Pune without which I would not have completed this work.

My special thanks for all the help in my hard times from the department faculties, the PhD monitoring committee Dr. Bhas Bapat, Dr. Sudarshan Ananth, Dr. Aparna Deshpande and Dr. Umakant Rapol, the chair and the co-chair of the department of physics Dr Sunil Mukhi and Dr. MS Santhanam, the dean of doctoral studies Dr. Girish Ratnaparkhi and Dr. Amit Hogadi, the dean of graduate studies Dr. G Ambika, the director IISER-Pune Dr. K N Ganesh and my Research advisory committee member Dr. Arijit Bhattacharya. I am also thankful to Prabhakar Anagare, Dhanashree and Kalpesh for their occasional help.

I thank my colleagues and friends in IISER-Pune for giving me the life-long memories of the journey of my PhD.

Finally, I would like to thank all these people for teaching me the fact that in any corner of the world, any country, any society and any community, people with humanity are always in majority. This is what has revitalized my courage to further explore the world with the same zeal as in my school days.

Contents

List of Figures

Chapter 1

Introduction

Colloid, polymers, surfactants and their mixtures form the part of the soft matter that is prevalent throughout our day to day life. Food products like milk, butter mayonnaise, cosmetic products and household products from detergent to utensils made up of polymer composites, petrol and drug industries are full of the examples of soft materials (Bartlett, 1998). The forces of interactions involved in soft matter are often weak, non-covalent, of the order of k_BT and entropic in nature (Escobedo, 2014). Soft matter is memory forming, consists of active particles, shows characteristics far from equilibrium, form experimentally observable patterns at mesoscopic length scale, dissipative and entropic in nature. These are some of the characteristics of soft matter that show that how a system created from large constituents of particles behaves interestingly differently from the "hard matter" composed of atoms and molecules (Nagel, 2017). These systems have gained a tremendous amount of attention of researchers from physics, chemistry, biology and interdisciplinary fields alike due to their extensive use, interesting and complex behavior and capabilities to engineering novel materials by employing Self-Assembly to form ordered structures. Self-assembly, had a long journey from its earliest work in 1935 by Irvin Langmuir and Katherine B. Blodget (Langmuir, 1935), to Onsager's seminal paper highlighting the role of entropy in self-organization (Onsager, 1949), to its evolution as one of the most promising approaches for the fabrication of nanostructures (Ozin et al., 2009a). Self-organization in the soft matter is not only important for nanofabrication industry but attracts researchers from diverse fields like physics of phase transition, defects and questions forming fundamental interests of scientific communities. Because of their versatility, relatively inexpensive production and capability to process under mild conditions of temperature and pressure, soft matters are increasingly being exploited in advanced technological applications.

Colloids are the particles in the range of a few nanometres to micrometres in size which exhibit a high surface to volume ratio or more precisely a high surface to mass ratio (Schramm, 2002) inducing a crucial behavior known as Brownian motion, the discovery of which dates back to 1827 by Scottish botanist Robert Brown [7,8]. Brownian motion remained unexplained until 1905 when Einstein published a paper explaining it as a result of bombardment by water molecules leading to indirect evidence of the existence of atoms and molecules[8] and helping in understanding the then puzzling transport phenomena (Bird, 2004). The Brownian motion allows particles to explore the available phase space and interact with each other (Lionberger and Russel, 1999) leading to the formation of phases like solid, liquid, gas and their coexisting phases which are analogous to the phases shown by atomic and molecular systems (Bianchi, Blaak, and Likos, 2011). Moreover, the mesoscopic scale behavior and relatively slow dynamics facilitate the observation of colloidal systems in a laboratory using light scattering microscopy techniques at trackable time scales

which is otherwise difficult for the atomic or molecular systems. Thus colloidal systems are great model systems for foundational and groundbreaking experiments in equilibrium and non-equilibrium physics owing to their accessible length and time scales (Poon, 2004). Mixing colloids with other systems like polymers or surfactants multiply the available phase space and generate entirely new and fascinating properties and phase behavior (Tuinier et al., 2008; Jayalakshmi and Kaler, 1997; Bolhuis and Frenkel, 1994; Kooij, Vogel, and Lekkerkerker, 2000; Lajovic and Jamnik, 2009).

Polymers are in use from ancient times. The ancient Mayans used rubber tree extract to make balls (Hosler, Burkett, and Tarkanian, 1999; STAHL, 1999). Researchers have persistently tried to improve the performance of polymeric materials to optimize for industrial applications. The vulcanization of rubber to produce crosslinking polymers by Goodyear in 1839 improved its performance ("A Short History of Polymer Science"). In 1907 First synthetic plastic was made known as Bakelite. After the establishment of polymers as long chains made up of monomeric repeating units by Nobel laureate Hermann Staudinger, a series of polymeric materials came into the picture. In 1927 Polyvinyl chloride (PVC), Polystyrene in 1930, nylon in 1938 and polyethylene in 1941 (Feldman, 2008).

Then researchers realized that combining polymers with other materials can multiply material performance. Thus Kevlar was invented in 1965, which is a fibre reinforced polymer with extreme hardness and excellent temperature resistance (Kwolek, Mera, and Takata, 2002). Polymers and polymer-based composites dominated the use of steel in household products by 1980s. The invention of these polymer composites has shaped the whole economy of various industries. However, these minerals and other inorganic materials were only thought as 'fillers' until a landmark discovery by Toyota in 1992 regarding the preparation of polyamide 6/ organophilic clay nanoparticles composite with its super-enhanced properties. This new material was reported to be having 40% increase in rupture tension, 68% in Young's modulus, 126% in flexural modulus and enhanced heat distortion temperature in comparison to pure polymers (Duleba, Spišák, and Greškovič, 2014). This discovery gave the field of nanotechnology a new direction followed by an era of intensive theoretical and experimental investigations in search of an explanation for the unimaginably enhanced properties of polymer nanocomposites which still a matter of research.

Compared to their micro counterparts, nanoparticles have a large surface to volume ratio. Enhancement in microcomposites are achieved at the expense of optical clarity, surface gloss and increased weight due to high filler volume fraction, while due to a high surface to volume ratio of nanoparticles the material enhancement can be achieved at a very low volume fraction of fillers in nanocomposites ($< 20\%$) (*Nano Composite Network, Technology Review-Nanocomposite.*). As a single gram of nanoparticles contains an enormous number of particles (10^{20}), the role played by a small number of nanoparticles is expected to be much better than a large amount of micron-sized particles. Thus increment in the interfacial region due to the high surface area of nanoparticles is thought to play a vital role in nanocomposite materials enhanced properties. Most of the theoretical studies on reinforcement mechanisms are based on micromechanical models which relate the mechanical properties with the filler volume fraction and shape (Y Gao, 2017). However, these models are unable to capture the nanoscale constituents, increasing the complexity and decreasing the accuracy of the analysis. Though literature presents numerous toughening mechanisms like cavitation, shear yielding, crack pinning, crack deflection, crack-bridging-pull-out, nanoparticle mobility, and much more, the information available is still non-extensive to come to a consensus (Zeng, Yu, and Lu, 2008; Coleman et al., 2006).

With the development in the field of nanotechnology, the focus of researchers was to 'disperse' nanoparticles inside the polymeric matrices (Mackay, 2006; Kashiwagi et al., 2007). Therefore most of the studies were concentrated on developing a method to modify nanoparticle interactions within themselves and with polymers to stabilize their dispersion in the matrix (Chandran et al., 2014). However, an important discovery by Mobil Oil Corporation changed the whole scenario of nanotechnology and brought a renaissance to the field of nanofabrication(Zhao, Lu, and Millar, 1996).

During the 1980s, zeolites which are molecular size porous materials were widely used in oil and petroleum industries as sieves for various filtering processes (Shi et al., 2015). However, the industry was challenged by the demand for larger pore size and perfectly ordered porous materials(Ohayon et al., 2001). In search of this, Mobil Oil Corporation created the family of new materials. One member of the family named MCM-41 was reported to be produced by the method of templating by employing wormlike micellar matrix as templates for casting nanoporous materials. This approach in no time became popular among researchers due to its simplicity, low cost and better control over tailoring the desired dimension and shape. Thus, giving rise to a huge kick to the nanofabrication industry with the evolution of a 'Bottom-up' approach (Liedl, 2011).

A wide range of polymeric matrices and their blends were explored to produce a myriad of nanostructures with a variety of morphologies (Lalander et al., 2010; Mezzenga, 2003; Choi et al., 2007; Ikkala and Brinke, 2004). Diblock and triblock copolymers are among the most explored systems due to their interesting and complex phases (Jain and Bates, 2003; Pochan et al., 2004). Various techniques were used to modify their interactions in order to 'guide' nanoparticles for their selective deposition in polymeric matrices to get the desired structure. The ordered polymeric matrices thus for long were used as templates by using external fields and chemical reactions for selective deposition of nanoparticles (Guarini et al., 2002; Bruinink et al., 2006). However, some of the simulations and theoretical studies(like Balasz et al. 2002) (Lee et al., 2002) led the attention to the idea of self-assembly of ordered structures via entropic interactions (Fenniri et al., 2002; Yodh et al., 2001; Whitesides, 2002).

Despite the success of theories of Asakura Oosawa (Asakura and Oosawa, 1954), Onsager (Onsager, 1949), Lekkerkerker (Lekkerkerker et al., 1992a), Gast et al. (Gast, Hall, and Russel, 1983b; Gast, Hall, and Russel, 1983a) etc., the theoretical results are full of approximations and limitations like low concentration and polymer to colloid size ratio and ideal chain behavior (Poon, 2002; Lekkerkerker et al., 1992a; Dijkstra et al., 2006; Chervanyov and Heinrich, 2009). At higher concentrations and longer polymers, these systems show non-equilibrium behaviour due to entanglement, local arrest, caging, jamming and other effects. On the one hand, these theories are unable to handle the complexity of the colloid-polymer mixtures, and the micromechanical models of polymer nanocomposites fail to capture the nanoscale constituents of the system, On the other hand, the experimental techniques are limited by the low resolution and experimental costs. In such a scenario, computational techniques serve as a bridge between the two methods and are able to simulate some of the systems quite successfully. Nonetheless, these techniques are also hindered by computational time and costs and especially difficulty in reaching equilibrium states for denser systems due to locally arrested states.

From Asakura and Oosawa's interaction and Onsager's 1949 (Onsager, 1949) seminal paper to the jammed and arrested states, colloid-polymer mixtures/polymer

nanocomposites had a long journey actively contributing and building up the concepts in soft matter. It has been more than eight decades that the nanoparticles were added to polymers and still it forms an active research field in search of a lot of unanswered questions. A myriad of nanomaterials was generated using these polymeric matrices of which diblock and triblock copolymers are the prominent examples. However, hardly there exist attempts to explore and understand the behavior of wormlike micellar composites. Despite its remarkable rheological properties and semiflexibility and behavior that is non-existent to a polymeric matrix, this system is lacking the appropriate investigations. This thesis is an attempt to explore the system of wormlike micelles and nanoparticles mixture and get a direction for further studies to understand it.

Before describing our system and presenting the results, let us have a basic overview of colloids, polymers colloid-polymer mixture, wormlike micelles and use of polymeric matrices for nanofabrication.

1.1 Colloids

Francesco Selmi in 1845 described the first example of colloidal particles as a turbid 'pseudo solution' of silver chloride and Prussian blue giving birth to a new branch known as colloidal science(Guareschi, 1911). However, it is Thomas Graham, who in 1861 for the first time in the world used the word 'colloid' while describing the 'pseudo solution' prepared by Selmi 15 years before (Vincent, 2012). The research on colloidal science has eluded scientists for more than ten decades and is still an active area searching answers for questions of fundamental interests.

As introduced in the first paragraph of this chapter, colloids are characterized by a large surface to volume ratio and leading its behavior by surface interactions. In a solution, colloidal particles are constantly in contact with solvent molecule colliding and exchanging momentum resulting in a random zig-zag path referred to as Brownian motion. This allows them to explore the available phase space with an average translational kinetic energy of 3/2KT. On increasing concentration, they come into contact with each other and tend to phase separate if their aggregation energy is higher than the thermal energy otherwise remain dispersed. The phase behavior of colloidal systems is quite analogous to atomic and molecular systems, and hence there is an immense interest in it (Goodwin, 2004). As the colloidal particles tend to phase separate, in most of the practical situations, it is often required to stabilize a colloidal dispersed solution. Therefore, their surface is often modified in order to form a stable solution. They are either charged (Pham, Fullston, and Sagoe-Crentsil, 2007), surface modified or coated with other chemicals or grafted with polymers for this purpose (Ruckenstein and Li, 2005). This modification changes their interaction and behavior. In the following sections, we briefly go through the interaction between colloidal particles and their behavior.

1.1.1 Interaction between uncharged colloidal particles

Electrons in an atom or molecule are always in motion as suggested by quantum physics. There exists a finite probability of creation of an electronic charge distribution leading to an imbalance of charge leaving the body polarized. Therefore even in the absence of a permanent dipole on a body, there might be an instantaneous dipole moment created by its electronic charge distribution or due to the charge distribution in neighboring bodies. The effective interaction between two particles due

to permanent or induced dipoles is known as Van Der Waal's (VDW) interaction. VDW interaction consists of the following contributions, (Hamaker, 1937)

Keesome interaction: dipole-dipole interaction
It is the interaction between two permanent dipoles.

Debye interaction: dipole-induced dipole interaction
It is the contribution from the interaction between a permanent dipole and an induced dipole.

London dispersion interaction: induced dipole-induced dipole interactions
It arises from the interaction between instantaneously induced dipole moments.

In most of the cases, dipolar interactions are attractive. Therefore VDW's interaction is also an attractive interaction but weaker than the ionic and covalent bondings. By assuming these interactions to be additive to a first approximation, Hamaker derived an expression for the interaction energy between two spherical particles of radius a, separated by a distance r as (Shaw, 1980),

$$V_\alpha = -\frac{A}{12}\Big\{\frac{1}{x(x+2)} + \frac{1}{(x+1)^2} + 2\ln\frac{(x(x+1)}{(x+1)^2)}\Big\}, \tag{1.1}$$

where, $x = r/(2a)$ and A is known as Hamaker constant.

At large distances, in the limit of $x \to \infty$, the potential shows r^{-6} behavior. While at short distances when $x << 1$, the expression becomes $V_a = -Aa/(12d)$. Therefore at shorter distances potential varies as the inverse of the distance between the particles creating an attractive long-range interaction which is responsible for the aggregation of colloids. Including Pauli's exclusion principle gives a steep increase in the potential at very short distances. The interaction between two uncharged colloids is often expressed as an empirical relation for a spherical particle of radius σ and attractive potential depth ϵ as follows,

$$V(r) = 4\epsilon\Big[(\frac{\sigma}{r})^{12} - (\frac{\sigma}{r})^{6}\Big]. \tag{1.2}$$

This is known as Lennard-Jones potential and extensively used in computational modeling and theoretical studies. The potential is highly repulsive at shorter distances manifesting Pauli's exclusion principle and have a long-range attractive tail for higher distances as shown in Figure 1.1.

In many real applications, colloidal dispersions are needed to be stabilized against coagulation which is done by various methods like surface modification by charging or coating with some other material or grafting with polymers (Napper, 1977). The modifications of colloidal surfaces modify the interaction between them generating different phase behaviors. In the following sections, we have a brief introduction to the change in colloidal interactions in the case of surface modifications.

1.1.2 Interaction between charged colloids

When charged particles are dispersed in a solution, it derives the neighboring counterions in the solution to get adsorbed on the colloidal particles creating a layer. This layer modifies the interaction between two charged colloids. The simplest model that attempted to explain the modified interaction in the case of charged colloidal

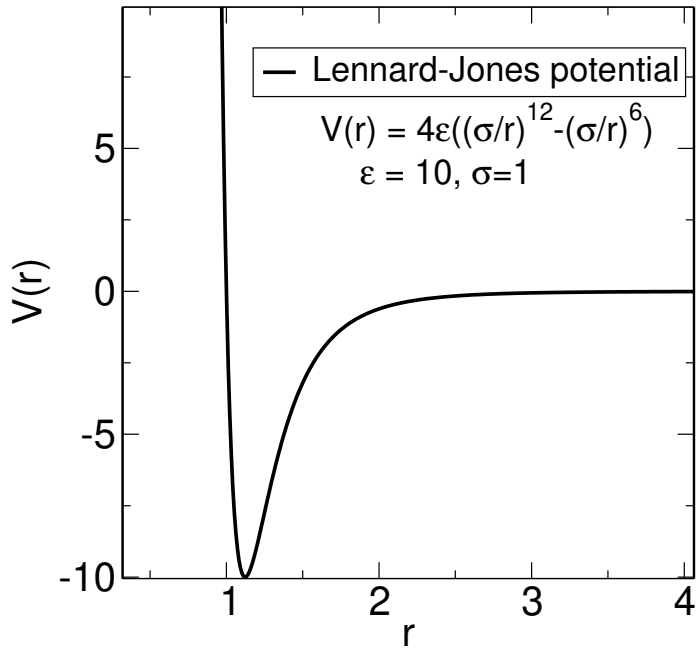

FIGURE 1.1: Plot of Lennard-Jones potential.

surfaces was first given by Helmholtz (Helmholtz, 1853).

Helmholtz model:

In this model, the counterions in the solution get adsorbed by the charged colloids neutralizing them. It creates a situation like a capacitor, as shown in Figure 1.2.

If $\rho(z)$ is the charge density of the surface at a distance z from the surface, an electric field is generated by these charges which can be given by Poisson's equation as follows,

$$\frac{dE}{dz} = \frac{1}{\epsilon\epsilon_0}\rho(z), \tag{1.3}$$

where, ϵ and ϵ_0 are the dielectric permittivities of the medium and vacuum respectively. The relation between the electric field E and the corresponding electric potential ψ is given by,

$$E = -\frac{d\psi}{dz}. \tag{1.4}$$

Therefore, the Poisson's equation can be written as,

$$\frac{d^2\psi}{dz^2} = \frac{1}{\epsilon\epsilon_0}\rho(z). \tag{1.5}$$

However, the electric field in the area between the two surfaces is constant as there is no charge in between them. Let E_0 and V_0 be the constant electric field and potential between the two surfaces. Integrating above expressions, we can write,

$$E_0 = \frac{\sigma}{\epsilon\epsilon_0}, \tag{1.6}$$

OR

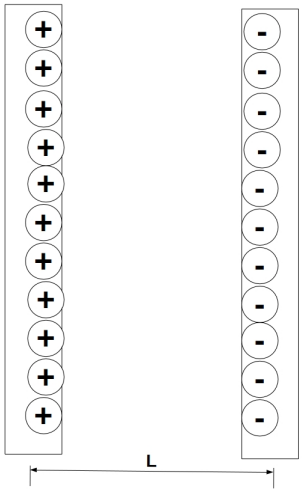

FIGURE 1.2: Helmholtz model of charged colloids.

$$\frac{\sigma}{\psi} = \frac{\epsilon\epsilon_0}{L}. \tag{1.7}$$

Assuming,

$$\frac{\epsilon\epsilon_0}{L} = C_s, \tag{1.8}$$

where, C_s is known as the specific capacitance. We can write,

$$\frac{\sigma}{\psi} = C_s. \tag{1.9}$$

Thus the surface potential of the colloids is proportional to the surface charge density as in the case of a capacitor. However, this theory is unable to explain the dependence of the interaction on the ionic strength, which is a big drawback.

This model is corrected and improved by Gouy and Chapman.

Gouy-Chapman model:
Helmholtz model does not capture the effect of the thermal energy of counterions. Gouy and Chapman (Torrie and Valleau, 1982; Gouy, 1913) corrected it by taking into account the equilibrium distribution of the adsorbing ions hence allowing them to diffuse in the area between the two charged surfaces as shown in Figure 1.3.

Therefore the charge distribution in this case becomes,

$$\rho(z) = qc_B\left[e^{-q\psi(z)/k_BT} - e^{+q\psi(z)/k_BT}\right], \tag{1.10}$$

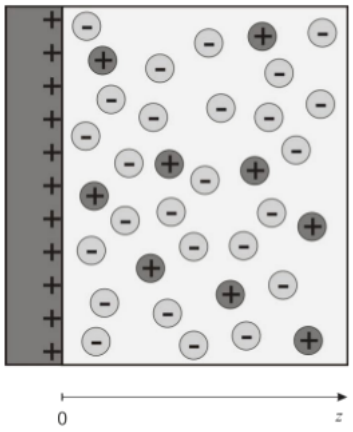

FIGURE 1.3: Gouy-Chapman model of charged colloids with a diffuse charged layer.

where, c_B is the bulk ionic concentration and q is the ionic charge. Therefore the Poisson's equation can now be modified as,

$$\frac{d^2\psi}{dz^2} = \frac{qc_B}{\epsilon\epsilon_0}\left[e^{-q\psi(z)/k_BT} - e^{+q\psi(z)/k_BT}\right]. \tag{1.11}$$

This is known as the Poisson-Boltzmann equation. Using Taylor series, this can be reduced to following approximate expression,

$$\frac{d^2\psi}{dz^2} = \kappa^2\psi, \tag{1.12}$$

where,

$$\kappa^2 = \frac{2q^2c_B}{k_BT\epsilon\epsilon_0}, \tag{1.13}$$

and κ^{-1} is known as Debye screening length. It defines the distance over which the potential decreases by an exponential factor. Thus it essentially defines the thickness of the ionic layer. This approximate form of Poisson-Boltzmann equation is known as Debye-Huckle equation and has a solution of the form of,

$$\psi = \psi_0.e^{-\kappa z}. \tag{1.14}$$

However, for highly charged surfaces this approximation is not valid and Poisson-Boltzmann equation has to be used which leads to the following solution,

$$\psi(z) = \frac{4k_BT}{q}\tanh\left(\frac{q\psi_0}{4k_BT}\right)e^{-\kappa x} = \psi_{eff}e^{-\kappa x}, \tag{1.15}$$

where,

$$\psi_{eff} = \frac{4k_BT}{q}\tanh\left(\frac{q\psi_0}{k_BT}\right). \tag{1.16}$$

Both the solution of Debye-Huckle and Poisson-Boltzmann equation is shown in Figure 1.4.

Stern double layer:

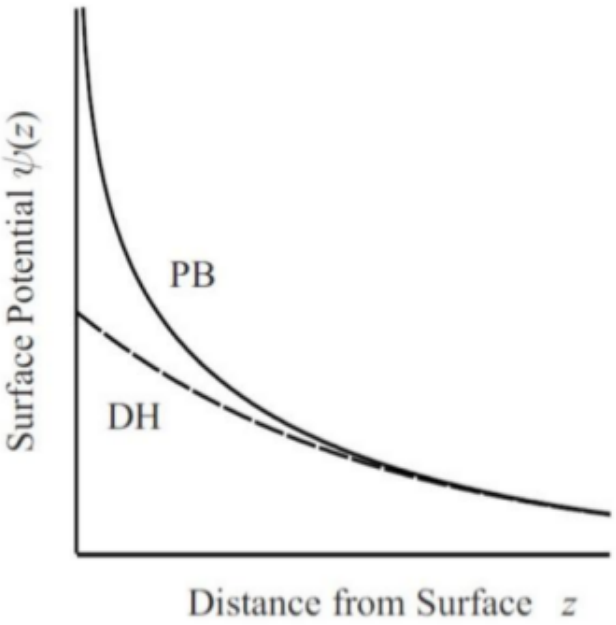

FIGURE 1.4: Solution to Debye-Huckle and Poisson-Boltzmann equations.

Improving over the Gouy-Chapman model, Stern formed a double layer theory by combining the Helmholtz and Gouy-Chapman models (Stern, 1924; Ohshima, Healy, and White, 1982). Thus in Stern model, the charged colloidal surface is directly adsorbed by immobile counterions interacting via Coulomb interaction forming an inner part of the layer, and there exist a diffuse layer of Boltzmann counterions forming the second layer. As seen in the above two models, the potential in the inner layer decreases quite fast varying linearly with distance while in the diffuse layer, it varies exponentially, decreasing slowly with the distance. This is explained in Figure 1.5

When two such charged particles come close to each other, then the double layers overlap with each other. The counterions between the gap are forced to stay within the small volume between the two surfaces. This gives rise to a pressure equal to the difference between the pressure of the film between the two surfaces and the bulk. A detailed treatment of the problem based on Gouy-Chapman-Stern theory is carried out by Healy et al. assuming that the adsorption equilibrium is maintained as the two layers overlap.

For spherical particles of radius a, stern potential ψ_d and shortest distance of approach H, two distinct cases arise,

Case I: If the surface charge results from the adsorption of ions then the surface potential remains constant and is given by,

$$V = 2\pi\epsilon_0\epsilon a{\psi_d}^2 \ln\left(1 + exp[-\kappa H]\right). \tag{1.17}$$

Case II: If the surface charge is a result of the ionization of the groups on the particle surface then the surface charge density remains constant and the potential

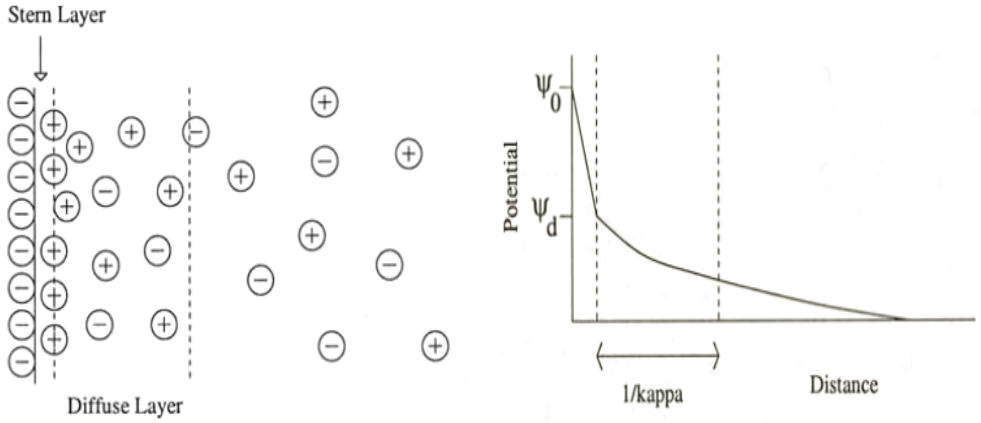

FIGURE 1.5: (left)Stern model of the double layer. (Right) The corresponding potential varying with distance from the surface.

is given by,

$$V = -2\pi\epsilon_0\epsilon a{\psi_d}^2 \ln\left(1 - exp[-\kappa H]\right). \tag{1.18}$$

In both the above cases, in the limits of $exp[-\kappa H] >> 1$, i.e. for a small electric double layer overlap the equations reduces to,

$$V = 2\pi\epsilon_0\epsilon a{\psi_d}^2 exp[-\kappa H]. \tag{1.19}$$

However, the above treatment is based on the assumption of equilibrium of the adsorbed ionic layer which was shown to be invalid by Overbeek (Overbeek, 1977) as the potential profile of each surface will be affected by the presence of the other charged surface. Therefore the actual situation lies somewhere in between the constant potential and constant charge approximations.

1.1.3 The Derjaguin-Landau and Verwey-Overbeek (DLVO) Theory

During the 1940s, two Russian scientists Derjaguin-Landau (Derjaguin, 1941) and two Dutch scientists Verwey-Overbeek (Verwey, Overbeek, and Overbeek, 1999) independently formulated a quantitative theoretical description predicting the stability of colloids. This theory states that the interaction potential energy between two charged colloidal particles is given by the sum of the two potentials. A short-range attractive Van Der Waal's potential arising from dipolar interactions and the other is the long-range repulsive double layer potential arising from the charge distribution on colloidal surfaces. Thus the total potential of a colloid in a solution can be written as,

$$V_{DLVO} = V_{VDW} + V_{EL}. \tag{1.20}$$

The Van Der Waal's potential gives rise to short-range, attractive energy varying as the inverse of the distance from the surface while the double layer potential induces a long-range, repulsive potential varying exponentially. At very short distances VDW potential is highly repulsive. Thus VDW potential is dominating at very short or long distances, while the Stern double layer interaction dominates at the intermediate distances giving rise to a secondary minimum as explained in Figure 1.6.

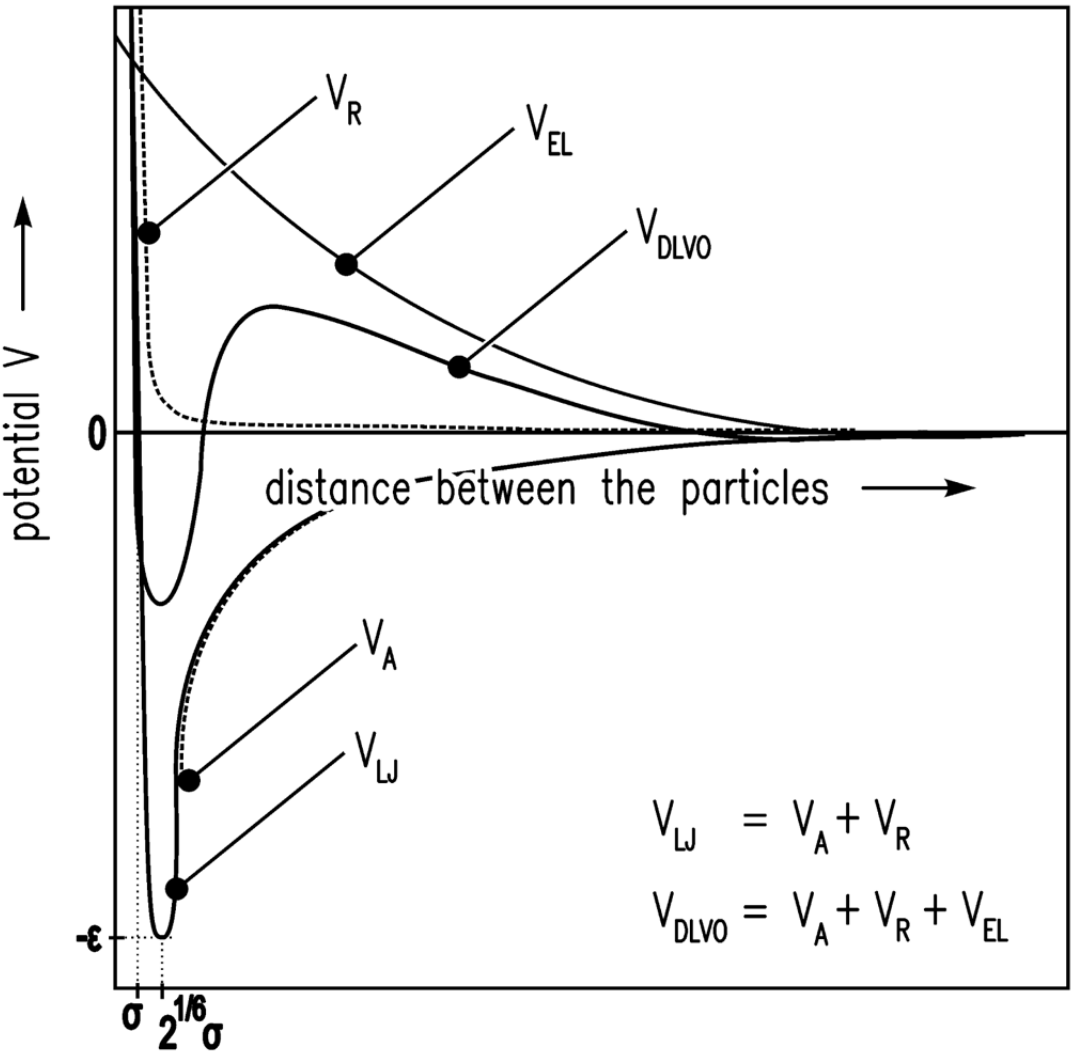

FIGURE 1.6: DLVO potential: A combination of Lennard-Jones potential V_{LJ} and Stern double layer potential V_{EL}. V_A and V_R represents the long-range attractive (due to dipolar interactions) and short-range repulsive (due to Pauli's principle) potentials. Reprinted with permission from the authors of (Sahabi and Kind, 2011)

Figure 1.6 shows three different graphs. One is Lennard-Jones potential V_{LJ} which the superposition of the repulsive part V_R coming from Pauli's exclusion principle and an attractive contribution V_A due to the dipolar interactions. The stern double layer potential is shown as the repulsive contribution part by V_{EL}. The sum of the VDW and double layer potentials is shown as the resultant V_{DLVO} potential giving rise to a primary minimum at a shorter distance and a secondary minimum at longer distances due to the dominance of the VDW potentials at these two distances. However, at intermediate distances, a positive potential barrier is created due to the dominant terms of electric double layer potential. The height of this potential barrier is crucial in deciding the colloidal dispersion stability, and it depends on the ionic strength and pH of the solution. When colloidal particles with high kinetic energy overcome this energy barrier, the primary minimum induces irreversible coagulation. While particle with low kinetic energy when approach each other are unable to cross the positive potential barrier, they can form an aggregation which corresponds to the secondary minimum of the V_{DLVO}. However, due to the very low depth of the secondary minimum, this aggregation induces a weak bonding between particles, hence making it reversible.

Thus, if K.E is the kinetic energy of the colloidal particle and U_{max} is the positive barrier height then,

if K.E > U_{max} $\rightarrow$ Irreversible aggregation $\rightarrow$ Coagulation

if K.E < U_{max} $\rightarrow$ reversible aggregation $\rightarrow$ Flocculation/dispersion

Stability of a solution now depends on the K.E of the colloidal particles. In the case of low K.E, to avoid the secondary minimum induced aggregation, a barrier can be created to this primary minimum by modifying solvent properties or by grafting polymers on colloidal surfaces, ensuring the stability of the colloidal dispersion.

Thus, DLVO theory was a breakthrough in colloidal science and was successfully able to explain the stability of the colloidal suspensions. Though DLVO theory cannot explain the coagulation properties in all colloidal systems as specific structural effects are not considered here which are tough to determine, it is still used extensively today even after 50 years of its development and has become a milestone in colloidal science.

There also exist other methods to stabilize the colloidal solutions like steric repulsion, surface coating, polymer grafting, etc. collectively known as steric stabilization methods. The following section introduces to the steric stabilization.

1.1.4 Steric stabilization

Often colloids are stabilized by grafting and coating their surfaces with polymers (Ruckenstein and Li, 2005). When two such polymer grafted colloids come close to each other, the polymer layers begins to overlap resulting in a higher concentration in between particles. This creates an unbalanced pressure pushing the colloids apart. Alternatively, the decrease in entropy due to the restriction of polymer configurations in the overlapped region creates a repulsion between colloidal particles.

One of the crucial parameter affecting the grafted polymeric interaction is temperature, depending on which, a solution can play the role of a good, bad or theta solvent. Steric stabilization works well in a good solvent where polymers prefer to remain near solvent molecules while it is ineffective in a poor solvent, making them collapse and form colloidal aggregates. Due to the coagulation process in

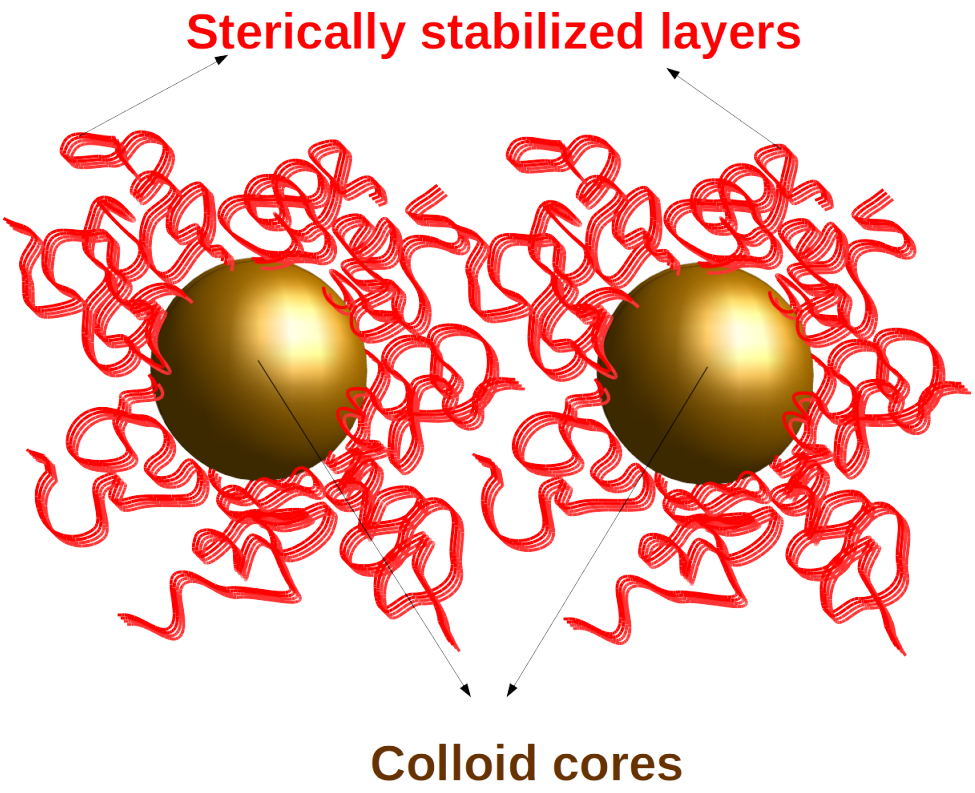

FIGURE 1.7: Steric stabilization: surface modification by grafting polymers.

charged colloids which is often irreversible, steric stabilization gives it an advantage over charged stabilization. Moreover, non-aqueous solutions cannot accommodate charge stabilization, unlike steric stabilization.

In order to provide a strong repulsion between two colloids, the grafted polymer ends are not only required to adsorb strongly on the colloidal surface but also need the other end to extend away from the colloidal surface. Therefore a homopolymer often fails to be a good surface graft and block copolymers are widely employed for this purpose. Due to large differences between the nature of polymeric interactions, grafting technique, kind of surface anchoring, etc., it does not have a generalized theoretical description. However, the repulsive interaction between two grafted polymers, when they approach each other, can be described by the repulsive force proposed by De Gennes (De Gennes, 1987) as follows,

$$F(D) = \frac{\beta k_B T}{s^3}\left[\left(\frac{2\delta}{D}\right)^{9/4} - \left(\frac{D}{2\delta}\right)^{3/4}\right], \tag{1.21}$$

where, D is the separation between the surfaces, δ the thickness of the polymer layer, k_B the Boltzmann constant, T the absolute temperature and s is the separation between the ends of the terminally attached polymer chains. The first term refers to the repulsive force due to the overlapping of polymers while the second term accounts for the stretching of polymers.

1.1.5 Colloidal phase behavior

The Phase transition is the extensively studied subject in Soft Matter over the last two decades, of which colloidal systems are the most outstanding example showing a rich phase behavior depending on the attractive and repulsive interactions. Hard sphere colloids form the simplest system to consider which mimics the phase behavior of atomic solids or liquids. After the Onsager's hard rod fluid theory, it was the theoretical prediction of hard-sphere crystallization by J.E Kirkwood and the first simulation observation of it by Wood and Jacobson (Wood and Jacobson, 1957) and Alder and Wainwright (Alder and Wainwright, 1957) more than 50 years ago that strengthened the idea of entropically driven phase ordering. For a hard-sphere fluid of radius a, the interaction between them are defined as,

$$V(r) = 0 : r > a, \tag{1.22}$$

$$V(r) = \infty : r < a. \tag{1.23}$$

Due to the infinite repulsion, the hard-sphere have vanishing internal energy, and their free energy F is determined by entropy S as,

$$F = -TS, \tag{1.24}$$

where, T denotes the absolute temperature. Thus hard-spheres play a role analogous to the ideal gas in understanding fluids, glasses and crystals, etc. There does not exist any exact equation of state for hard-spheres, but Percus-Yevic equations give a good representation of hard-sphere fluid (Smith and Henderson, 1970; Verlet and Weis, 1972). Their phase behavior was first studied in simulations where the crystalline state was a great surprise for scientists. It was only after establishing PMMA particles as nearly hard-sphere colloids, their system behavior was realized experimentally and confirmed the previous simulation results.(De Hek and Vrij, 1981; Edwards et al., 1984; Ilett et al., 1995; Pusey and Van Megen, 1986)

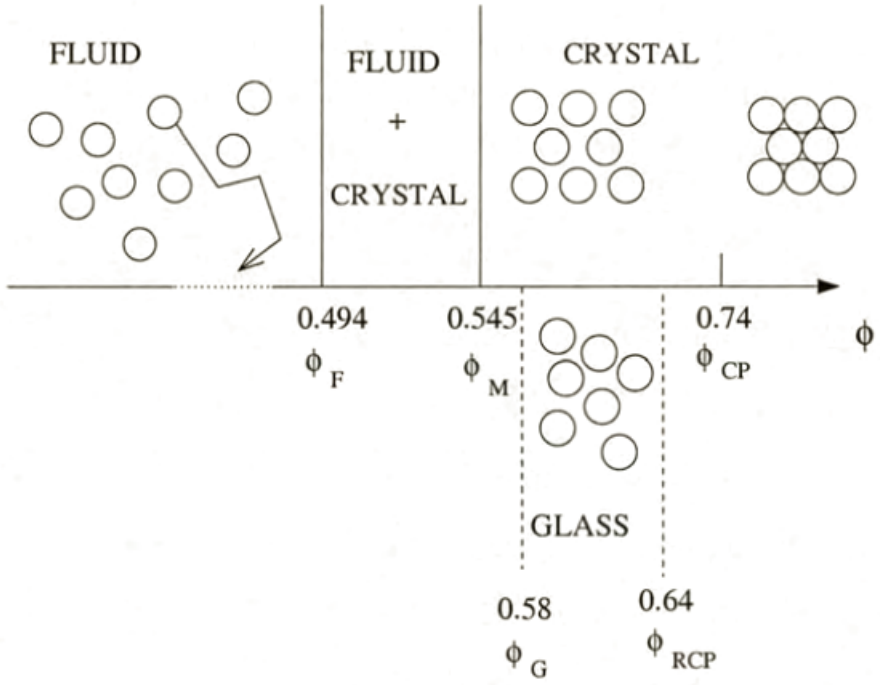

FIGURE 1.8: Phase diagram of a hard-sphere colloidal system as a function of their volume fraction. Adapted from (Brader, 2010).

Simulations of monodispersed hard (Wood and Jacobson, 1957; Hoover and Ree, 1968) sphere system shows that their behavior depends only on the dimensionless quantity ϕ, the volume fraction of the colloids given by,

$$\phi = N\frac{V_p}{V}, \tag{1.25}$$

where, N is the number of spheres in volume V, and V_p is the volume of a sphere. Figure 1.8 shows a schematic diagram for the phase behavior of hard-sphere colloids. As explained earlier, these systems are entirely entropically driven. The entropic term has two contributions competing with each other; the configurational entropy and free volume entropy. At higher densities, the increase in configurational entropy may lead to a large drop in free volume entropy by forming an arrested state. This state is relaxed by increasing the free volume entropy at the expense of configurational entropy. Thus at higher densities colloids tend to get crystallized. For colloidal systems with short-range or long-range attractive potentials, the enthalpic contribution increases the complexity leading to a rich phase behavior. The addition of an attractive long-range interaction leads to three-phase equilibria, while attractive short-range interactions result in metastable states for gas and liquid coexistence, maintaining the gas and crystal equilibrium. Figure 1.9 shows the colloidal phase behavior comparing the cases of purely hard-spheres, short-range attractive and long-range repulsive systems.A

At lower densities, hard-sphere colloids show fluid-like behavior diffusing freely and showing no long-range order. On increasing colloidal volume fraction to 0.494 and beyond, it enters into a coexisting phase of solid and fluid before solidifying as

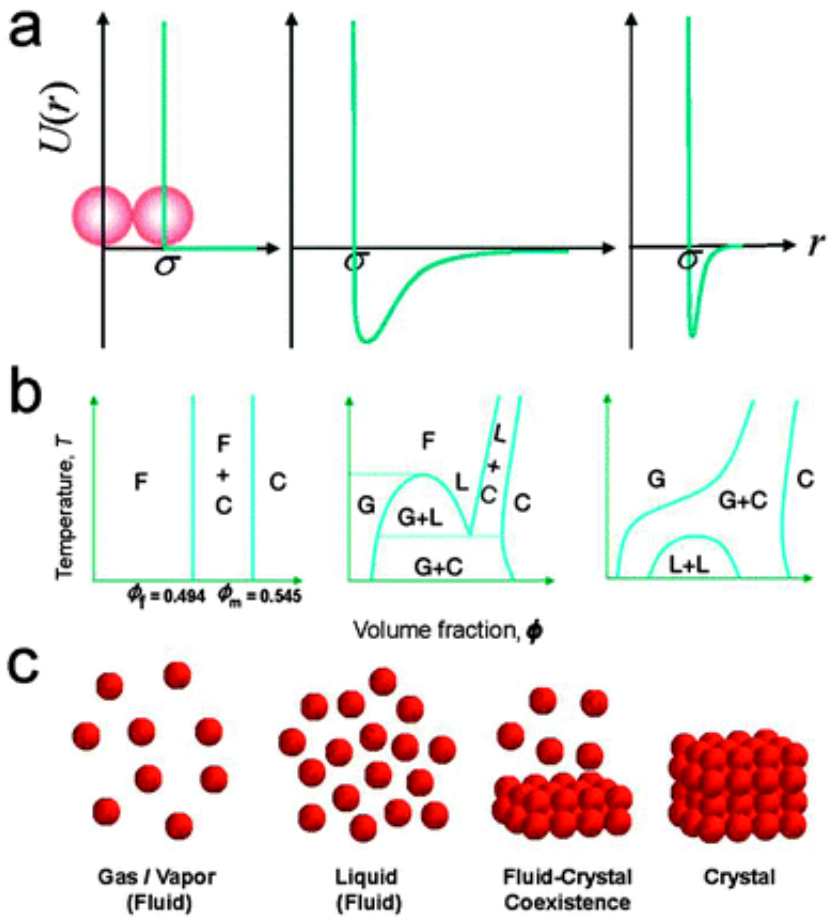

FIGURE 1.9: Phase diagrams in colloids. (a) Interactions between colloid particles. From left to right: hard-sphere interaction, long-range attraction, short-range attraction. (b) Left: in hard-sphere systems, only fluid (F) and crystal (C) phases exist. Middle: phase diagram of hard-spheres with long-range attractions, an analogue of atomic systems. Right: in cases where the attraction is short-range, as in protein systems (important in physiology), an equilibrium between gas (G) and crystal (C) is found, but the liquid (L)–liquid (L) transition becomes metastable. (c) Schematic representation of phases in colloids: gas, liquid, crystal (Zhang and Liu, 2014) - Reproduced by permission of The Royal Society of Chemistry [ref].

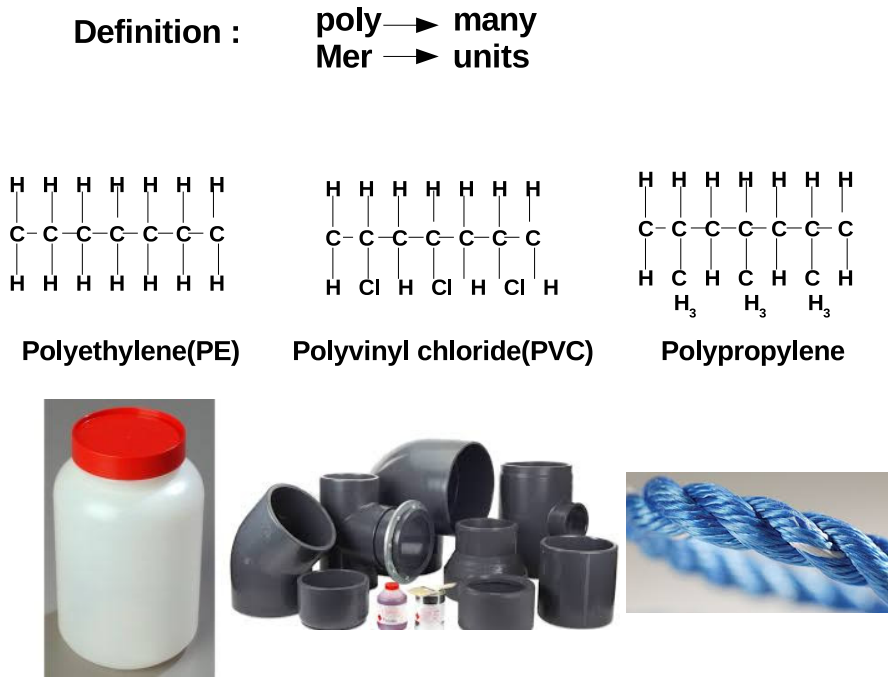

FIGURE 1.10: Polymers: examples

crystal beyond 0.545 volume fraction. On further increase in volume fraction, the packing of the crystal phase increases with the limiting value of maximum closed packing volume fraction of 0.74. There also exists a maximum random closed packing for the volume fraction of 0.64, but high-density states are not easy to get to the equilibrium states. They might get stuck in metastable states like a glassy state starts to form at the value of 0.58. Varying the colloidal interactions induce a variety of phase behavior (see Figure 1.9). Apart from interactions, many factors affect the colloidal phase behavior like polydispersity, electrolyte concentration, solution pH value, soft core interactions, etc.

1.2 Polymers

In today's modern world, polymers make up a significant part of our regular useful materials. The word Polymer is derived from two words, poly(many) and mers(units). It means a material created by many repeating units which are joined by covalent bonds. No other material has so much impact on our lives and industries as polymers. From household products to light-weight aviation materials and biological matters polymers form an integral part. Polymer physics spanning the history of more than 60 years now form the basis of varieties of problems in physics.

Our day to day life is full of polymeric materials, some of which are shown in Figure 1.10. Apart from plastic and polymer composite materials, some of the other major examples of polymers are:
Fatty acids : Chain of hydrocarbons
Polysaccharides : Chain of monosaccharide
Proteins : Chain of amino acids
RNA and Dna : Chain of Nucleotides

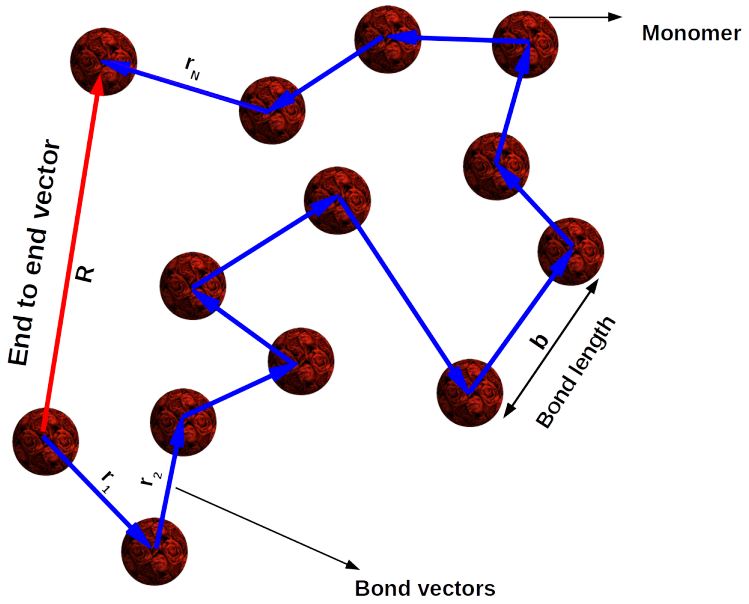

FIGURE 1.11: Polymers are represented as a random walk with the bond vectors $\vec{r_i}$ as their random steps. $\vec{R}$ is the end to end vector of the polymer.

There exists a huge variety of theories that allow studies of single atomic systems. Using the exact form of inter-particle potential, a pair correlation function can be determined from where all thermodynamic properties can be calculated. This is possible for atomic or diatomic systems. In the case of molecules, the presence of a huge number of parameters makes the equation difficult to handle, and the situation becomes out of control. Though increased complexity in the many-body system makes it impossible to arrive at a solution using current theories, there exist a limiting case of infinitely long chains(theoretically which are close to polymers) that can be handled using simple approximations. In a system consisting of long polymers, the probability that a randomly chosen monomer is an end monomer is very low. Assuming each polymeric segment to be situated somewhere in the middle of a chain simplifies the theoretical complexities drastically and gives access to a powerful technique known as the mean-field treatment. In the mean-field treatment, the polymer conformations are assumed to have an apriori probability distribution. The probability distribution of the end-end vector of the polymers is derived in the next section.

1.2.1 Ideal polymeric chain

Ideal polymers are the simplest model of polymers where the chains are represented by a random walk. This is shown in Figure 1.11 where, an ideal polymeric chain is having $N+1$ monomers linked by bonds of length b and characterized by their end-to-end distance expressed as,

$$\langle \vec{R}^2 \rangle = \langle \vec{R}.\vec{R} \rangle = \Big\langle \sum_{i=1}^{N} \sum_{j=1}^{N} \vec{r_i}.\vec{r_j} \Big\rangle, \tag{1.26}$$

where, $\vec{r_i}$ and $\vec{r_j}$ represents the bond vectors.

Since there exists no correlation between segments of ideal chains, therefore,

$$\langle {r_i}^2 \rangle = \langle \vec{r_i} \vec{r_j} \rangle = b^2, \tag{1.27}$$

$$\langle \vec{r_i}.\vec{r_j} \rangle = 0 (i \neq j), \tag{1.28}$$

Hence,

$$\langle \vec{R}^2 \rangle = Nb^2, \tag{1.29}$$

In one dimension, the number of ways of arriving at a distance x from origin after N steps of unit size is given by,

$$W(x, N) = \frac{N!}{n_+!\, n_-!}, \tag{1.30}$$

where, n_+ and n_- are the steps taken in forward and backward direction respetively. The total possible number of occurence of this trajectory is 2^N. Therefore, the probability of arriving at a distance x from origin after N steps of unit size is given by,

$$p(x, N) = \frac{1}{2^N} \frac{N!}{n_+!\, n_-!}. \tag{1.31}$$

Now, assuming $x << N$ and using Sterling's approximation $N! = \sqrt{2\pi N}(N/e)^N$ we can write,

$$p(x, N) = \frac{1}{\sqrt{2\pi N}} \exp \frac{-x^2}{2N}. \tag{1.32}$$

Since $\langle x^2 \rangle = N$, therefore,

$$p(x, N) = \frac{1}{\sqrt{2\pi \langle x^2 \rangle}} \exp \frac{-x^2}{2\langle x^2 \rangle}. \tag{1.33}$$

In three dimesnions, the probability $p(\vec{R}, N)$ can be given by the procudt of the probabilities in the x,y and z axes. Using equation 1.29 and 1.33, the probability in three dimensions can be written as,

$$P(\vec{R}, N) = \Big(\frac{3}{2\pi N b^2}\Big)^{3/2} exp\Big(-\frac{3\vec{R}^2}{2Nb^2}\Big), \tag{1.34}$$

which is a Gaussian probability distribution of the end-to-end vector.

Due to their thread-like structures, polymers possess properties entirely different from their small monomeric analogues. Unlike rigid molecules, the shape of polymers and its flexibility facilitates a large number of possible arrangements of structures which are known as polymer conformations. This is a significant character leading to behavior nonexistent in colloids. For a long polymer, the existence of a huge number of conformations creates a restoring force having entropic origins, leading to elastic behavior. Thus a polymeric chain acts as an entropic spring, as shown in Figure 1.12. The chain entropy can be written as,

$$S(\vec{R}) = k_B \ln W = constant + k_B \ln P(\vec{R}). \tag{1.35}$$

Using equation 1.34, We can write the above equation as,

$$S(\vec{R}) = constant - \frac{3k_B}{2Nb^2}\vec{R}^2. \tag{1.36}$$

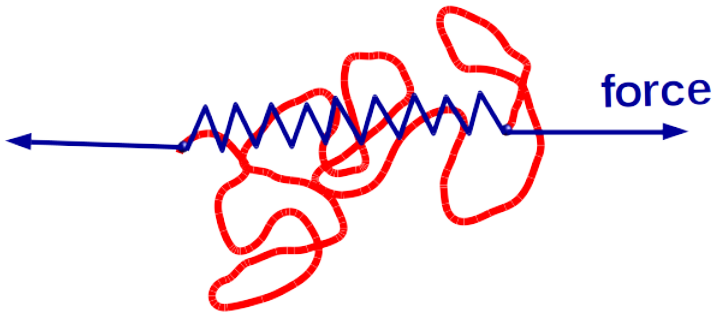

FIGURE 1.12: polymer as an entropic spring.

Therefore, the free energy can be written as,

$$A(\vec{R}) = -TS = constant + \frac{3k_BT}{2Nb^2}\vec{R}^2. \tag{1.37}$$

This is the origin of elasticity in rubbers, elastomers and other polymeric materials.

1.2.2 Effect of excluded volume: Real chains

S.F.Edwards in 1965, using the self-consistent field method, showed that the effect of excluded volume in polymers results in the swelling of the polymers. Flory, on the other hand, using the mean-field approach argued that the equilibrium chain length is controlled by a balance between excluded volume which tends to expand the chain and a restoring force due to loss of conformational entropy as a result of swelling (Yamakawa, 1971). Consider a polymeric chain of N monomers linked by segments of length b and an end to end distance R. If v is the excluded volume of a monomer pair and T be the temperature then, The energetic contribution to the free energy due to the excluded volume repulsion is,

$$F_{excl} \equiv k_BTvN^2/R^3, \tag{1.38}$$

and the entropic contribution to the free energy due to the expansion of the chain is,

$$F_{entropic} \equiv k_BT\frac{R^2}{Nb^2}. \tag{1.39}$$

Therefore, the total free energy F can be expressed as,

$$F(R) = F_{excl} + F_{entropic}(R), \tag{1.40}$$

$$F \equiv k_BT\Big(v\frac{N^2}{R^3} + \frac{R^2}{Nb^2}\Big). \tag{1.41}$$

By setting $\partial F/\partial R = 0$, the equilibrium length is given by,

$$R_F \equiv v^{1/5}b^{2/5}N^{3/5}. \tag{1.42}$$

Thus, $R_F \propto N^{3/5}$.

The simple arguments of the Flory theory give surprisingly accurate results, but this is due to the fact of a fortunate cancellation of errors. The Flory theory only includes the interaction between the monomers but, does not take into account the

connectivity of the monomers. Hence, the theory fails to include information about the spatial correlation between the monomers along the backbone of the polymer. Therefore, the arrangement of monomers on a lattice is overestimated, giving rise to an overestimated value of energy. However, at the same time, the entropy of the polymers also gets overestimated. The two errors almost cancel with each other, and the Flory theory ends up giving a nearly accurate result. The Flory theory gives a scaling which is very close to the behavior predicted by the Renormalization Group (RG) theory or simulations, which is, $R_F \propto N^{0.588} b$.

1.2.3 Polymers in a solution: Effect of interactions

For dilute solutions, mean-field Flory-Huggins lattice theory successfully explains the behavior of polymers (Yamakawa, 1971). According to this theory, volume V is divided into a lattice of N_0 cells, each cell of volume v. The molecules randomly occupy the sites with a probability depending on their respective volume fractions. Let x_1 and x_2 be the number of cells occupied by each monomer and solvent particle respectively while the corresponding volume fractions are represented by ϕ_1 and ϕ_2.

The behavior of a polymeric chain in a solution depends on the effective interactions between monomers and solution. There are three possible types of interactions represented as follows,
ϵ_{11} = polymer-polymer ϵ_{12} = polymer-solvent ϵ_{22} = solvent-solvent

Flory used a long derivation but arrived at a simple and intuitive result. The change in the entropy and enthalpy calculated to be,

$$\frac{\Delta S_M}{N_0} = -k_B \left| \frac{\phi_1}{x_1} \ln \phi_1 + \frac{\phi_2}{x_2} \ln \phi_2 \right|, \tag{1.43}$$

$$\Delta H_M = N_0 k_B T \chi \phi_1 \phi_2, \tag{1.44}$$

where, χ is known as Flory parameter, given by the following expression,

$$\chi = \frac{z}{k_B T} \Big[\epsilon_{12} - \frac{1}{2}(\epsilon_{11} + \epsilon_{22}) \Big], \tag{1.45}$$

where, z is the coordination number. Hence, the expression for free energy is given by,

$$\frac{\Delta F}{N_0} = k_B T \Big[\chi \phi_1 \phi_2 + \frac{\phi_1}{x_1} \ln \phi_1 + \frac{\phi_2}{x_2} \ln \phi_2 \Big]. \tag{1.46}$$

Figure 1.13 shows the importance of χ parameter in deciding the phase behavior. It defines the effective interaction depending on which following three situations arise,

(1)$\chi < 0$:

There is an effective attraction between polymers and solvent and the chains are swollen. Such a solvent is known to be a **Good Solvent** and the polymer end-end distance behaves as,

$$R \propto N^{3/5}. \tag{1.47}$$

(2)$\chi = 0$:

The excluded volume disappears, implying that the dilute solution acts as an ideal solution. Such a solvent is known as **theta solvent** and the polymer end-end distance follows a random walk path given by,

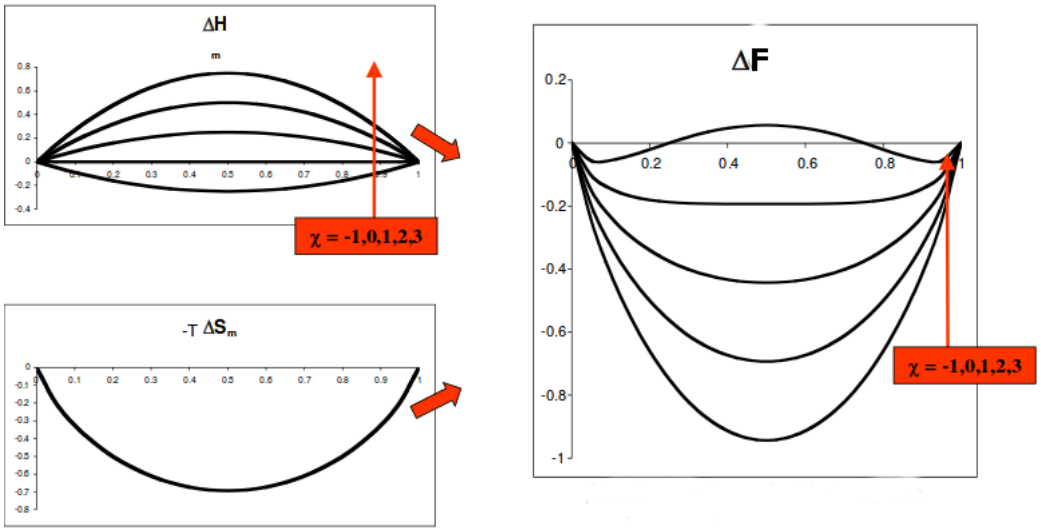

FIGURE 1.13: Variation of change in (Top left) enthalpy, (Bottom left) entropy and (Right) free energy with polymer concentration and χ parameter. Reprinted from (*OCW, MIT.*) under the Creative Common license.

$$R \propto N^{1/2}. \tag{1.48}$$

(3)$\chi > 0$:

For this case, The interactions produce an effective attraction between polymers. Therefore the polymer collapses forming a globule. Such a solvent is known as **Poor solvent** and the polymer end-end distance is the radius of the sphere in which the polymer chain collapses, therefore, can be given by,

$$R \propto N^{1/3}. \tag{1.49}$$

Figure 1.14 shows an example of the polymer behavior in a good, bad and theta solvent. The snapshots are the result of a Monte Carlo simulation of the bond fluctuation model on a simple cubic lattice.

Using the expression for free energy in equation1.46, we can calculate

Binodal curve: The locus of all the points satisfying $\frac{\partial \Delta F}{\partial \phi_1} = \frac{\partial \Delta F}{\partial \phi}$. This is also known as the coexistence curve.

Spinodal curve: The locus of all the points satisfying $\frac{\partial^2 \Delta F}{\partial^2 \phi_2} = 0$

Critical point: The point at which the binodal and spinodal curves coincide. At this point both the second and the third derivative of the free energy vanishes.

These curves are shown in Figure 1.15 in a χN versus ϕ_2 plot. The binodal curve shows the points where the two phases are in equilibrium. The region below the curve is a single-phase region while above the curve is a two-phase region. The region between binodal and spinodal curves represents the points where the two phases are stable. Above the spinodal curve, the two-phase region is unstable. The

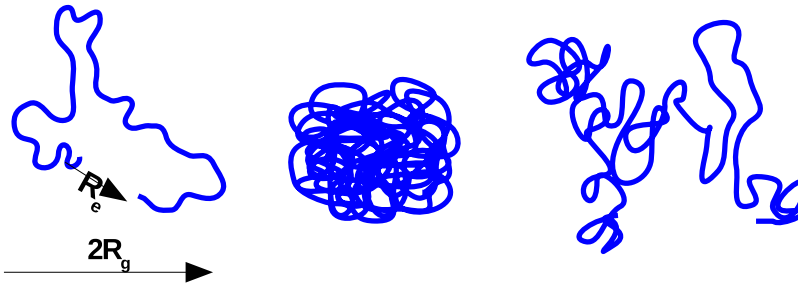

FIGURE 1.14: Polymer behavior in (Left) good (Centre) bad and (Right) theta solvent. (Binder et al., 2008)

figure also shows the critical point where the binodal and spinodal curves coincide.

Although Flory-Huggins theory successfully explains the polymer phase behavior in the dilute limit, in semidilute limits and at high concentrations, this theory fails to depict the phase behavior correctly. The following sections explains the polymers at higher concentrations.

1.2.4 Semidilute solution of polymers

The above mean-field treatment of polymers fails to explain various experimental results at high concentrations. The Flory-Huggins theory ignores the thermal fluctuations and does not distinguish the interactions of bonded monomers from non-bonded monomers, which is ascribed to its failure. Blob model and Scaling theory introduced in the 1970s, on the other hand, was able to explain well the semi-dilute regime of polymers and solve the then-mysterious problems elegantly. The semi-dilute solution is a peculiar property of polymeric systems entirely non-existent to their colloidal counterparts. The concentration at which the polymers start overlapping each other is still quite low, and there exists a wide range of concentration beyond the overlapping concentration where polymers overlap, entangle and finally form a melt at a very high concentration. Figures 1.16 shows the different regimes of polymers with varying concentration.

According to De Gennes blob model, a polymer chain can be divided into spherical blobs within which a partial chain conformation is similar to the isolated parent chain (Edwards, 1966). Thus the density of monomers in the blob mirrors the density of the whole solution. If we consider a polymeric solution divided into blobs of g monomers of size b_g with total no. of blobs N_g. If N and b are the total no. of monomers and monomer-monomer bond length respectively then we can write,

$$b_g \equiv g^{1/2} b, \tag{1.50}$$

And,

$$N_g \equiv N/g. \tag{1.51}$$

Therefore, the expression for the end-end distance of a chain made up of blobs R_b is given by,

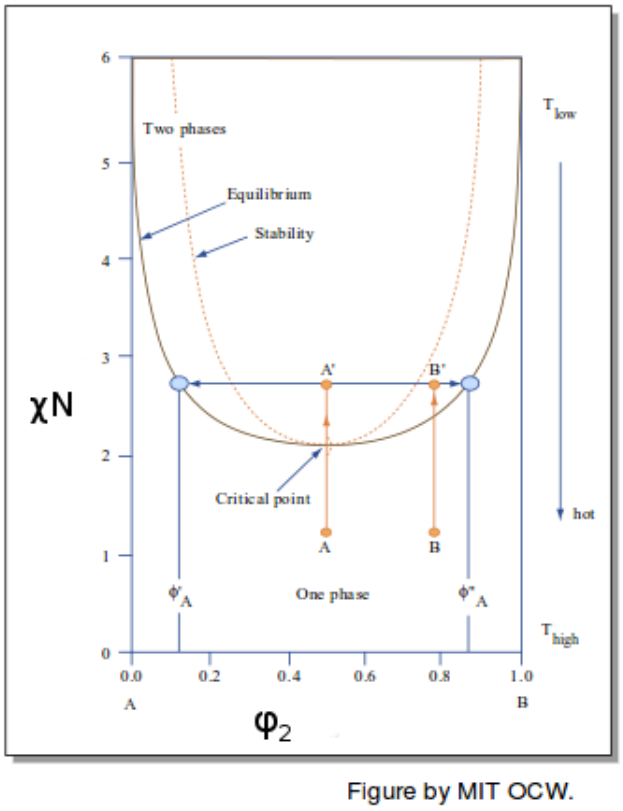

FIGURE 1.15: Polymer phase diagram using Flory-Huggins theory. Reprinted with permission from (*OCW, MIT.*) under the Creative Common license.

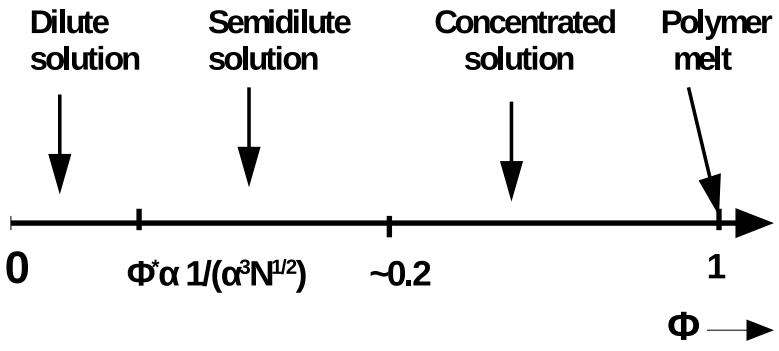

FIGURE 1.16: Dilute, semi-dilute and concentrated regimes of polymers for theta condition. Φ^* shows the crossover volume fraction between dilute and semidilute regimes and it varies as $N^{-1/2}$.

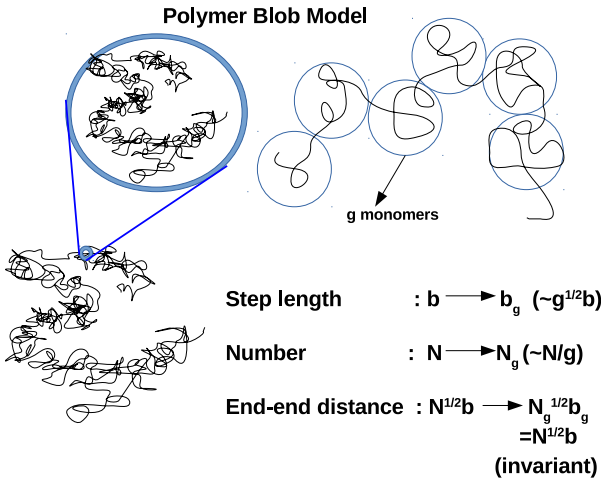

FIGURE 1.17: Polymer blob model and the invariance of the polymer end-end distance to the scaling.

$$\langle R_b \rangle = N_g^{1/2} b_g, \tag{1.52}$$

$$\langle R_b \rangle = N^{1/2} b = \langle R \rangle. \tag{1.53}$$

The above equation says that the end to end distance remains invariant to the scaling of the polymer unit. This is explained in Figure 1.17.

Figure.7 in (Wang et al., 2010) shows a schematic representation of different polymer regimes with blobs in semi-dilute regime and change of scaling with change in concentration, while Figure 1.18 summarizes the phase behavior of polymers with concentration and temperature (χ parameter).

1.3 Colloid-polymer mixture

It has been known for a long time that the addition of polymers promotes aggregation and phase separation in colloidal suspensions (Gast, Russel, and Hall, 1986; Patel and Russel, 1989; Ilett et al., 1995). Several experiments reported this peculiar behavior. An enhanced aggregation of red blood cells was reported by Fahreus in 1920 due to increased concentration of blood serum fibrinogen globulin and albumin (Fåhraeus, 1929). Traube reported a phase separation of rubber latex particle suspension into a dilute and concentric phase on the addition of plant and scaweed polysaccharides (Traube, 1925). The induced aggregation due to polymers was first explained by Asakura and Oosawa by introducing the concept of Depletion Interaction.

1.3.1 Asakura-Oosawa model: Depletion interaction

Asakura and Oosawa, formulated a theoretical description of a colloid-polymer mixture, in order to explain an experimental result of the aggregation of colloids on the addition of polymers, by introducing the idea of depletion attraction (Asakura and Oosawa, 1954). According to this idea, in a colloid-polymer mixture, a polymer of the radius of gyration R_g can reach the surface of a colloidal particle only up to a

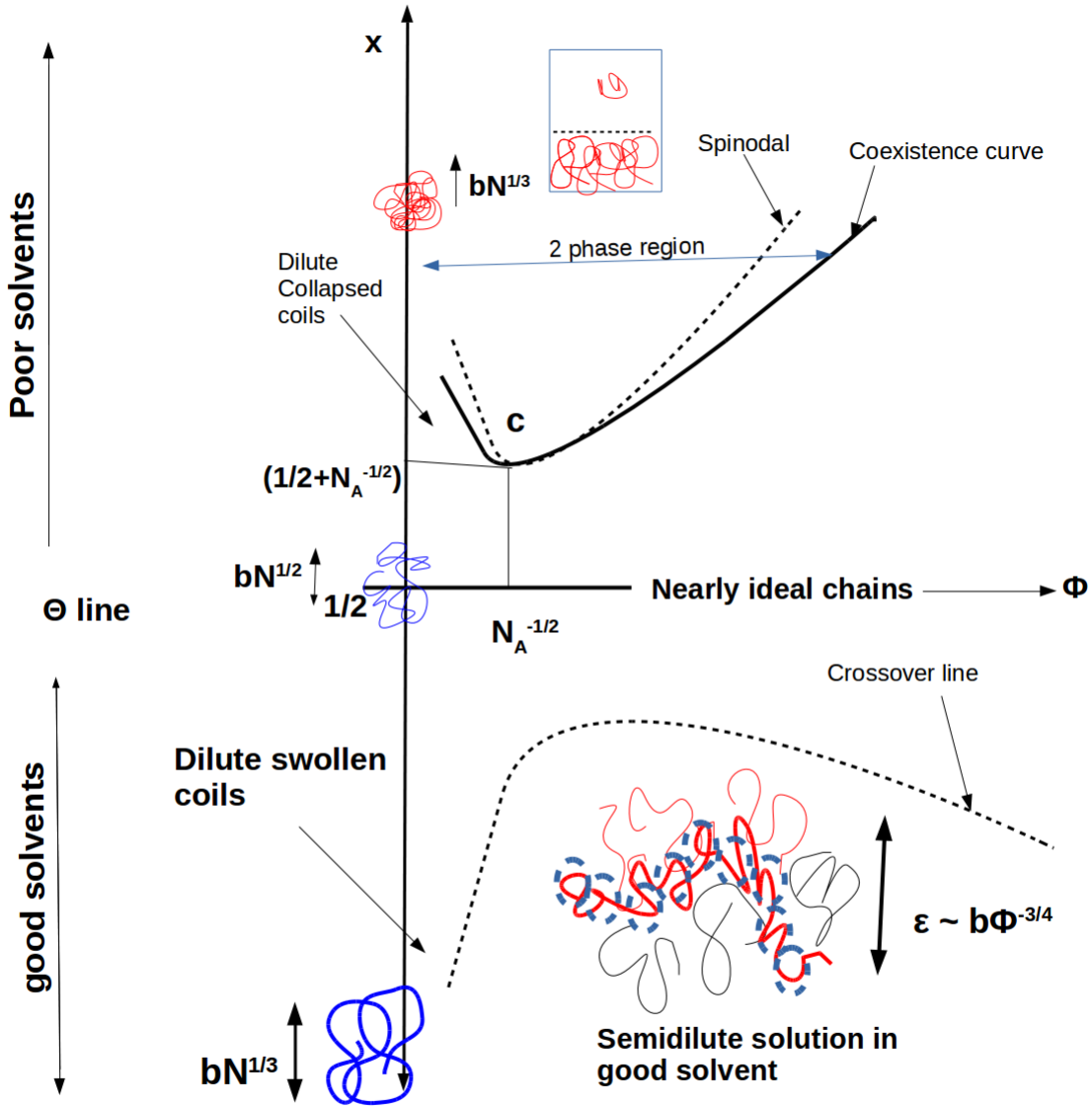

FIGURE 1.18: Polymer phase diagram in a χ parameter versus Φ (concentration) graph. The $\chi = 1/2$ line represents the Θ line. Above the Θ line the polymers are in a good solvent while they are in a bad solvent below it.

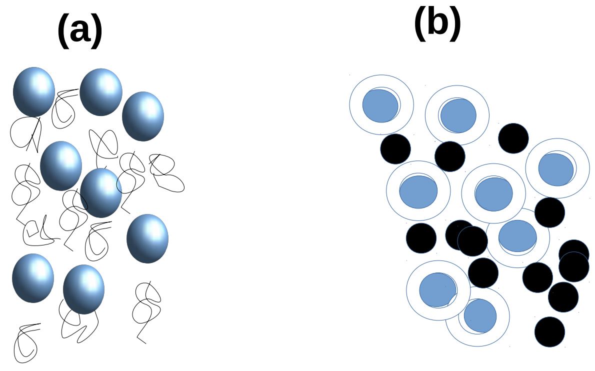

FIGURE 1.19: (a) The figure shows colloids(blue particles) and polymers(black) mixture. Since the polymers can overlap with each other but not with the colloids, the polymers are replaced as soft particles(black) in figure (b) while this leaves the colloidal particles with a depletion region around the colloidal surface (shown as a circle in broken line) where the centres of the polymers can not enter. When the depletion zones overlap, there is an increase in free volume for the polymers and also an increase in their translational entropy. Therefore, the addition of polymers in a colloidal system gives rise to an effectively attractive potential between colloids.

distance of R_g. The volume of a sphere with $(\sigma_c + \sigma_p)/2$ from the region around the colloids remains excluded, where σ_c is the diameter of colloid and the diameter of polymers is given by $\sigma_p = 2R_g$, R_g being the radius of gyration of the polymer coils. This excluded volume is known as depletion zone. When two such colloidal particles come close to each other, the depletion zones overlap and effectively reduce the total volume of it. Therefore overlapping of depletion zones increases the free volume entropy for the polymers and hence a depletion attraction is added between colloidal particles when polymers are added to the colloidal solution. This is explained in Figure 1.19 (adapted from (Binder, Virnau, and Statt, 2014)).

We present here a short overview of the model and the theories based on it not going into great details. One can refer to (Dijkstra, Brader, and Evans, 1999), (Gast, Hall, and Russel, 1983b) and (Gast, Hall, and Russel, 1983a) for details. The model can be represented by using the following pair potentials (Dijkstra, Brader, and Evans, 1999):

$$\begin{aligned} \phi_{cc}(\mathbf{R}_{ij}) &= \infty \quad \text{for} \quad |\mathbf{R}_{ij}| < \sigma_c \\ &= 0 \quad\quad \text{otherwise} \\ \phi_{cp}(\mathbf{R}_i - \mathbf{r}_j) &= \infty \quad \text{for} \quad |\mathbf{R}_i - \mathbf{r}_j| < (\sigma_c + \sigma_p)/2 \\ &= 0 \quad\quad \text{otherwise} \\ \phi_{pp}(\mathbf{r}_{ij}) &= 0 \end{aligned}$$

where, the suffixes c and p indicates colloids and polymers, respectively. $\mathbf{R}_i$ and $\mathbf{r}_j$ are the position vectors of the centres of the colloids and polymers respectively: $\mathbf{R}_{ij} = \mathbf{R}_i - \mathbf{r}_j$ and $\mathbf{r}_{ij} = \mathbf{r}_i - \mathbf{r}_j$. The polymer degrees of freedom can be integrated out in order to obtain an effective hamiltonian for the colloids. Consider N_c colloids and N_p polymers with a polymer to colloid size ratio q in the (N_c, V, z_p, T) ensemble,

where z_p is the fugacity of the system that depends on the chemical potential μ_p as follows:

$$z_p = \Lambda_p^{-3} \exp -\beta\mu_p, \tag{1.54}$$

where, Λ_p is the thermal wavelength of the polymer coils and $\beta = 1/(k_B T)$ The total Hamiltonian of the system consists of the kinetic energy contributions and the sum of the following interaction terms:

$$H = H_{cc} + H_{cp} + H_{pp}, \tag{1.55}$$

where,

$$H_{cc} = \sum_{i<j}^{N_c} \phi_{cc}(\mathbf{R}_{ij}),$$

$$H_{cp} = \sum_{i=1}^{N_c} \sum_{j=1}^{N_p} \phi_{cp}(\mathbf{R}_i - \mathbf{r}_j),$$

Since, the polymer coils are assumed to be non-interactive, $H_{pp} = 0$. Therefore,

$$H = H_{cc} + H_{cp}. \tag{1.56}$$

In order to integrate out the polymer degrees of freedom, the hamiltonian of the system can be represented by an effective hamiltonian consisting of colloid-colloid interaction and a perturbative term:

$$H^{eff} = H_{cc} + \Omega. \tag{1.57}$$

The perturbative potential Ω can be written as the sum of zero, one, two and higher body terms:

$$\Omega = \sum_{n=0}^{N_c} \Omega_n. \tag{1.58}$$

The zero body term and one body terms can be written as:

$$\Omega_0 = z_p V/\beta, \tag{1.59}$$

$$\Omega_1 = z_p \eta_c (1+q)^3 V, \tag{1.60}$$

where, η_c is the colloid packing fraction.

The two body term depends on the simultaneous coordinates of two colloids which represets the Asakura-Oosawa potential ϕ_{AO}. The exact form of this potential ϕ_{AO} is derived by Asakura and Oosawa as follows:

$$\phi_{AO}(\mathbf{R}_{ij}) = -\frac{\pi\sigma_p^3 z_p (1+q)^3}{6q^3}\left[1 - \frac{3\mathbf{R}_{ij}}{2(1+q)\sigma_c} + \frac{\mathbf{R}_{ij}^3}{2(1+q)^3\sigma_c^3}\right] \quad \text{for } \sigma_c < \mathbf{R}_{ij} < \sigma_c + \sigma_p, \tag{1.61}$$

$$= 0 \qquad \text{for} \quad \mathbf{R}_{ij} > \sigma_c + \sigma_p. \tag{1.62}$$

This is the depletion potential responsible for the attractive interaction between colloids when polymers are added to the system.

The mixture of colloids with polymers was the first studied mixture involving

colloids, much before the evolution of the idea of entropic ordering by Asakura and Oosawa (AO) and later independently and more explicitly by Vrij (Vrij, 1976). Since then, the depletion interaction has been studied extensively in the last 50 years leading to many theoretical developments, simulations and experimental studies. Even with the simplest model incorporating non-interacting ideal polymers with a fixed R_g and limitations of low concentration and low polymer to size ratios, the model has managed to depict the colloid-polymer phase behavior observed in experiments. Models developed by Lekkerkerker (Lekkerkerker et al., 1992b) and Gast et al. (Gast, Hall, and Russel, 1983b; Gast, Hall, and Russel, 1983a) are the most prominent examples which will be discussed in the following paragraphs.

1.3.2 Perturbation theory

The first study of the colloid-polymer mixture using the standard liquid state perturbation theory was carried out by Gast et al. Gast et al. (Poon et al., 1993) used the perturbation techniques in which the interactive potential is decomposed into a reference potential depicting observed behavior and a perturbation for aqueous(Gast, Hall, and Russel, 1983b) and non-aqueous solutions (Gast, Hall, and Russel, 1983a). For non-aqueous case, the hard-sphere potential is considered as a reference potential and AO depletion potential ϕ_{AO} as a perturbation:

$$\phi^{eff} = \phi_{cc} + \phi_{AO}. \tag{1.63}$$

The potential ϕ_{AO} is a two-body term (as shown in the previous section), and this method ignores the higher body term. The higher body terms are shown to be zero for low values of q (q < 0.1547) (Dijkstra, Brader, and Evans, 1999) but ignoring them for higher values of q will be a drastic approximation. The perturbation theory by Gast et al. still manages to depict a variety of aspects of the phase behaviour that has been confirmed by experiments. Please refer the phase diagrams shown in (Gast, Hall, and Russel, 1983c) and are reproduced in (Dijkstra, Brader, and Evans, 1999). It shows the dependence of phase behaviour on the size ratio q. It produces good results for solid-liquid transition but failed to give a good prediction for fluid-fluid transition for small size ratio (Dijkstra, Brader, and Evans, 1999). Moreover, a stable fluid-fluid region was also found along with a triple point for a sufficiently large value of q. It also showed the broadening of the solid-liquid region on increasing the polymer concentration when q is small (q < 0.3). Later, a solid-solid transition was also identified using the same theory by Dijkstra et al. Gast et al. later, experimentally verified the predicted types of phase coexistence regions in a model colloid-polymer system (Gast, Russel, and Hall, 1986).

1.3.3 Free volume theory

Unlike Gast et al., Lekkerkerker (Lekkerkerker et al., 1992b) used free volume theory, using free energy minimization method where the free volume accessible to the freely-overlapping polymer coils was approximated by using scaled-particle theory. This method allowed for the partitioning of the polymers between phases and corrects for multiple overlap of depletion layers which was lacking in the method used by Gast et al. Phase diagrams for the various polymer to colloid size ratios were determined. Similar to the findings of Gast et al., the phase diagrams were found to be dependent upon the size ratios. Figure 1.20 shows the phase diagram produced by Lekkerkerker for two different size ratios of 0.1 and 0.4. Both the results match

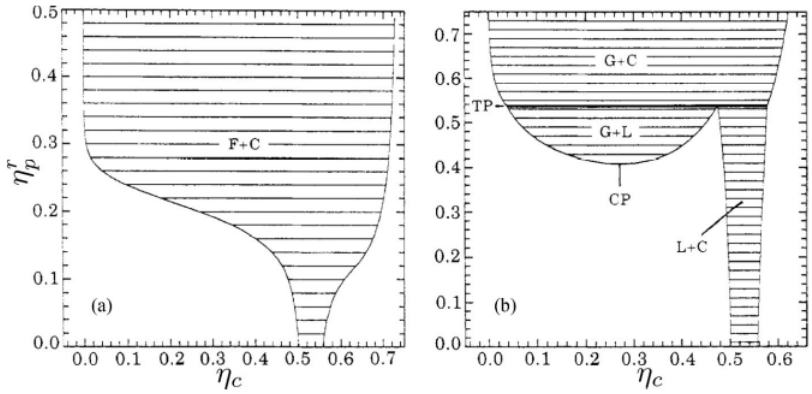

FIGURE 1.20: Phase diagrams of colloid-polymer mixtures in the plane of variables colloid-packing fraction (η_c) and polymer-reservoir packing fraction ($\eta_p{}^r$), for polymer to colloid size ratios q = 0.1 (a) and q = 0.4 (b). The curves show the boundaries of the two-phase coexistence region between fluid (F) and crystal (C) phases (for q = 0.1 (a)) where no gas (G)-liquid (L) phase separation and hence no triple point line (TP) occurs, unlike the case of q = 0.4 (b), where gas-liquid coexistence (G + L) also occurs, ending in a critical point (CP). The tie lines (connecting coexisting phases) simply are horizontal straight lines. The region to the left of the shaded area represents fluid, while the region to the right represents crystal. The phase diagrams were obtained from the free volume theory, also using the equation of state for the fcc crystal due to Hall as an input. Reprinted with permission from Lekkerkerker et al., Europhys. Lett. 20, 559 (1992).

quite well with each other. It shows fluid-solid coexisting phases for q < 0.3 and a gas-liquid coexistence for q > 0.3, similar to the theory of Gast et al.

Like colloidal systems, the colloid-polymer system also shows a fluid-solid coexistence with the coexisting region expanding with the added polymers. However, there exists a limiting value of size ratio known as crossover value beyond which the phase behavior differs from the colloidal phase behavior. After the crossover value of q, the phase diagram shows the existence of a critical point and a triple point. Both the theory of Gast et al. and Lekkerkerker produced this crossover phase behavior. These results match well with experiments and computer simulations. Also, the prediction of uneven polymer partitioning by Lekkerkerker was confirmed by experimental studies by Russel and Patel (Patel and Russel, 1989) and Poon et al. (Poon et al., 1993)

The above theories were limited to AO limit of low concentration and q value. To break the, limit Meijer and Frenkel used lattice simulation method to correct the AO model for high q value (Meijer and Frenkel, 1994). Schweizer et al. developed an integral equation approach while a novel coarse-graining technique was used, which was developed by Bolhuis, Louis and coworkers (Bolhuis, Louis, and Hansen, 2002; Bolhuis, Meijer, and Louis, 2003). These theories show the importance of enthalpic interactions in phase behavior. However, with increasing density and including non-ideality of polymer chains, the theoretical equations become very complex and need a lot of approximations and assumptions to solve them. The theoretical results to a

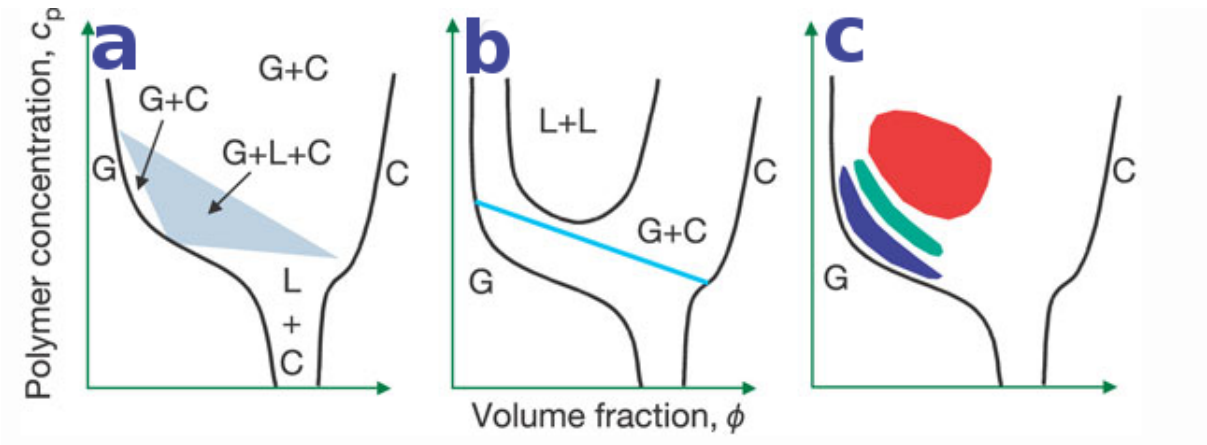

FIGURE 1.21: Statistical mechanics predict the partitioning into colloid-rich and polymer-rich phases. For a given colloid size, the phase diagrams are sensitive to the polymer size: (a) large polymer, (b) small polymer. The polymer can partition into different phases, so the lines indicating coexisting phases are not necessarily horizontal. Phase diagrams are similar to those in Fig. 1.9b, but are inverted, as polymer concentration plays the role of inverse temperature. Figure (a) is similar to an atomic system, having regions of three-phase equilibria (shaded area). Figure (b) is similar to systems found for some proteins, with two-phase coexistence and a metastable liquid-liquid region. (c) The situation often found experimentally, for short polymers. The blue area indicates a region where crystals are formed; the green area indicates aggregation, and the red area indicates gelation. Thus, only in the narrow region close to the phase boundary are the equilibrium phases reached. Reprinted with the permission from (Anderson and Lekkerkerker, 2002) (Nature. 2002 Apr25;416(6883):811-5).

major extent are dependent on the assumptions used and each theory differing in its assumptions and approximations differs to a large extent in predicting the phase behavior. Therefore it is very difficult to compare these results with experiments. (Ganesan, Ellison, and Pryamitsyn, 2010)

The literature involving mixtures of colloids and polymers, to a large extent, employs the idea of depletion for explaining phase behavior. To present a theoretical analysis of colloid-polymer mixture in great detail is beyond the scope of the thesis as the thesis is more focused on the morphological changes at the mesoscopic scale of the nanoparticle structure using wormlike micellar matrix. A brief overview of the theoretical understanding of the colloid-polymer mixture is presented because of the symmetry of the wormlike micellar and polymeric matrices. Similar kinds of nanostructures are also obtained using polymeric matrices.

However, with increasing concentration, the colloid-polymer mixtures are departed from the equilibrium and stuck in some non-equilibrium states like gels, which theoretical models are not able to capture. Recently there have been some efforts in understanding it by proposing different mechanisms for the formation of non-equilibrium states like Jamming, caging, mode coupling theories for glassy states, etc. However, the results are non-conclusive and need a more detailed study of these systems. Figure 1.21 compares the theoretical phase diagram for (a) short polymers and (b) large polymers with the (c) experimentally obtained equilibrium regions for short polymers. It shows that only in the narrow region close to the phase boundary are the equilibrium phases reached.

1.4 Wormlike micelles

Wormlike micelles are long-living polymeric structures which form the class of viscoelastic fluids. Their interesting rheological properties has garnered a lot of attention from soft matter scientists, and the relation between their rheological response and microstructure is still a subject of research. Their diverse rheological behaviors and microstructures lead to numerous applications like a thickening agent in consumer products, hydrofracking fluids in the oil industry, drug carriers in targeted delivery, turbulent friction drag-reducing agents, and templates to create functional nanofluids.

The existence of self-assembled surfactant aggregates was first suggested by Mc Bain in 1913 (McBain, 1913). It was followed by many proposals (Harkins, Davies, and Clark, 1917; Philippoff, 1950; Mattoon, Stearns, and Harkins, 1947; Hartley and Runnicles, 1938; Hartley, 1949; Corrin, 1948) but no clear theoretical or experimental evidence for different shapes of micelles until 1951 when a conclusion by Philippoff (Philippoff, 1951) indicated that the standard methods for determining micellar shapes do not differentiate between different shapes of micelles whether spherical, cylindrical, discs, branched, vesicles, cubic or lamellar, etc. Later, the development of powerful experimental techniques like small-angle X-ray and neutron scattering (Prévost, Gradzielski, and Zemb, 2017) or cryogenic transmission electron microscopy (Danino, 2012) established the different shapes of micelles and revealed their microstructures. Initially, the theoretical studies were based on the principle of minimization of free energy of the system that includes surfactant molecules, water molecules and micellar aggregates (Debye, 1948; Hobbs, 1951; Halsey Jr, 1953; Ooshika, 1954; Debye and Anacker, 1951; Hoeve and Benson, 1957; Rusanov, 2016) but these theories were lacking the most influential ingredient in the formation of micelles which is the surfactant geometry. Tanford for the first time (Tanford, 1972;

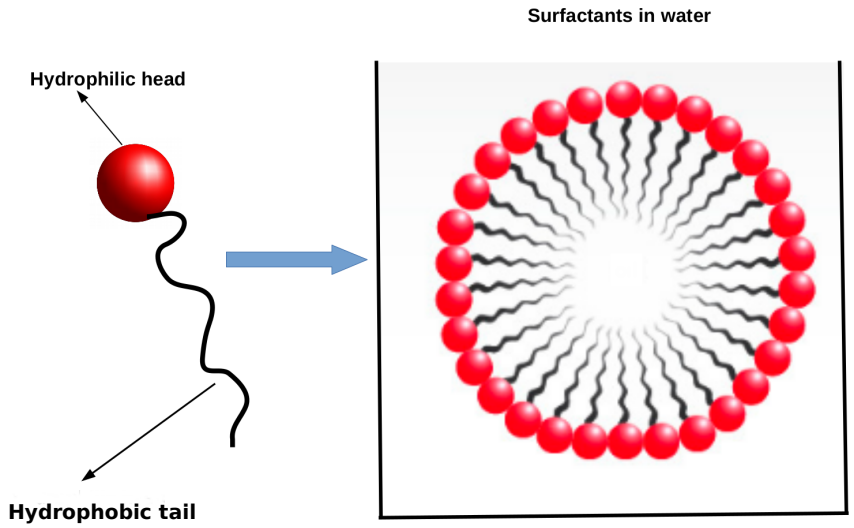

FIGURE 1.22: Formation of micelles

Tanford, 1974; Tanford, 1978) combined the concepts in earlier theories with the surfactant geometry. However, Israelachvili, Mitchel, and Ninham (Israelachvili, Mitchell, and Ninham, 1976) developed a fully geometry-based approach that was able to explain the formation of different shapes of micelles by introducing 'packing parameter'.

The aggregates of surfactants in a solution are highly polydispersed. This has been shown in the earlier theories by Debyeand Anacker (Debye and Anacker, 1951) and others and also confirmed experimentally by Scheraga and Backus (Scheraga and Backus, 1951). This is also proved later by M. E. Cates (Cates and Candau, 1990a). There are also theories by Nagarjan and Ruckenstein (Nagarajan, 1982; Nagarajan, 1993; Nagarajan and Ruckenstein, 1991) and Blankschteini et al. (Puvvada and Blankschtein, 1990; Naor, Puvvada, and Blankschtein, 1992; Zoeller, Lue, and Blankschtein, 1997; Srinivasan and Blankschtein, 2005) who used molecular thermodynamic approach that has been applied to ionic surfactants. Later, computer simulations proved to be a great way in understanding the process of formation of micelles. It is not possible to present all these theories in detail. Below, we present in brief the basic and essential elements in understanding the wormlike micellar system.

1.4.1 Surfactants

Surfactants or surface-active agents consist of two parts: a hydrophilic head group and a hydrophobic tail group. When surfactants are in a solution like water, their hydrophobic parts come together to form a core which is surrounded by hydrophilic head groups (please refer to Figure 1.22) in order to reduce the tension between surfactants and water (Holmberg et al. 2003). The hydrophilic head group can be ionic, non-ionic or zwitterionic which is attached to one end of the hydrophobic non-polar tail made up of one or two (e.g. in biological lipids) short hydrocarbon

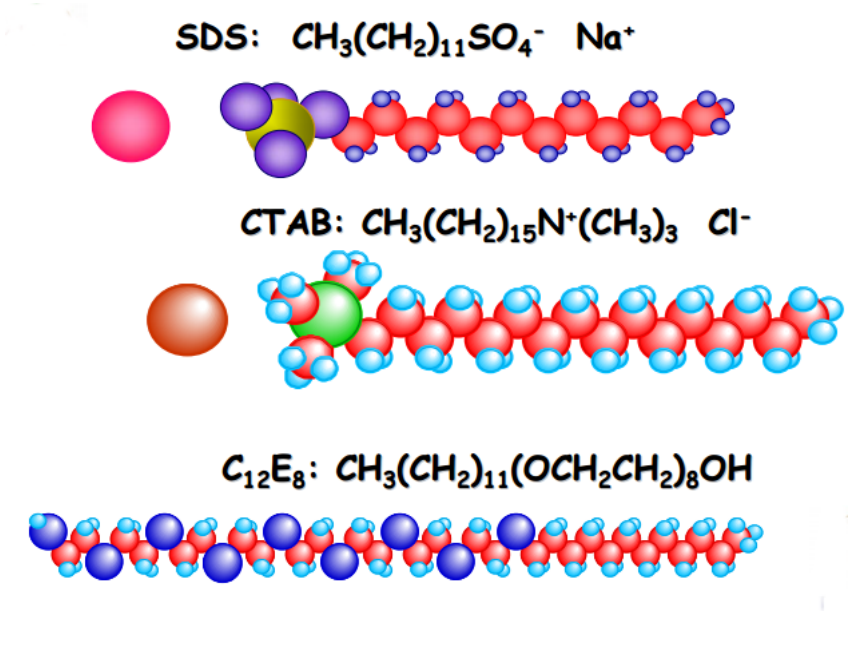

FIGURE 1.23: Example of surfactants, SDS, CTAB and $C_{12}E_8$

chains that can be linear or branched. The position of the polar group, the degree of chain branching, the length of the chain, head to tail ratio, etc., combinedly define their physicochemical properties. Some commonly used examples of surfactants are SDS :$Ch_3(CH_2)11SO_4^-Na^+$, $CTAB : CH_3(CH_2)15N^+(CH_3)Cl^-$, $C_{12}E_8 : CH_3(CH_2)11(OCH_2CH_2)8OH$ which are shown in Figure 1.23

1.4.2 Surfactants in a solution: formation of micelles

In aqueous solutions, surfactants tend to form aggregates such that the hydrophobic tails are surrounded by hydrophilic head groups in order to minimize free energy. Due to the hydrophobic effect of the tail group, the surfactant molecules migrate to the surface of the aqueous solution leading to the aggregation of surfactants whose size is limited by the repulsion among the head groups. These aggregates are generally called micelles. Once the micelle has formed, it goes into the solution from the surface. Micelles aggregate into diverse geometrically complex and dynamically fluctuating morphologies like spherical, cylindrical or wormlike micelles with or without branches, hexagonal, cubic, lamellar, etc. An important quantity known as the packing parameter gives us a method to correlate the molecular geometry with the growth of micelles (Tanford, 1980; Israelachvili et al., 1975 (Findenegg, 1986)). It is defined as :

$$P = \frac{V}{a_0 l}, \tag{1.64}$$

where, P = Packing parameter and V = Volume of the surfactant molecule.
a_0 = effective head group area and l = length of the tail group. Depending on packing parameter micelles take different shapes and arrangement of the surfactant molecules, as shown in Figure 1.24. If the packing parameter is smaller than $1/3$, spherical micelles are formed; while if it is between $1/3$ and $1/2$, cylindrical micelles may be generated; and bilayers and vesicles are formed when it is greater than $1/2$. Total surfactant concentration, the type of surfactants used, and salinity

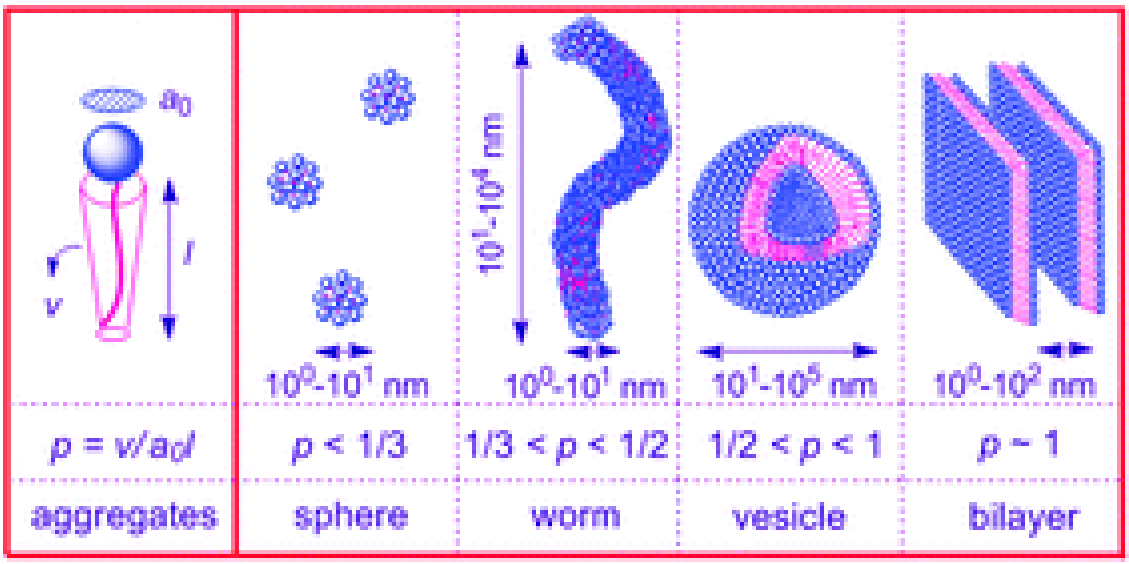

FIGURE 1.24: Different shapes of micelles formed depending on the value of Packing parameter P (Dreiss, 2017) - Reproduced by permission of the Royal Society of Chemistry [ref]

affect the packing parameter (Rehage and Hoffmann, 1988; Lequeux and Candau, 1994). The morphology of micelles can also be affected by producing changes in solution conditions such as overall surfactant concentration, surfactant composition, temperature, pressure, ionic strength, and pH.

1.4.3 Critical Micellar Concentration (CMC)

At low concentrations, surfactants remain dispersed and start overlapping as the concentration exceeds a limiting value known as Critical Micellar Concentration (CMC) and self-assemble to form aggregates which depend on various factors. Regardless of the amount of surfactant added to the solution, the unimer concentration will never exceed the critical micelle concentration (Holmberg et al., 2003). It depends on a lot of factors like tail length, polarity, alkyl chain branching, double bonds, aromatic groups, perfluorination of the alkyl group. The added electrolyte also has an effect on the CMC. The effect of salt addition depends on the valency of the ions and added counter-ions (Holmberg et al., 2003). Beyond CMC, micellar aggregates take various forms depending on the concentration of surfactants as shown in Figure 1.25. With increasing concentration spherical aggregates turns into cylindrical aggregates because of electrostatic forces, then to hexagonal, cubic, lamellar, etc. CMC increases with an increase in the volume, polarity, dipole moment, and polar surface area of the hydrophilic head group, while it decreases with the increases in the hydrophobic part of the surfactant. Empirical correlations between the structural characteristics of surfactant and CMC have been developed for ionic, cationic and anionic surfactants. According to Klevens equation, the CMC can be expressed as a function of the number of carbon atoms in the hydrophobic chain for an ionic surfactant (Klevens, 1953; Klevens, 1948)

$$log(CMC) = A - B_n, \tag{1.65}$$

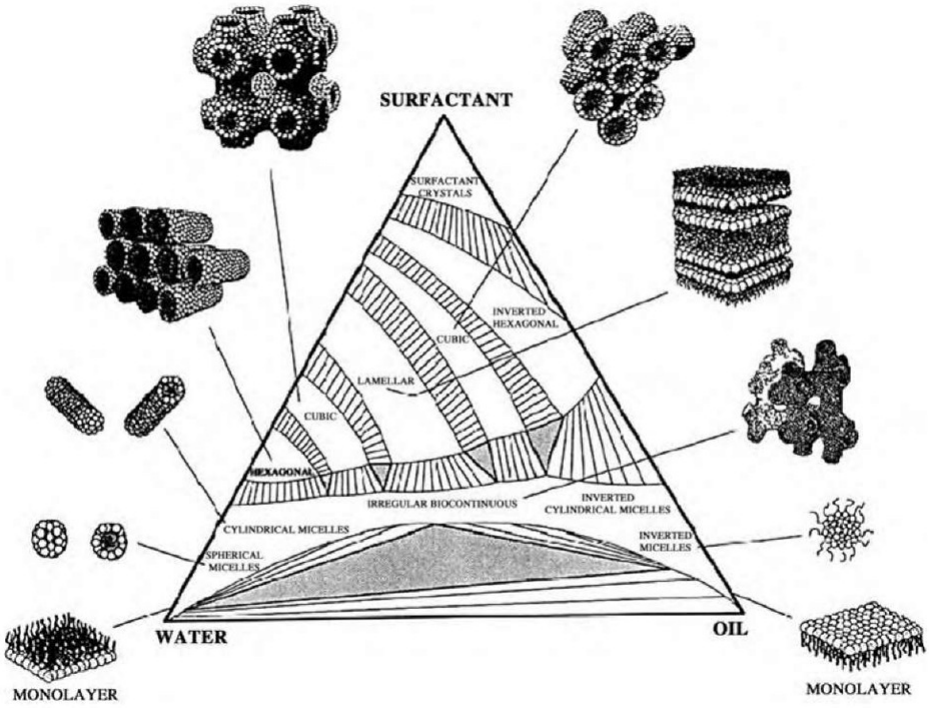

FIGURE 1.25: Different shapes of micelles formed depending on the micellar concentration and the type of solution. (*Self-Assembled Structures Part 1 (Nanotechnology):webpage*)

where, A is a parameter dependent on the ionic strength of the system and the type of the hydrophilic head group, B depends on the number of hydrophobic chains and hydrophilic head groups and n is the number of carbon atoms in the chain. Figure 1.26 is an example of this empirical relationship calculated for betaine surfactant. The values of A and B are determined as 3.046 and -0.4809, respectively. The CMC is then 350 M for n=1 for betaine surfactants. The CMC's are not affected by the hydrophilic head group as much as the hydrophobic tail. In many cases, the CMC's were found to be identical for molecules with the same tail, but differing head groups, but not zwitterionic head groups. In general, the CMC can be predicted both by the hydrophobicity of the head group and by the hydrophilicity of the tail group,

log (cmc) = a(hydrophilic descriptor) + b(hydrophobic descriptor) + c(hydrophilic descriptor x hydrophobic descriptor) + constant

Where a,b,c are constants and the expression beside c is the cross-linking term between the two effects. If it is zero, then the hydrophilicity and the hydrophobicity are independent. Quantitatively, the CMC for a variety of surfactants in different solvents has often been measured experimentally within a range of a few per cent uncertainties.

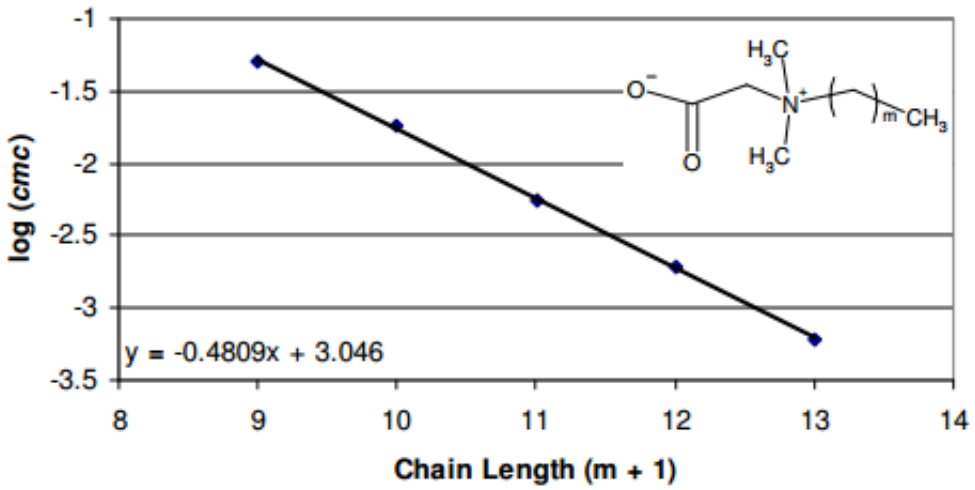

FIGURE 1.26: Graph of log(CMC) vs chain length calculated for Betaine. Adapted from the data provided in (Qu et al., 2010)

1.4.4 Wormlike micelles: Theoretical considerations

Out of various types of micelles, we are particularly interested in wormlike micelles. These micelles have got particular interest in recent years from both theoreticians and experimentalists because of their peculiar wormlike micellar phases and remarkable rheological properties. These micelles grow into long, cylindrical, semi-flexible wormlike aggregates which show many similarities with polymers: in particular, they entangle with each other above a critical micellar concentration to form a transient network, imparting interesting viscoelastic properties and nonlinear rheological characteristics. However, the property which distinguishes them from polymers is that they are constantly breaking and reforming in dynamical equilibrium. For this reason, they are also referred to as 'equilibrium polymers'. They encompass all the micelles which arise due to packing parameter values between $1/3$ and $1/2$. At high surfactant concentrations, large micelles are expected, the spherical shape of micelles will be accompanied by a large hole at the centre costing energy while wormlike micellar shape suitable to give rise to a minimum free energy structure. They are often discussed in the language of polymer physics with a consideration that their molecular weight distribution is in thermal equilibrium. Their size distribution has been calculated by Cates and Candau (Cates and Candau, 1990a).

The ends of the micelles contribute to the energy depending on its size and curvature and can increase to very high values when the spontaneous curvature is low. The fusion of micelles is accompanied by an energy gain by the loss of two end caps which is equivalent to the energy cost of creation of two end caps when they go through scission reaction. For sufficiently large endcap energies, the micelles can grow to lengths of micrometres. The gain in end cap energies is balanced by the loss in translational entropies by replacing two independently moving micelles with a larger one. Considering these two competing terms in a mean-field (Flory-Huggins) approach, Cates derived the distribution of chain length in wormlike micelles as (Cates, 1996):

$$P(L) \propto exp(-L'/L), \tag{1.66}$$

where, L' is the mean length given by,

$$L' = \sqrt{\phi exp(E_{ec}/k_B T)}, \tag{1.67}$$

ϕ is the total volume fraction of micelles and E_{ec} is the end cap energy of the micelles. This result is found to agree with the systems which exhibit weak growth, but the dependence on the power of $\phi^{1/2}$ term is subject to controversy. When charge distribution on micelles is taken into account for ionic surfactants, it changes dramatically and gives rise to three different regimes of growth of aggregates with the change in concentration of surfactants/electrolyte. This power-law type growth is obtained only at higher concentrations. For charged surfactant with low salt content, electrostatic interactions may affect the self-assembly of the surfactant molecules, leading to an exponent that is considerably larger than 0.5.

Gravsholt et al. (1979) proposed that viscoelasticity of micelles has the same physical origin as polymer melts, i.e. entanglement and reptation (Berret, 2006a; Edwards et al., 1986). By taking the analogy to polymers and their entanglement, wormlike micelles are also subjected to study based on the reptation model (De Gennes and Witten, 1980). De Gennes developed a theory for classical polymers where the polymers above an overlap concentration are constrained in a hypothetical tube formed due to the confinement by the surrounding chains. As a result of a small perturbation, polymers can relax inside that hypothetical tube created by the presence of the other polymers surrounding them which is known as Reptation and has a characteristic time scale τ_{rep}. Cates further extended this model for wormlike micelles by considering the scission and recombination reactions in micelles in addition to Reptation which is known as Reptation-reaction model. In this model, the relaxation time is shown to be (Cates and Candau, 1990a),

$$\tau = \sqrt{(\tau_{break}\tau_{rep})}, \tag{1.68}$$

where, τ_{break} is the lifetime of a micelle of mean length. This is an interesting result which is quite unusual for complex fluids, which generally show deviations from Maxwellian behavior. This Maxwell-like behavior has been observed over a range of wormlike micellar fluids in dynamic modulus experiments hence justifying Cates model. While for breaking time larger than reptation time, the micelles behave as ordinary 'dead polymers' as they are dominated by reptation. The exponents predicted using Reptation-reaction kinetic model are close to the observed values for some systems, but there exists a lot of discrepancies (Cates and Candau, 1990a). Some authors have ascribed this to the existence of micellar branching while Berret suggests that it is due to the fact that for these systems, the average micellar length does not follow the predicted one. He also suggests that the theory is not applicable for systems with strongly binding counterions.

Even at equilibrium, micelles are dynamically active units with scission and recombination reactions. Aniasson and Wall put forward the initial theoretical explanation of the formation of micelles with the assumption that micelles can only grow through monomer exchange (Aniansson and Wall, 1974; Aniansson and Wall, 1975). The kinetics of relaxation after a small perturbation to the equilibrium state of wormlike micelles was theoretically studied by Turner and Cates. Using the equilibrium length distribution, they examined a system which is evolving in time with given rate constants for scission and recombination reactions which leads to an equation for the time evolution of the length distribution. This was further studied by Marques and Cates to take into account larger perturbations in the mean length of the micelles.

As micelles grow longer, due to bending rigidity, there is an energy cost for bending. The elastic energy cost dE_{ee} of bending a length element dL of a cylinder to curvature C is

$$dE_{ee} = 1/2KC^2dL, \tag{1.69}$$

where, K is the bending modulus.

This gives rise to a characteristic length scale which represents the flexibility called persistence length l_p given by

$$l_p = K/k_BT. \tag{1.70}$$

The persistence length separates the shorter length scale over which the micelle is essentially a rigid rod and the longer length scale where it is more like a flexible polymer with the conformation corresponding to a random walk. This separation of length scales, which holds for sufficiently long flexible micelles, allowed for the early measurement of the rigidity and length of micelles using neutron scattering methods [13, 14]. For micellar chains of length much larger than persistence length, Semenov and Khokhlov using Onsager's method showed a first-order phase transition in micelles where micellar structure changes from isotropic state to aligned state which is known as Isotropic-Nematic transition (Van Der Schoot and Cates, 1994; Semenov and Khokhlov, 1988; Khokhlov and Semenov, 1981). There have been some experiments determining the phase diagram of micelles. Which shows phases like hexagonal, nematic discotic and lamellar in addition to isotropic and nematic phases with a controversy over the predicted phase boundaries using theory. Figure 6 in (Berret, 2006a) shows a phase diagram for four different micellar systems obtained experimentally showing various phases of micelles like isotropic (entangled), nematic (N) and hexagonal (H), nematic discotic (N_D) and lamellar (L_α).

1.5 Colloid-Micelle mixture

At low concentrations, surfactants are extensively used as stabilizers of colloidal dispersion while high surfactant concentration induces a loss of dispersion stability. This loss of stability is ascribed to the formation of wormlike micelles above CMC and hence producing a depletion interaction. This is observed for both negative and positive colloidal particles in both negative and positive surfactants. At high concentrations, wormlike micelles form a viscoelastic fluid, and many studies suggest that inclusion of colloidal particles improves their rheological properties. An experimental study by Piazza and Di Pietro (Piazza and Di Pietro, 1994) shows that unlike the colloid-polymer phase diagram which shows fluid-crystal coexisting phases for high enough depletant concentrations, Colloids exist in the form of a gel with no structural reorganization or sedimentation for weeks in a colloid-spherical micelles system. Figure.2 in (Baxter, 1968a) shows the experimental phase behavior of colloid-spherical micelle mixture and compares it with the results from the theory of Lekkerkerker. The experimental results are scaled to agree with the theoretical phase boundary. The figure also shows the plot of percolation threshold for gel formation using the Baxter model (Baxter, 1968a) for attractive spheres which agrees quite well with the experimental results (Baxter, 1968b). Studies suggest that the addition of micelles can destabilize suspensions and cause creaming, flocculation, aggregation and fusion of the suspended species (Kline and Kaler, 1996). All these studies suggest that there exists an active interaction between micelles and colloids

that modifies the effective colloidal interaction in a colloid-micellar mixture and improve rheological properties in a viscoelastic wormlike micellar fluid, but they are still incompletely understood. The literature lacks any detailed study involving the mesoscopic structure of the wormlike micelle-colloid mixture. This thesis intends to fill this gap in the literature.

1.6 Polymer nanocomposites and the method of templating for nano-assembly

After the discovery of Nylon-6 which shaped the economy of the synthetic fibre industry, much of the interest of researchers was drawn by polymer-nanocomposites due to its enhanced performance. Though Bower mentions about nanocomposite material in his 1949 paper, not much was explored about them and until 1970s minerals were only used as fillers. However, the significance of these nanocomposites was realized only after a landmark study by Toyota in 1992 regarding the preparation of Polyamide-6/organophilic clay nanoparticles. This new material was reported to be having 40% increase in rupture tension, 68% in Young's modulus, 126% in flexural modulus and enhanced heat distortion temperature in comparison to pure polymer (Duleba, Spišák, and Greškovič, 2014). Because of its explosively enhanced properties and low cost, it was widely adapted in various industries, after its first commercial use by General Motors in 2002. After this paper by Toyota, there comes an era where researchers were trying to find an explanation for enhanced properties of nanocomposite materials and many experiments conducted reporting a number of fracture mechanisms. A variety of polymer matrices were used, such as Epoxy, polyamide, polystyrene, polyurethane, and polypropylene (Dufton, 1998). While the creation of additional surfaces on crack propagation as a primary means of toughening is reported by Zerda et al. (Zerda and Lesser, 2001), another study claimed 'crazing' to be the main toughening mechanism (Kim and Michler, 1998). Wang et al. observed the creation of microcracks and their coalescence to form macrocracks, on an application of stress (Elboujdaini et al., 2000; Ma et al., 2005). Some reports are also published showing the dependence on clay loading and extent of exfoliation (Wang et al., 2005; Lee et al., 2005; Gonzalez, Eguiazabal, and Nazabal, 2006; He et al., 2008). A recent study by Quaresimin et al. indicates the homogeneous spread of clay particles transferring stress more efficiently compared to inhomogeneously spread clay particles which lead to higher no. of defects and suppressed mechanical properties (Opelt and Coelho, 2016a; Quaresimin, Salviato, and Zappalorto, 2015). Though literature presents a no. of toughening mechanisms like cavitation, shear Yielding, crack pinning, crack deflection, crack bridging pull out, nanoparticle mobility etc., the information available is still nonextensive due to expensive experiments and non-compatibility of techniques to nanoscale constituents (Opelt and Coelho, 2016b; Carolan et al., 2017; Liang, 2008). Mostly these experiments were performed hoping to produce high-performance materials while experiment to understand their damage mechanisms are still lacking. There existed some mechanics-based model and successfully used in fibre reinforced nanocomposites like Halpin-Tsai model (Affdl and Kardos, 1976) and Mori-Tanaka model (Mori and Tanaka, 1973; Dvorak, 1991). These analytical models take into account the parameters such as elastic stiffness of matrix, aspect ratio, volume fraction and orientation of reinforcement. However, these analytical models were unable to capture the nanoscale constituents of the system hence, increasing complexity and decreasing the accuracy of the analysis (Pitsa and Danikas, 2011).

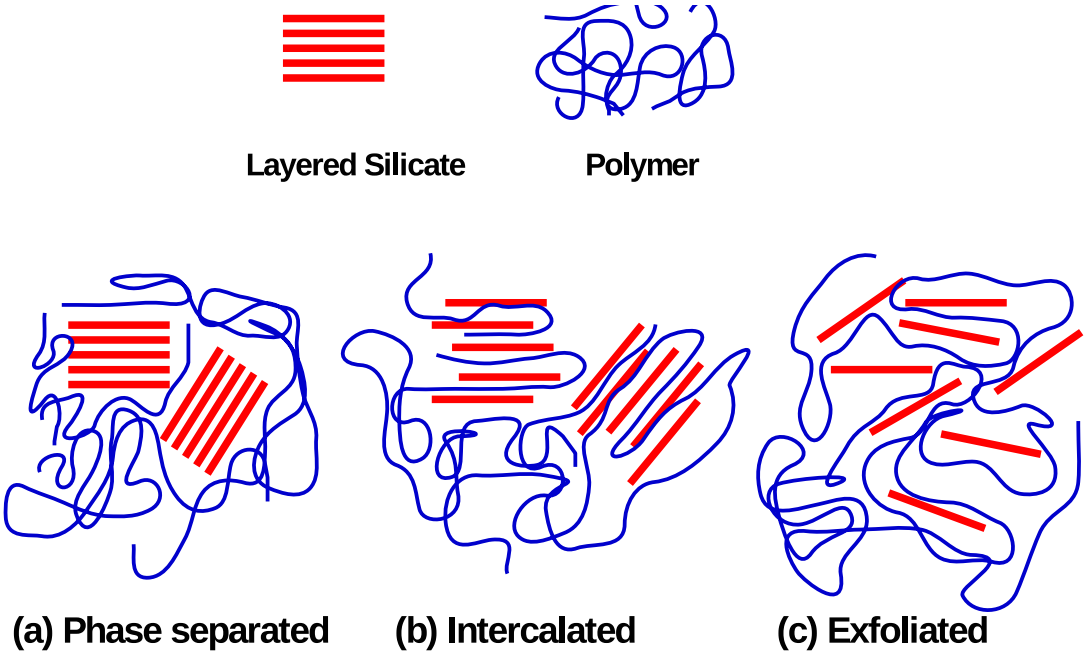

FIGURE 1.27: Different types of composites arising from the interaction of layered silicates and polymers; (a) Phase separated microcomposite (b) Intercalated nanocomposite (c) Exfoliated nanocomposite. Adapted from (Camargo, Satyanarayana, and Wypych, 2009)

The transition from a colloid-polymer mixture to polymer nanocomposite is quite dramatic and is attributed to the high surface to volume ratio of nanoparticles and quantum effects. Different kinds of fillers are used for polymer reinforcement, e.g. particles, layered and fibrous materials. Figure 1.27 shows an example of layered silicate with three different types of composites. Figure 1.27a shows a phase-separated composite which shows the reinforcement of the level of traditional microcomposites. Figure 1.27b shows a well-ordered multilayer morphology resulting in alternating polymeric and inorganic layers, while maximum reinforcement is obtained in a fully exfoliated layers of silicate as shown in Figure 1.27c. Thus the resultant properties of a polymer nanocomposite not only depends on the topology of nanofillers but also on the level of exfoliation. Finally, the interfacial interaction between polymer and fillers greatly influence the composite properties and modifying the interfacial interactions can tailor the properties of nanocomposites.

Around the 1980s, the petroleum industry was facing a challenge to produce mesoporous molecular sieves. Zeolite and its hybrids were widely used in the petroleum industry as molecular sieves for various extraction and filtration processes but were limited by its small pore size. Near the end of the 1980s, a breakthrough discovery by a group of four scientists from Mobil Oil Corporation revolutionalized the whole industry of nanofabrication giving birth to a new approach known as the Bottom-up approach. The scientists from Mobil Oil Corporation discovered a new family of mesoporous sieves, of which the material known as MCM-41 was reported to be produced by the method of templating using a micellar matrix. Owing to the simplicity, low cost and its adaptability, the method in no time became popular among researchers and widely adapted in industries opening a new era in synthetic chemistry and physics and especially nanofabrication. The then nanofabrication industry challenged with defect-free and novel nanomaterials and cost of production,

warmly welcomed this new method of nanofabrication and extensively employed various polymeric, liquid crystalline and supramolecular systems as templates of which diblock and triblock copolymers are the most prominent examples. Though advances in various lithographic techniques like X-ray, ion-beam or electron-beam provides access to sub-100nm scales, they are very costly and time consuming with the requirement of state of the art facilities. Moreover, as the Top-Down approach involves the machining of a large structure to build devices at the nanoscale, production of defect-free materials is quite challenging to it. On the other hand, in a Bottom-Up approach, the nanoscale structures are produced by assembling the basic building blocks at sub-nm or nm scale, like atoms, molecules, polymers, colloids in a controlled way. A wide variety of techniques have been developed in the last two decades like electrochemical deposition, co-precipitation in solution, chemical vapour deposition, templating etc, but the templating method stands out as a practical physical-chemical method and a reliable alternative to the top-down technique because of its low cost, simplicity and the ease of tailoring the template dimensions. Micelles, zeolite, glasses, block copolymers, layered materials, biological membranes and other supramolecular materials are some of the examples of templates. By exploiting the anisotropy in their topological structures, nanoscale pores, voids, etc., nanoparticles are deposited inside them to grow nanostructures. For a long time, these systems were exploited as templates, but some of the studies(like Balasz et al.) paid the attention of the scientific community towards the structures formed by the synergistic self-assembly due to coupled interactions of nanoparticles and the polymeric template.

Self-assembly, had a long journey from its earliest work in 1935 by Irvin Langmuir and Katherine B. Blodget, to Onsager's seminal paper highlighting the role of entropy in self-organizing structure, to its employment in a bottom-up approach in current nanofabrication industry. While Pinnavia and coworkers and Stucky group introduced the precipitation-based method, Attard et al. reported the formation of mesostructured cubic, hexagonal or lamellar structures by sol-gel polymerization in lyotropic liquid crystals, thus familiarizing with the liquid crystal templating. There are also reports of the formation of block copolymer templated mesoporous films and monoliths by evaporation induced self-assembly by Brinker et al. and also using the method of Nanocasting by Ryoo et al. The main idea behind template-directed self-assembly is to create an organized texture of the template in the nanoparticle network growing inside it, which involves an interplay of physical and chemical factors in designing structures.

There have been a lot of interests in the surfactant-based self-assembly of nanoparticles due to its interesting and complex mesoporous structures that they form in a solution. The amphiphilic property of a surfactant has also been explored in a block copolymer where the two different blocks of the polymers have the amphiphilic nature, and various nanostructures have been created using it. In surfactant-based self-assembly of inorganic nanoparticles, there are three fundamental interactions to consider whose interplay decide the final hybrid mesophase. Those three fundamental interactions are,
(1) Surfactant-Surfactant
(2) Surfactant-inorganic
(3) inorganic-inorganic

This is explained in Figure 1.28
If ΔG_{inorg}, ΔG_{org}, ΔG_{inter} and ΔG_{sol}, ΔG_{ms} denotes the free energy changes

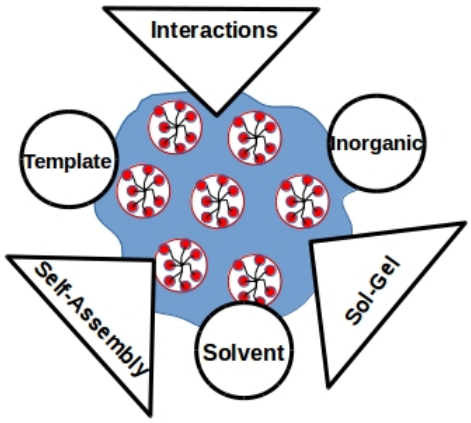

FIGURE 1.28: Scheme of the main relationship between the solvent, the template and the inorganic centre: The synergistic interaction. Adapted from (AA Soler-Illia et al., 2003)

due to inorganic-inorganic, surfactant-surfactant, surfactant-inorganic interface, solvent interactions and mesophase energies respectively, then the total change in free energy is given by,

$$\Delta G_{ms} = \Delta G_{inorg} + \Delta G_{org} + \Delta G_{inter} + \Delta G_{sol}. \tag{1.71}$$

To selectively deposit inorganic particles in a template without disrupting its texture by first letting the template grow and then selectively adding inorganic particles to form a well-defined hybrid structure requires that,

$$|\Delta G_{inorg}| < |\Delta G_{inter}| or |\Delta G_{org}|. \tag{1.72}$$

Therefore, there exists a huge literature on a controlled and selective deposition of inorganic particles by using chemical interactions or external fields. In the case of block copolymers,

$$\Delta G_{org} \propto \chi_{AB}, N_A, N_B, \tag{1.73}$$

where, χ_{AB}, N_A, N_B denote the strength of repulsion between the blocks A and B of the copolymer, no. of A blocks and no. of B blocks respectively. The kinetic features of inorganic components play a significant role, and the inorganic polymerization may lead to a metastable state where the hybrid mesophase gets 'froze'. To achieve an equilibrium ordered state, an adequate balance between the surfactant-surfactant interaction (ΔG_{org}) and the interaction at the interface (ΔG_{hybrid}). Thus, the formation of an organized mesophase is the result of an adequate balance between the phase separation of the template and the inorganic polymerization. Once the hybrid mesophase is formed, the system is suitably treated to remove the template in order to recover the nanostructure. Figure 1.29 shows an example of the steps involved in the formation of a mesoporous network of oxides. First, a hybrid mesophase is formed by mixing the organic and inorganic components. Then, it is

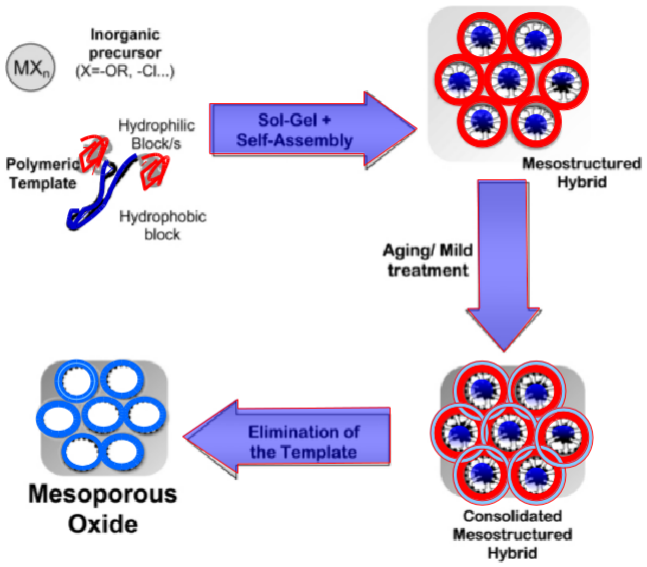

FIGURE 1.29: Schematic view of the steps leading to form a solution to a mesoporous oxide network. Adapted from (AA Soler-Illia et al., 2003)

suitably treated, and the organic templating component is removed to obtain the inorganic nanostructure finally. Using surfactants as templates make the removal of the template from the hybrid mesophase easier in order to recover the nanoparticle phase.

1.7 Scope of the thesis

Despite the interesting structural and rheological properties possessed by wormlike micelles, the literature is still lacking a systematic study of nanoparticle self-assembly using wormlike micelles. This work is a step towards understanding the system in detail and will give future directions to study its equilibrium and non-equilibrium properties. The wormlike micelles and nanoparticles mixture is a multiscale system requiring an equally multiscale approach to study their behaviour. The goal of this thesis is to develop a coarse-grained model of the wormlike micelle-nanoparticle system that gives us the flexibility to study the system behaviour with respect to the change in various system parameters. Using a suitable Monte Carlo algorithm, we study the self-organization of the system. The self-organization of nanoparticles inside the model wormlike micellar matrix is also provided with theoretical insight. The rest of the thesis is organized as follows:

In Chapter 2, we describe the computational model and method to study the self-organization of wormlike micelles and nanoparticles, justifying the use of the coarse-grained model. The results obtained by using this model and method for a dense system of wormlike micelles and nanoparticles by varying the minimum approaching distance between nanoparticle-micelle and the size of nanoparticles are presented in chapter 3. In this chapter, we report the formation of the rod-like structure of nanoparticles. The effect of variation of the density of wormlike micellar matrix is investigated in Chapter 4, where we report various morphological changes

in nanoparticle structures and conclude these results in a diagram depicting these structural changes. Chapter 5 gives the concluding remarks.

Chapter 2

Modelling and method

With the theoretical and experimental limitations, mesoscopic computational models have emerged as a bridge between the two. They have been successfully applied throughout soft matter, phase transition problems, liquid crystals etc. (Peter and Kremer, 2009). Wormlike micelles have been extensively explored as a viscoelastic fluid using the constitutive equations (Spenley, Cates, and McLeish, 1993), but the exact mechanism of their rheological behaviour like shear banding, shear thinning and shear thickening is still under debate (Germann et al., 2016). Moreover, the atomistic scale simulations cannot reach large enough length and time scales to predict the system behaviour at the mesoscopic scale. Hence, mesoscopic simulation methods are efficiently used for such systems. Coarse-grained modelling is a powerful tool for simulation and studies of equilibrium and nonequilibrium properties of self-organizing soft matter systems. The self-organization of soft matter systems at the mesoscopic level is the effect of a large number of internal degrees of freedom of constituent molecules. Therefore, these molecules can be grouped together to eliminate the unwanted degrees of freedom in action at small scales and thereby in retains the details which are relevant to the system. Thus, coarse-graining decreases the number of unnecessary processing of information, making the simulation cost and time effective. Moreover, it is impossible to access the length and time scales at the mesoscopic level using atomistic simulations.

There exist many models that represent the wormlike micellar systems at different time and length scales. Some of them are of atomistic-level which simulates the self-assembly of wormlike micellar chains from amphiphilic molecules (Maillet, Lachet, and Coveney, 1999; Yakovlev and Boek, 2007), while others using a coarse-grained model which represents the wormlike micellar chains as a chain of few beads (Goetz and Lipowsky, 1998). One of the mesoscopic model known as FENE-C model (Kröger and Makhloufi, 1996) is one of the widely explored models where the wormlike micelles are represented as a chain of hard spheres which can grow by the addition of monomers at the chains ends or by recombination with other chain ends. The bonds can break by thermal fluctuations or tension. Using FENE-C model equilibrium and shear properties of wormlike micelles have been explored (Huang, Ryckaert, and Xu, 2009). There is another self-assembling model by Chatterji and Pandit (Chatterji and Pandit, 2001a) where particles interact via an isotropic two-body interaction and a semiflexibility inducing three-body interaction enforces chain self-avoidance, hence suppressing branching. A Monte Carlo simulation is used to investigate the equilibrium properties of the system.

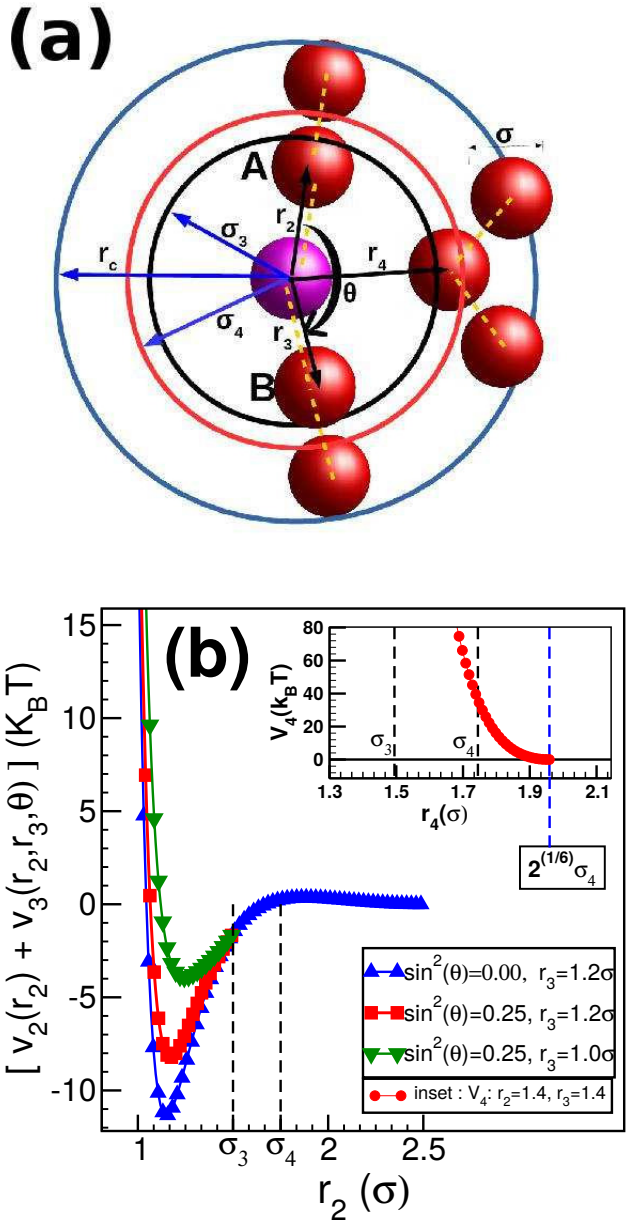

FIGURE 2.1: (colour online) (a) The figure shows the schematic representation of the range of different interactions (V_2, V_3, V_4) of the model potentials. The red spheres denote the monomers of size σ which self-assemble to form equilibrium polymers. All the distances are shown with respect to the monomer shown in pink. These monomers are acted upon by two body potential V_2 having a cutoff range of r_c. A three-body potential V_3 is acting on a triplet with a central monomer bonded by two other monomers (joined by a dashed line) at distances of r_2 and r_3, forming an angle θ at the central monomer (shown in pink) and having a cutoff range of σ_3. There is also a purely repulsive four-body potential V_4 which is a shifted Lennard-Jones potential introduced to prevent branching. The distance $2^{1/6}\sigma_4$ is defined as the cutoff distance for V_4. (b) The figure shows the plots of $V_2 + V_3$ for different values of versus r_2 for fixed values of $\sin^2(\theta)$. $\sigma_3 = 1.5\sigma$ is the cutoff distance for potential V_3. The inset shows a suitably shifted Lennard-Jones potential V_4 with a cutoff distance of $2^{1/6}\sigma_4$, where $\sigma_4 = 1.75\sigma$.

2.1 Semiflexible equilibrium polymers (or wormlike micelles)

2.1.1 Model

The model we use is a modified version of a previous model presented by Chatterji and Pandit (Chatterji and Pandit, 2001c; Chatterji and Pandit, 2003). In this model, wormlike micelles (WLMs) are represented by a chain of beads (called monomers here which are shown as spheres in Fig.2.1(a)) which interact with the given potentials to form equilibrium polymers (wormlike micelles) without branches. Every single bead or a monomer in the model is representative of an effective volume of a group of amphiphilic molecules. Thus, the WLMs are modelled at a mesoscopic scale ignoring all the chemical details. The diameter of a monomer σ is taken as the unit of length in the system. The potential is the combination of three terms V_2, V_3 and V_4:

- We have a two-body Lennard-Jones (L-J) potential modified with an exponential term,

$$V_2 = \epsilon[(\frac{\sigma}{r_2})^{12} - (\frac{\sigma}{r_2})^6 + \epsilon_1 e^{-ar_2/\sigma}]; \forall r_2 \leq r_c, \tag{2.1}$$

  where, r_2 is the distance between two interacting monomers with $\epsilon = 110k_BT$ and the cutoff distance of the potential is at $r_c = 2.5\sigma$. The exponential term in the above potential creates a maximum at $\approx 1.75\sigma$ which acts as a potential barrier for two monomers approaching each other. Two monomers are defined as bonded when the distance r_2 between them becomes $\leq \sigma_3 = 1.5\sigma$, such that the interaction energy is negative. This is explained schematically in Fig.2.1(a) and the plot of the potential is also shown in Fig.2.1(b) (full line-blue). We set $\epsilon_1 = 1.34\epsilon$ and $a = 1.72$.

- To model semiflexibility of chains, we use a three-body potential V_3,

$$V_3 = \epsilon_3(1 - \frac{r_2}{\sigma_3})^2(1 - \frac{r_3}{\sigma_3})^2 \sin^2(\theta); \forall r_2, r_3 \leq \sigma_3. \tag{2.2}$$

  Here, r_2 and r_3 are the distances of the two monomers A and B (refer Fig.2.1(a)) from the central monomer (coloured pink) which forms a triplet with an angle θ subtended by $\vec{r_2}$ and $\vec{r_3}$. Here $\epsilon_3 = 6075k_BT$. The prefactors to $\sin^2(\theta)$ are necessary to ensure that the potential and force goes smoothly to zero at the cutoff distance $\sigma_3 = 1.5\sigma$ for V_3. This three-body potential modelling semiflexibility acts only if a monomer has two bonded neighbors at distances of $\leq \sigma_3$. Fig.2.1(b) shows the plots of $V_2 + V_3$ for $r_2 = \sigma$ and different values of r_3 and θ. This potential penalizes angles $< 180^\circ$. Configurations with $\theta = 0^\circ$ are prevented by excluded volume interactions of the monomers.

- Monomers interacting by potentials V_2 and V_3 self-assemble to form linear polymeric chains with branches. A fourth monomer can get bonded to a monomer which already has two bonded neighbours to form a branch. In order to avoid branching, it is necessary to repel any monomer which can potentially form a branch. Therefore, we introduce a four-body potential term which is a shifted Lennard-Jones repulsive potential V_4 which repels any branching monomer at distances $\approx \sigma_4$, where $\sigma_4 = 1.75\sigma > \sigma_3$. The explicit form of the potential V_4 is,

$$V_4 = \epsilon_4(1 - \frac{r_2}{\sigma_3})^2(1 - \frac{r_3}{\sigma_3})^2 \times V_{LJ}(\sigma_4, r_4); \forall r_4 \leq 2^{1/6}\sigma_4. \tag{2.3}$$

Here, r_2 and r_3 are the distances of the two monomers from central monomer(coloured pink) which forms a triplet, while r_4 is the distance of the fourth monomer which tries to approach the central monomer which already has two bonds, as shown in Fig. 2.1(a). We set the cutoff distance for this potential to be $2^{1/6}\sigma_4$ with a large value of $\epsilon_4 = 2.53 \times 10^5 k_B T$. The value of ϵ_4 is kept large enough to ensure enough repulsion in case $(1 - \frac{r_2}{\sigma_3})^2 << 1$ and/or $(1 - \frac{r_3}{\sigma_3})^2 << 1$. These terms are necessary to ensure that if r_2 or r_3 becomes $\geq \sigma_3$, V_4 and the corresponding force goes smoothly to zero at the cutoff of σ_3.

All the three potentials are summarised in Fig.2.1(a). In this figure, the red spheres denote the micellar monomers having size σ. These monomers are acted upon by two body potential V_2 having a cutoff range of r_c. The potential is shown in Fig.2.1(b) indicated by the legends $\sin^2\theta = 0$ (triangle-blue line). A three-body potential V_3 is acting on a triplet with a central monomer bonded by two other monomers at distances r_2 and r_3 (bonded monomers are joined by dashed lines). The vectors $\vec{r_2}$ and $\vec{r_3}$ subtends an angle θ at the central monomer and the potential V_3 has a cutoff distance of σ_3 (Fig.2.1(b)). The three-body potential V_3 modifies the two body potential V_2 such that the resultant potential energy $V_2 + V_3$ gets shifted to a higher value of energy depending on the value of θ, r_2 and r_3. This is illustrated in the graph for $\sin^2\theta = 0.25$ and two different values of $r_3 = 1.2\sigma$ and σ keeping the value of r_2 fixed at $r_2 = \sigma$. For a given value of θ, the potential energy $V_2 + V_3$ is lower for higher value of r_3. In addition to V_2 and V_3, there is also a four-body potential V_4 which is a shifted Lennard-Jones potential introduced to prevent branching and having a cutoff distance $2^{1/6}\sigma_4$. The behaviour of potential energy V_4 is shown in the inset of Fig.2.1(b). The vertical lines indicate $\sigma_3 = 1.5\sigma$ and $\sigma_4 = 1.75\sigma$. The vertical line (in blue) in the inset figure shows the cutoff distance of V_4 at $2^{1/6}\sigma_4$.

Thus, the model used here not only adds a semiflexibility to the chains but also prevent any form of branching in the chains by providing V_4 potential. Moreover, this form of potential gives us a control parameter σ_4 that can be used to control the excluded volume between micellar chains which is an advantage over other potentials used in the literature.

Though we refer to our model of the self-assembling polymeric system as a model of WLM, in practice, it could be used to model a general class of semiflexible equilibrium polymers formed by suitable aggregation of spherical beads, as we have not used any feature specific to WLM in our model. Our monomeric beads should be considered to be of a size much larger than that of amphiphilic molecules which constitute WLM.

2.1.2 Simulation method

There exist many simulation methods that simulate a soft matter system, e.g. lattice-gas (Wolf-Gladrow, 2004), lattice-Boltzmann (Higuera and Jimenez, 1989) methods which are widely used to study the hydrodynamics of the system while Molecular Dynamics (Haile, 1992) form another popularly used method to follow the actual trajectories of the system. In order to study the equilibrium properties of the system, the Monte Carlo method (Binder et al., 1993) is applied. In this study, we choose to investigate the equilibrium phase behaviour of the system using the Monte Carlo method.

Monte Carlo methods use randomness in the sampling, run for many iterations and use the law of large numbers to obtain the results (Graham and Talay, 2013). For complex systems involving large dimensions, a Markov chain Metropolis Monte

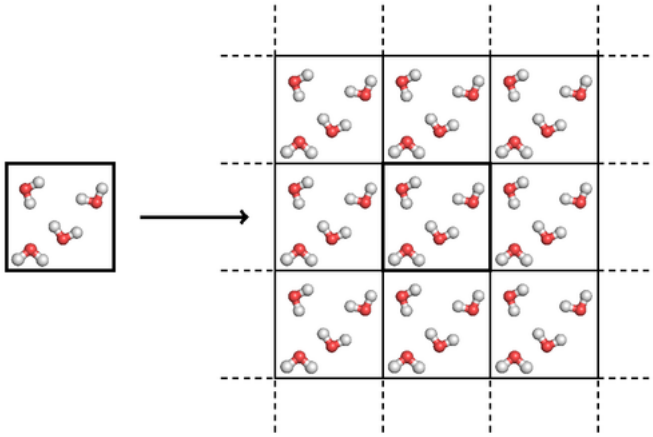

FIGURE 2.2: Periodic Boundary Condition: For a better representation of a realistic system representing a large number of particles in bulk, the original box is replicated on each side surrounding the central box. Under the periodic boundary conditions, each atom interacts with an atom that can be either in the same box or one of the neighbouring boxes.

Carlo method is preferably used which employ non-dynamic stochastic steps based on random moves of the system (Hastings, 1970). It is based on the detailed balance conditions, which says that the probability of moving from one state to another is the same as the probability of moving from the second state to the first state in the system when in equilibrium. For a system in thermodynamic equilibrium, the distribution of energies is given by Boltzmann distribution. Therefore to reach the equilibrium using Monte Carlo method, the probability of accepting any move from a state having energy E_1 to a state having energy E_2 is accepted by a biased thermodynamic probability of max $\{exp(-(E_2 - E_1)/k_BT)$,1$\}$.

2.1.3 Periodic Boundary Condition (PBC)

A finite number of particles simulated in a small simulation box produces boundary effects. For a better representation of a realistic system representing a large number of particles in bulk, the original box is replicated on each side surrounding the central one as shown in Figure 2.2. Under the periodic boundary conditions, each atom interacts with an atom that can be either in the same box or one of the neighbouring boxes which are called periodic image particles. This helps in elucidating a simulation of a system in bulk. Moreover, the cutoff distance for the interaction is chosen such that the interacting particle does not see its own image in the surrounding box. To calculate potentials, calculating the neighbouring distances to find out particles under the potential range each time, increases the computational cost. Therefore a neighbour list is maintained which ensures that all the neighbouring particles are considered in the list with many more particles so that all the neighbours are accessible to the central particle till a new neighbour list is created.

2.1.4 Results: Isotropic to Nematic Transition

Figure 2.3a and 2.3b shows snapshots of 6000 and 7500 monomers, respectively, in a $30 \times 30 \times 60\sigma^3$ simulation box after the system is equilibrated using Monte

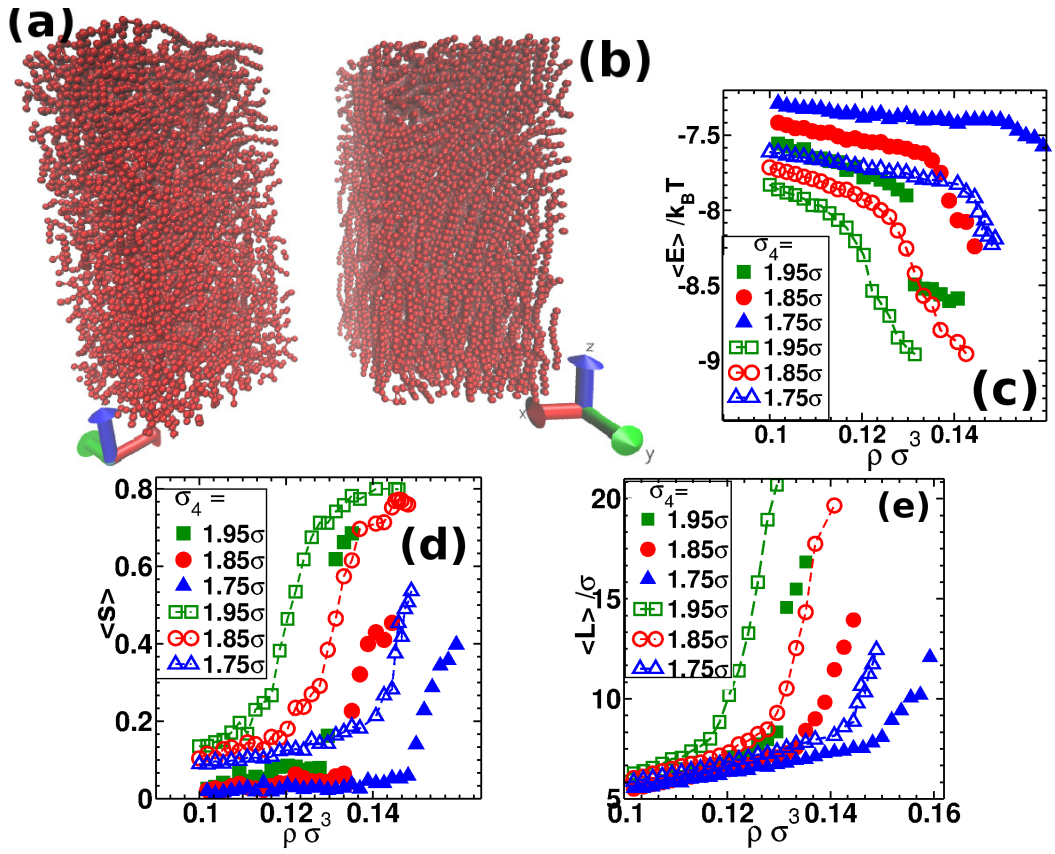

FIGURE 2.3: (Color online) Representative snapshots of (a) isotropic and (b) nematically ordered phase of self-assembling monomers forming worm-like micelles(WM). The number of monomers are 6000 and 7500, respectively, in a $30 \times 30 \times 60\sigma^3$ box for a small symmetry breaking field $B_n^2 = 0.025 k_B T/\sigma^2$ and $\sigma_4 = 1.95\sigma$. To identify the isotropic-nematic transition densities plots of average energy $\langle E \rangle$, the average nematic order parameter $\langle s \rangle$ and the average length $\langle L \rangle$ versus the number density $\rho_m \sigma^{-3}$ is shown in subfigures (c),(d) and (e), respectively. We explore the transition for three different values of EV diameter σ_4 at $B_n^2 = 0.025 k_B T/\sigma^2$ (filled symbols) and $0.1 k_B T/\sigma^2$ (empty symbols).

Carlo (MC) Metropolis algorithm. The low-density equilibrium configuration is a disordered isotropic phase with small chains. We have checked that an exponential distribution of chain lengths is obtained as expected (Cates and Candau, 1990b). To obtain the nematically ordered phase with long chains as shown in Fig. 2.3b, we have used a symmetry breaking field B_n which adds an energy $E_B = -(\hat{r}_2 \cdot \vec{B}_n)^2$ to the Hamiltonian; B_n acts only if $|\vec{r}_2| < \sigma_3$. We use $B_n^2 = 0.025 k_B T/a^2$, which biases $\vec{r}_2$ to allign along $\hat{z}$.

In Figure 2.3 c, d and e we have identified the range of densities over which the isotropic to nematic (I-N) transition occurs by plotting the average energy $\langle E \rangle$ of the monomers, the average nematic order parameter $\langle s \rangle = \langle 3/2 \cos^2(\phi) - 1/2 \rangle$ and the average length of chains $\langle L \rangle$ as a function of number density ρ_m of monomers. The angle ϕ is the angle between a bond vector connecting adjacent monomers in a chain and $\hat{z}$. Since, the average of $cos(\phi)$ is $1/\sqrt{3}$ for a completely random configuration, the expression for <s> normalizes the value from 0 to 1 corresponding to a completely random configuration to an alligned configuration of chains. All the quantities show a sharp increase/decrease at the transition, i.e., for values of $\rho_m > 0.12\sigma^{-3}$. An increase in σ_4, which increases the volume excluded by the chains, makes the transition sharper and also shifts it to lower densities. To assure ourselves of the robustness of our results, we carried out simulation for $B_n^2 = 0.1 k_B T/\sigma^2$ as well as lower value of $B_n^2 = 0.025 k_B T/a^2$ in boxes of $30 \times 30 \times 30\sigma^3$ and $30 \times 30 \times 60\sigma^3$, respectively. A previous detailed study using a potential similar to this model had established a weakly first-order isotropic to nematic phase transition (Chatterji and Pandit, 2001b). In the present study, we use the same term V_4 to vary EV of chains as well as to avoid branching of chains. Thus, V_4 is a very useful addition to V_2 and V_3 terms. Moreover, since there is no discontinuity in the force at σ_3, the combined potential is useful to study dynamical properties using MD simulations. We keep $\sigma_4 = 1.75\sigma$ in a box of $30 \times 30 \times 60\sigma^3$ and the $B_n^2 = 0.1 k_B T/\sigma^2$ fixed, for results presented hereafter.

2.2 Nanoparticles in a wormlike micellar matrix

2.2.1 Model

To explore the self-organization of nanoparticles (NPs) inside the model wormlike micellar matrix (or EP matrix discussed in the previous section), we need to introduce a suitable model for NPs. The NP-NP interactions are modelled by a Lennard-Jones potential for particles of size σ_n,

$$V_{2n} = \epsilon_n[(\frac{\sigma_n}{r_n})^{12} - (\frac{\sigma_n}{r_n})^6]; \forall r_n \leq r_{cn}, \tag{2.4}$$

where, r_n is the distance between the centres of two interacting NPs. The potential V_{2n} is shifted such that it goes smoothly to zero at the cutoff distance $r_{cn} = 2\sigma_n$. The interaction between NPs and micellar monomers at a distance r is modelled by a repulsive WCA (Weeks-Chandler-Anderson) potential given by,

$$V_{4n} = \epsilon_{4n}[(\frac{\sigma_{4n}}{r})^{12} - (\frac{\sigma_{4n}}{r})^6], \forall r \leq 2^{1/6}\sigma_{4n}. \tag{2.5}$$

The strength of attraction for the above potential is kept to be $\epsilon_{4n} = 30 k_B T$. The value of σ_{4n} here defines the minimum approaching distance between a NP and a monomer. Therefore, it is used as EVP between micelles and NPs. Since the

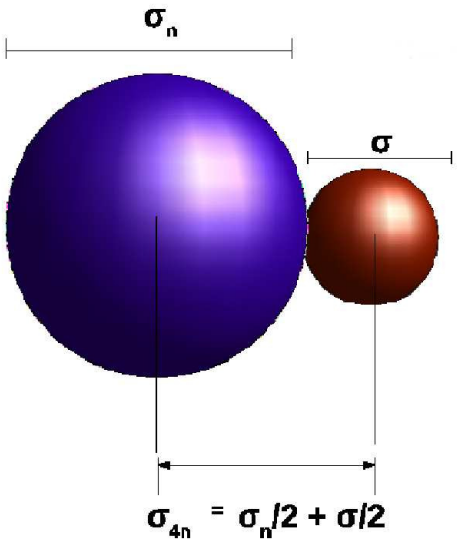

FIGURE 2.4: The figure is a schematic diagram to explain the role of the parameter σ_{4n} by which we control the excluded volume of the monomers when they interact with nan-particles. The parameter σ_{4n} is shown as the minimum approaching distance between nanoparticles and monomers and calculated as $\sigma_{4n} = \sigma/2+\sigma_n/2$. For monomers of diameter σ and nanoparticles of diameter $\sigma_n = 1.5\sigma$, the minimum allowed value of σ_{4n} is $(\sigma_{4n})_{min} = 1.25\sigma$. We use σ_{4n} as a parameter and we choose values $\sigma_{4n} \geq 1.25\sigma$ keeping $\sigma_n = 1.5\sigma$ fixed.

monomers and NPs of diameters of σ and σ_n are considered to be nearly impenetrable, the EVP cannot be less than $\sigma/2 + \sigma_n/2$. Thus, there exists a lower bound for the variable σ_{4n} and it can only have values $\sigma_{4n} \geq \sigma/2 + \sigma_n/2$. This is explained in Fig.2.4. In summary, the model has a fixed value of monomer diameter σ and NP diameter σ_n $(= 1.5\sigma)$ with the minimum approaching distance between them σ_{4n} used as a variable along with monomer number density ρ_m . All the other values are kept constant. The polymeric matrix thus modelled is equally applicable for a wormlike micellar matrix or any other equilibrium polymeric matrix.

2.2.2 Simulation method to study WLM+NP system

To study the behaviour of WLMs and NP system, we randomly place model monomers and NPs with a fixed volume fraction in a box of size $V = 30 \times 30 \times 60\sigma^3$ with periodic boundary conditions where the unit of energy is set by choosing $k_BT = 1$. We used the Monte Carlo method (Metropolis algorithm) to evolve the system towards equilibrium. For a high-density regime, the Metropolis Monte Carlo moves seemed to be inefficient to equilibrate the system. Therefore, the system is first allowed to equilibrate for 10^5 iterations with a few (100-200) NPs inside it so that monomers can self-assemble in the form of chains in the presence of the seeding of NPs. Once the chains are formed in the presence of seeded NPs (10^5 iterations) then, a semi-grand canonical Monte Carlo (GCMC) scheme is switched on for the rest of the iterations. According to this scheme, every 50 Monte Carlo Steps (MCSs), 300 attempts are made to add a NP at a random position or remove a randomly chosen NP in the system. Each successful attempt of adding or removing a NP is penalised by an energy

gain or loss of μ_n respectively, which sets the chemical potential of NP system. Thus, the value of μ_n controls the number of NPs in the system. A higher(or positive) value of μ_n leads to the lower number of NPs getting introduced into the system and vice versa.

Note that such a scheme violates detailed balance necessary for equilibrium, so this Monte Carlo scheme should be considered as a system where the NP + EP system tries to relax to equilibrium for 50 MCS, but then the simulation box is being put in contact with a NP-bath periodically. At these points of the MC-run, we try to introduce or remove NPs using Boltzmann factors. Nevertheless, the system becomes essentially a non-equilibrium system which is periodically exposed to a NP-bath for particle exchange every 50 MCS. The system is evolved with the GCMC scheme for 2×10^6 to 4×10^6 iterations and the thermodynamic quantities considered are averaged over ten independent runs. The next two chapters describe the effect of σ_{4n} and ρ_m on the WLM+NP system using this method.

Chapter 3

Effect of excluded volume parameter σ_{4n} on the wormlike micelle nanocomposite system

3.1 Introduction

There is persistent interest in the controlled self-assembly and growth of nano-structures of predefined morphology and size starting from small constituent nanoparticles (NP) (Frenkel and Wales, 2011; Curk et al., 2014; Lopes and Jaeger, 2001; Whitesides, Mathias, and Seto, 1991; Lu et al., 2008; Zaccarelli et al., 2008; Araki and Tanaka, 2006; Shchukin and Bimberg, 1999; Charleux et al., 2012; Zhang and Glotzer, 2004; Grzelczak et al., 2010a; Whitmer et al., 2013a; Moreno-Razo et al., 2012; Whitmer et al., 2013b; Gupta, Mehra, and Thaokar, 2012; Grzelczak et al., 2010b; Palma, Cecchini, and Samorì, 2012; Kim and Alexander-Katz, 2011; Starr, Douglas, and Glotzer, 2003; Pryamtisyn et al., 2009; Spaeth, Kevrekidis, and Panagiotopoulos, 2011; Rahedi, Douglas, and Starr, 2008; Mani et al., 2012; Li et al., 2012; Horsch, Zhang, and Glotzer, 2005; Parviz, Ryan, and Whitesides, 2003; Ozin et al., 2009b; Leontidis et al., 2003; Gharbi, Nobili, and Blanc, 2014). A separate non-alligned interest of physicists is in the formation and properties of topological defects when large particles (large compared to the size and spacing between nematogens) are introduced in ordered liquid crystalline nematic and smectic phases (Gharbi, Nobili, and Blanc, 2014; Zapotocky et al., 1999; Poulin et al., 1997; Ramos et al., 1999; Senyuk et al., 2013; Fukuda, Žumer, et al., 2009; McCoy et al., 2008; Muševič and Škarabot, 2008; Ravnik and Žumer, 2009; Tkalec et al., 2009; Škarabot et al., 2008; Zhou, Yue, and Feng, 2008; Stark, 2001). Recent experiments have also explored the self-organization of nanoparticles in a background matrix of the nematically ordered micellar phase, but constraints in the choice of size of NP led to the following two scenarios: small NPs of $2-3$ nm diameter pervade the nematic chains themselves and form a dispersion/solution whereas larger NPs of size $8-26$ nm get expelled by the elastic energy of ordered nematic phases and aggregate at the grain boundaries between nematic domains (Sharma et al., 2009a; Sharma, Aswal, and Kumaraswamy, 2010). The distance between adjacent nematic chains was 5.7 nm in the experiments.

Our present study spans across these two different research domains, and we use computer simulations to investigate the hierarchical self-assembly of NPs in the free volume between parallel chains of nematically ordered worm-like micelles (WM). WM is one of the experimental realizations of the class of polymers known as equilibrium polymers. In this work, the micellar polymeric systems are self-assembled themselves from "effective coarse-grained" monomeric beads and have a length and

size distribution controlled by monomer density and temperature (Cates and Candau, 1990b; Berret, 2004; Lerouge and Berret, 2010). In a computer simulation, we are able to systematically vary the diameter, the chemical potential of the spherical NPs as well as the excluded volume (EV) by the self-avoiding semiflexible chains inside which the NPs self-assemble. Thereby, we observe the effect of the above parameters as well as the elasticity of the background polymer matrix on the morphology and size of the nanostructures of self-organized NPs. The nanostructured aggregates, in turn, increase the effective density of monomers constituting the background matrix and make them more nematically ordered with longer chains spanning the length of the system. The use of nematically ordered WM/equilibrium polymers as a background matrix is different from using a simple nematic phase of anisotropic particles as the background template. This is because the polymeric matrix will form a more energetically stable but locally flexible framework as compared to a matrix made up of aligned long rigid rods. The cost of breaking a bond in WM is a few times k_BT, whereas there is no local energy cost to introduce a NP between the ends of two anisotropic particles.

At suitable densities and radii of NPs we get rod-like aggregates of different aspect ratios shaped by the geometry of the background matrix: EV and elastic energy costs of accommodating the NPs amongst the semi-flexible polymeric micelles encourage the NPs to form aggregates even at moderate number densities. Since the background matrix is not only deformable but also prone to scission and recombination, neighbouring rod-like aggregates of NPs can also fuse, at times, forming porous percolating networks of extended tubular structures. In experimental realizations of our studies, these nanostructures could be stable due to van der Waals attraction even if the background micellar matrix is dissolved away by adding suitable ions in solution by reverse-micellization as in (Hegmann, Qi, and Marx, 2007; Wang, Chen, and Jiao, 2009). To our surprise, we also get a perfectly crystalline phase spanning the simulation box where both NM and the WM forming monomers form alternate lines of NP and monomers forming closed packed structures. In the following, we describe the different nanostructures obtained as a result of the change in the excluded volume parameter σ_{4n} and summarize the conditions under which the different assembled structures are formed.

3.2 Method

To study NP microstructure formation in a matrix of nematic polymers, we start introducing NPs amidst the pre-formed nematically ordered chains as discussed in section.2.2.2. The monomers self-assemble into ordered WMs within 10^5 MC steps starting from a random initial configuration of 6800 monomers and 100 NPs. Then we attempt to add (remove) randomly chosen NPs 300 times every 50 MC steps for the rest of the MC steps.

We perform grand canonical MC (GCMC) simulations with the number of monomers fixed, but with an energy gain (*loss*) of $-\mu_n(\mu_n)$ for each added (*removed*) NPs in the simulation box where μ_n is the chemical potential. The equilibrium phase of the micelles and NPs is the phase separated structure as seen in Fig. 3.1a and b for low densities of monomers and NPs with $\mu_n = -0.48k_BT$, 4800 monomers, $\sigma_{4n} = 1.75\sigma$, $\sigma_n = 2\sigma$ and $\epsilon_n = 10k_BT$. By virtue of periodic boundary conditions, one can discern that there is only one single phase separated aggregate of monomeric chains.

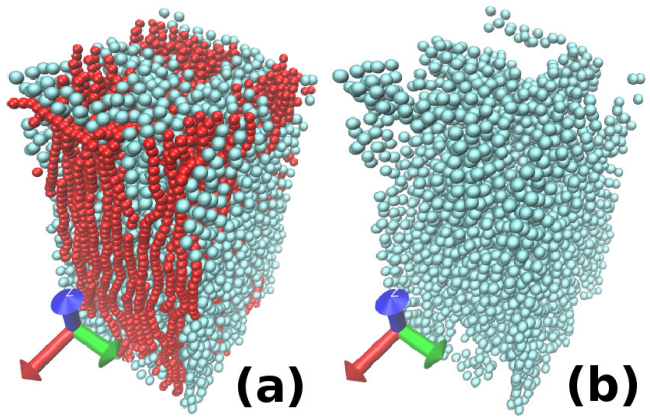

FIGURE 3.1: (Color online) Snapshots of WM chains (red/dark coloured) and structures formed by aggregates of nano particles-NP (blue/light coloured) are shown. The snapshot in b is exactly the same snapshot of a, with monomers made invisible to have unhindered view of NPs. (a) and (b) show an equilibrated phase separated configuration with 4200 monomers and $\mu_n = -0.48k_BT$ and $\epsilon_n = 10k_BT$ for NPs with $\sigma_n = 2\sigma$, $\sigma_{4n} = 1.75\sigma$ in a $30 \times 30 \times 60\sigma^3$ box.

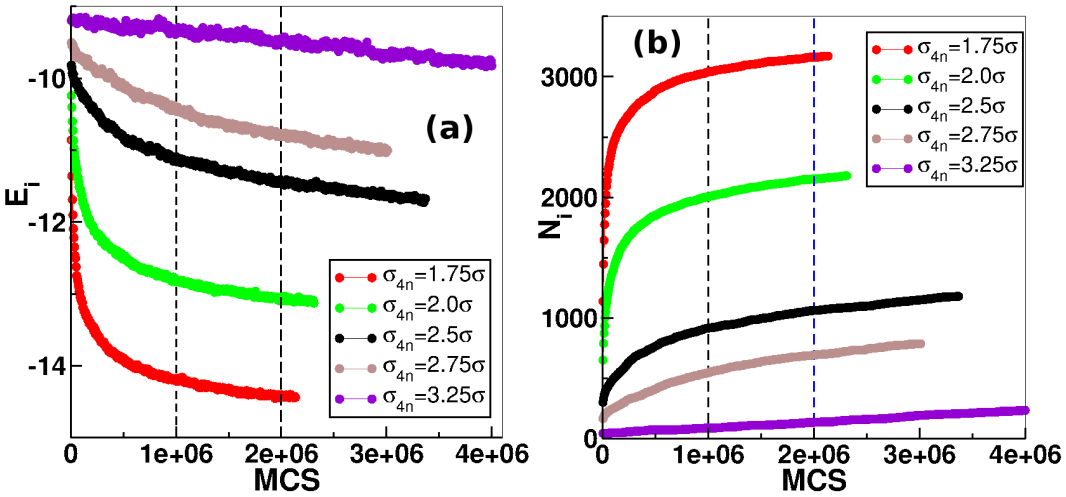

FIGURE 3.2: (Color online) Slow relaxation of (a) instantaneous energy E_i per particle in units of k_BT and (b) instantaneous number of NPs N_i of radius $\sigma_n = 2\sigma$, versus the number of Monte Carlo steps (MCS) in the simulation box of $30 \times 30 \times 60\sigma^3$ with 6800 monomers for different values of σ_{4n}. The values of ϵ_n and μ_n is kept fixed at $14k_BT$ and $16k_BT$, respectively, the same as that for data presented in the next figure: Fig.3.3.

For denser systems with $\mu_n > 0$, 6800 monomers and $\epsilon_n = 14k_BT$, we observe aggregation of NPs between micellar chains in our simulations. However, kinetic barriers in this dense glassy systems are too high to enable the system to phase separate completely, but GCMC steps for NPs help overcome energy barriers in configuration space allowing them to aggregate locally in space: dynamically arrested phase separating structures stuck in a metastable free energy minimum. As we see in Fig.3.2 a and b, within 10^6 MC steps, the number and structure of NP-aggregates within the micellar matrix gets nearly determined, with very slow addition/relaxations of NPs (less than 2.5%) over the next 10^6 MC steps. The average energy E_i is calculated at the total energy of the system divided by the total number of monomers + NPs in the system at a particular Monte Carlo step (MCS). We have plotted data every 5000 MCS. A few NPs manage to get introduced in a million iterations in the existing clusters as more free volume could open up due to local positional rearrangement of monomers and NPs. Of course, to ensure the robustness of our conclusions, we gave many independent runs to cross-check that we get statistically similar structures of micellar chains and NP-nanostructures at the same set of parameter values.

The results presented hereafter are independent of the initial configuration of NPs and monomers, but we always start with randomly placed 100 seed nanoparticles in the box. After we start GCMC steps after the initial 10^6 iterations, clusters of NPs form around these seed NPs, but the number of NPs adjust itself according to the available free volume to form clusters which in turn in determined by σ_{4n}. In our work, we allow the number of NPs to fluctuate, but the number of monomers is kept fixed. We always specify the number density ρ_m of monomers in the text as we are unable to calculate exactly the volume fraction of micellar chains. The volume excluded by a segment of the chain, as determined by σ_{4n}, kicks in only when there are self-assembled micellar chains with more than three monomers in a chain. Thus the volume excluded by the chains will depend upon the distribution of chain length of the self-assembled monomers. An isolated monomer by itself will occupy a volume of a sphere of radius $\sigma/2$.

3.3 Self Organization of Nano-structures

In Figure 3.3 we show representative snapshots of self-assembled nanostructures formed by the aggregates of NPs in a matrix of nematically ordered WM chains. We keep $\epsilon_n = 14k_BT$, $\mu_n = 16k_BT$ and the NP diameter $\sigma_n = 2\sigma$ of NPs fixed, and gradually increase the excluded volume parameter σ_{4n} of the monomer-NP interaction. At the lowest value of $\sigma_{4n} = 1.5\sigma$ (Fig.3.3c, d), we get a phase where the NPs are arranged in a periodic manner separated by chains of WM monomers. The monomers and NP form crystalline domains (Cr) with alternate positions of NP and monomer chains. We calculated the structure factors for NPs which confirm a crystalline structure (refer to discussions later in this section). This phase occurs whenever the condition $\sigma/2 + \sigma_n/2 = \sigma_{4n}$ is satisfied. *Moreover*, enough free volume should be available for the NPs to fill up all the possible lattice sites. The free volume is dependent on both σ_{4n} and σ_n as well on the number density ρ of monomers. We have fixed ρ at $0.126\sigma^{-3}$ and σ_4 at 1.75σ, but the number of NPs can adjust to fill up the available space between WM chains. For other combinations of σ_{4n} and σ_n, we get a near perfect lattice arrangement of NPs; the reader can confirm later in the text.

The excluded volume parameter between monomers and NPs σ_{4n} can be considered as the radius of NPs "as seen by" monomers while σ_n is the radius of nanoparticles. The condition $\sigma/2 + \sigma_n/2 = \sigma_{4n}$ means that the size of NPs "as seen by"micellar

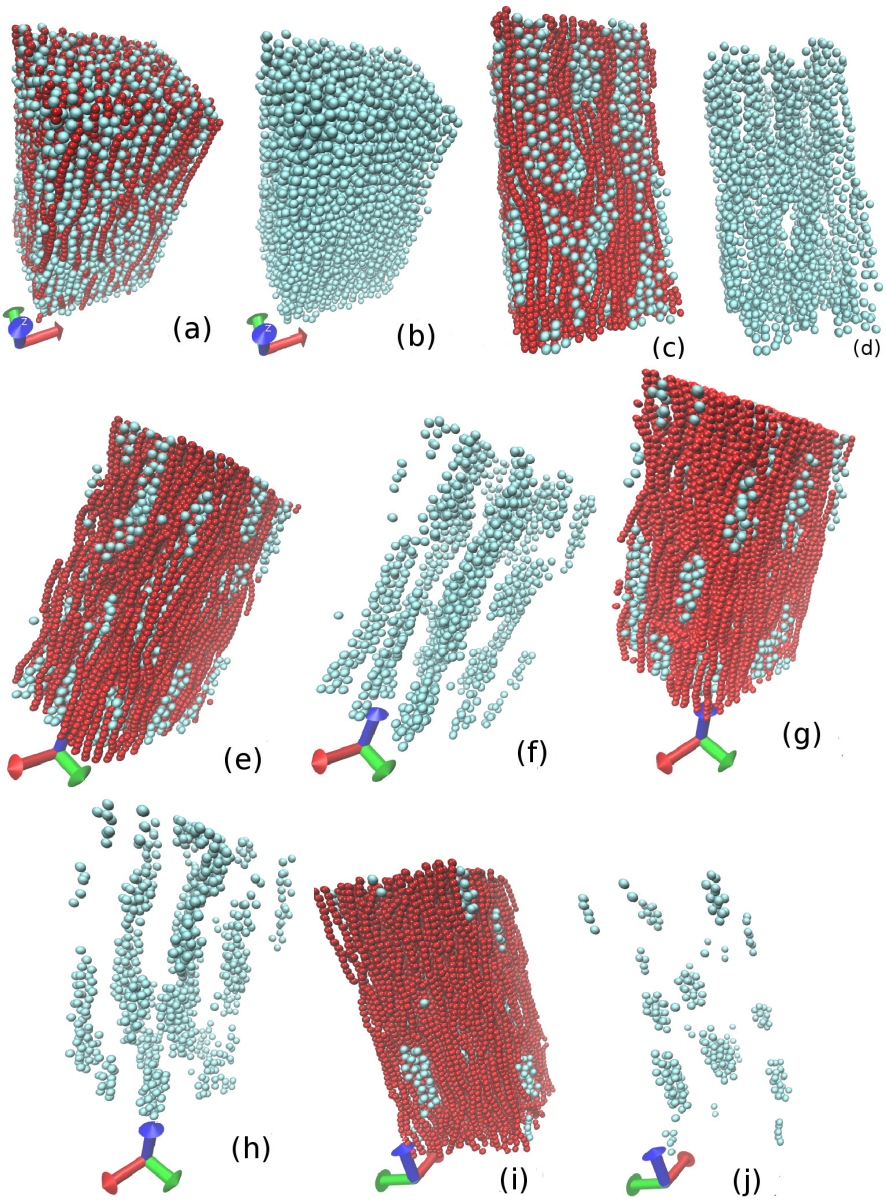

FIGURE 3.3: (Color online) Snapshots of WM chains (red/dark coloured) and structures formed by aggregates of nano particles-NP (blue/light coloured) are shown. The snapshots in b, d, f, h, j are exactly the same snapshots of a, c, e, g, i, with monomers made invisible. Snaphots (a) to (j) show dynamically arrested configurations of monomers and NPs; for these the values of μ, ϵ_n and the NP radius σ_n is kept fixed at $16k_BT, 14k_BT$ and 2σ, respectively. However, $\sigma_{4n} = 1.5, 2, 2.5, 2.75, 3.25$ is varied for $(a), (c), (e), (g), (i)$. The phases shown in snapshots a, c, e, g, i are crystalline (Cr), percolating network (P_n), elongated clusters (E), (E) but with shorter clusters, and aggregates (A), respectively. The volume fraction of NPs in (a) is 0.21 (2712 NPs), for c, e, g, i, k the NP-density is $0.38, 0.17, 0.092, 0.061, 0.018$, respectively. $B_n^2 = 0.1k_BT/\sigma^2$.

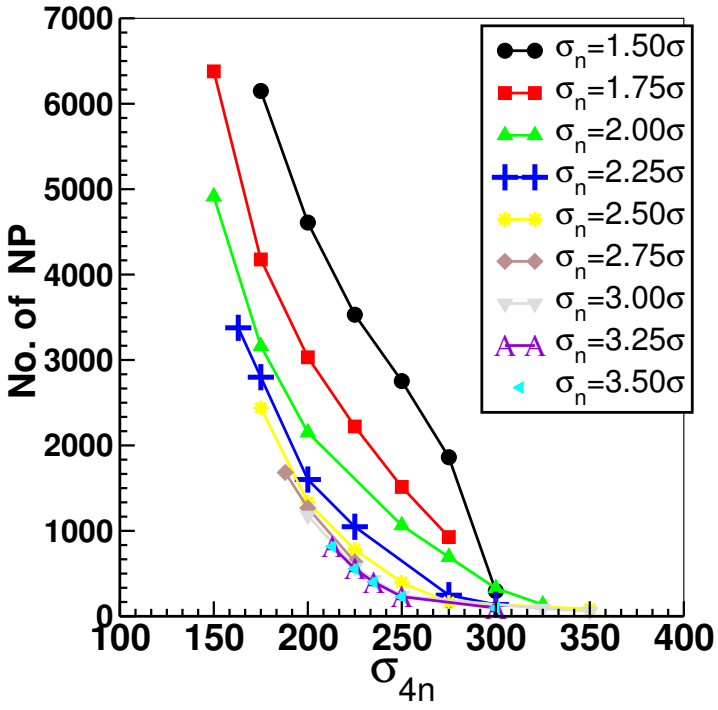

FIGURE 3.4: (Color online) The figure shows the decrease in the number of NPs available in the simulation box as the EV diameter σ_{4n} of micellar chains is increased. The data shown is for $\epsilon_n = 14k_BT$ and $\mu_n = 16k_BT$ for different values of the NP radius σ_n and data corresponds to the number of NPs at the end of the simulation run.

chains is same as the distance between micellar chains that will be maintained even in the absence of NPs. When this condition is satisfied, the micellar chains have the exact distance between them to accommodate a NP. That gives rise to a perfect(or near perfect) arrangement of the NPs and the chains. In any other case, when $\sigma_{4n} > \sigma/2 + \sigma_n/2$ a well-arranged system of micellar chains needs to be pushed(clustered) in order to accommodate a NP in between them. Therefore, the ordered structure is not maintained.

If now σ_{4n} is increased to 2σ from 1.5σ, a new structural arrangement of NPs is formed where the NPs start to phase separate to form percolating clusters of NPs which span throughout the system: refer Fig.3.3e and f. Kinetic trapping prevents complete phase separation, and we observe NP clusters separated by stacks of WM chains lead to morphologies which is akin to the percolating network (P_n) of NPs. If the WM phase was dissolved away at the end of the P_n phase formation, a porous scaffold of NP micro-structure would be retained similar to what is seen in Fig.3.3f. An increase of σ_{4n} will lead to elongated structures conjoined at fewer points in space with fewer NPs in the system, and finally at $\sigma_{4n} = 2.5\sigma$, we have even fewer NPs in the system which now formed non-percolating elongated clusters (E) of NPs spanning the $\hat{z}$ direction: refer Fig.3.3g and h. Clusters grow along the nematic direction to minimize elastic energy costs paid by nematically ordered WMs to accommodate NP clusters. A further increase in the value of σ_{4n} to 2.75σ leads to shorter and thinner elongated structures as shown in Fig.3.3i and j. Finally, small aggregates (A) dispersed in the nematic matrix are found for even larger values of $\sigma_{4n} = 3.25\sigma$ some of which are rod-like, as seen in Fig. 3.3k and l. For a further increase in σ_{4n}, it is not possible to introduce NPs in the nematic matrix. The decrease in the number

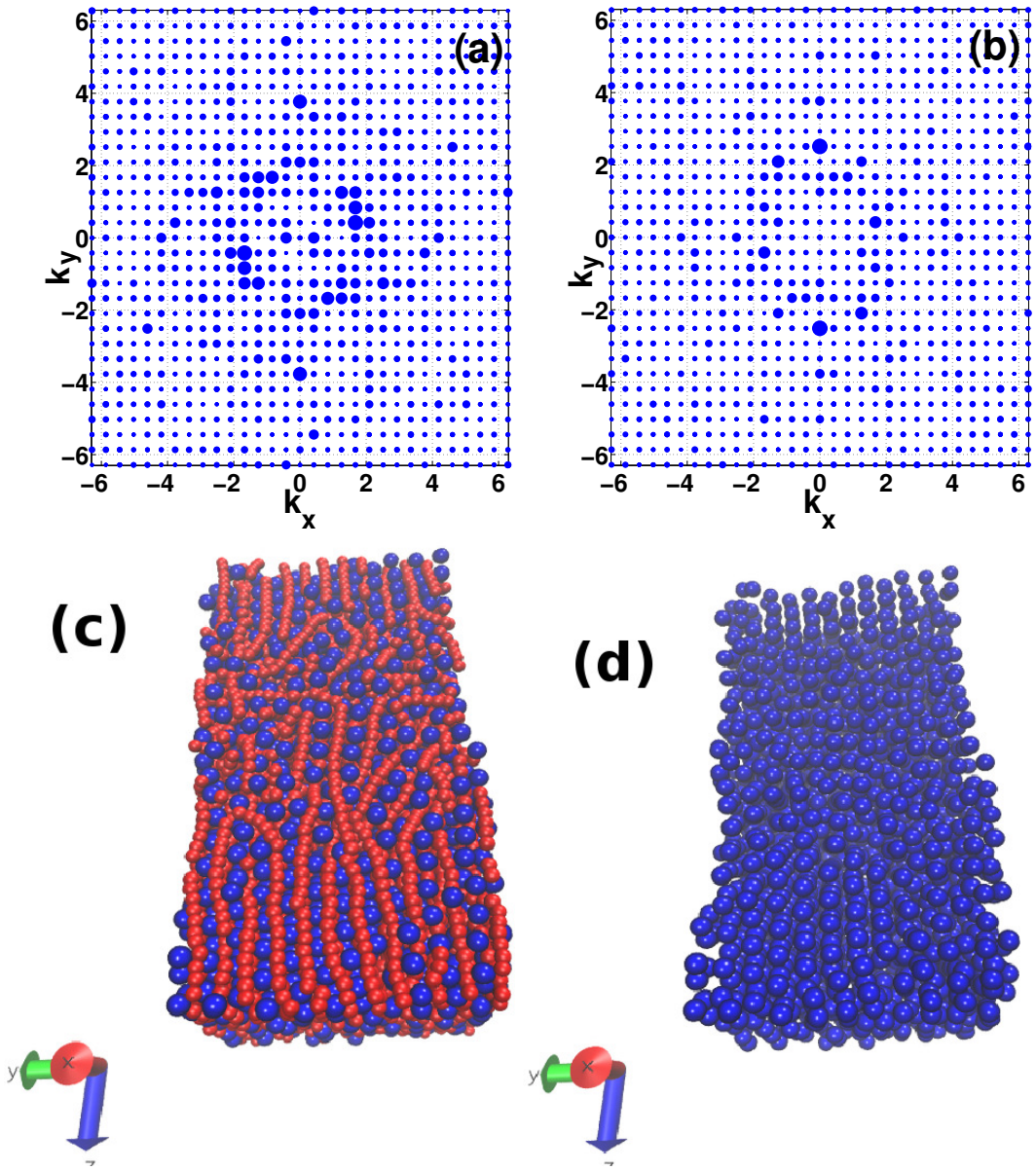

FIGURE 3.5: (Color online) (a) The structure factor $S(\vec{k})$, calculated for the snapshot shown in Fig.3.3 *b*, establishes local crystalline order of NPs. The bigger dots indicate a peak in $S(\vec{q})$ at the appropriate k_x, k_y values. Figure *b* shows $S(\vec{k})$ for another set of parameters for which a crystalline order is obtained (i.e., the condition $\sigma/2 + \sigma_n/2 = \sigma_{4n}$ is satisfied): $\sigma_n = 2.5\sigma, \sigma_{4n} = 1.75\sigma$ with μ_n and ϵ_n same as before, i.e. $\epsilon_n = 14k_BT$ and $\mu_n = 16k_BT$. Snapshot (c) shows the corresponding NP(blue/dark coloured) + monomers(red/light coloured) configuration. The snapshot without monomers shown is presented in (d).

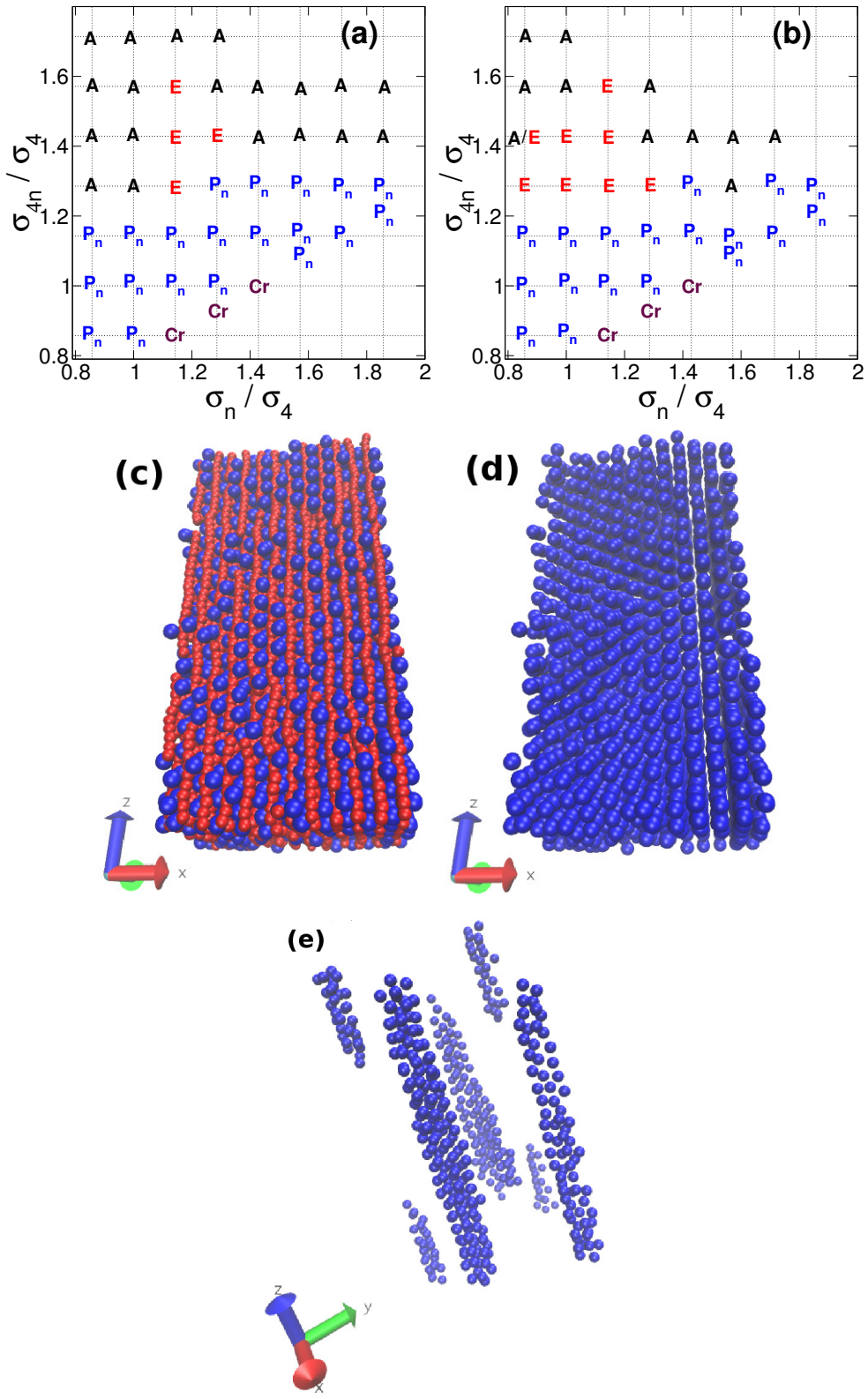

FIGURE 3.6: (Color online) The phase diagram denoting the different nanostructures formed as we change σ_{4n} and σ_n for $\epsilon_n = 14k_BT$ and (a) $\mu_n = 16k_BT$, (b) $\mu_n = 8k_BT$. Refer Fig. 3.3 for nanostructures nomenclature. Subfigure c and d shows near perfect lattice arrangement of NPs between planes of self-assembled monomer chains for $\sigma_n = 2.5\sigma$, $\sigma_{4n} = 1.75\sigma$; energies scales are $\epsilon_n = 30k_BT$, $\mu_n = 8k_BT$. The lattice structure spans the volume of the box. We show near perfect rod-like structures of NPs at $\sigma_n = 2\sigma, \sigma_{4n} = 2.75\sigma$ in subfigure e; $\epsilon_n = 14k_BT, \mu_n = 8k_BT$.

of NPs as we change σ_{4n} is shown in Fig.3.4. The number of NPs shown corresponds to the snapshot at the end of each simulation run. As discussed previously and as shown in Fig 3.2, the number of NPs increases very slowly after the first 10×10^5 Monte Carlo steps (MCS), hence we do not give the average number of NPs in the figure. The minimum number of iterations was at least 1.5 million MCS for each run. Smaller NP (σ_n) occupy less volume, so there is a larger number of NPs in the simulation box for the same value of EV diameter σ_{4n} of micellar chains.

We calculated suitable structure factors to confirm and substantiate that we truely obtain a crystalline phase of NPs interlocked with planes of micellar chains for the snapshots shown in Fig. 3.3a. We calculate $S(\vec{k}) = \left|\sum_n \exp^{-i\vec{k}\cdot\vec{r_n}}\right|^2 /N$ for the NPs and present it for two sets of parameters in Fig. 3.5 (a) and (b). The summation is over all the NP-particles and r_m is the position of the NP particles with respect to the origin. The peaks of $S(\vec{k})$ establish the periodic arrangement of NPs. The corresponding snapshots, with both NP and monomers shown in Fig. 3.5c and with NPs only shown in 3.5d for the parameter values used to calculate $S(\vec{q})$ in Fig. 3.5b, visually establish what can be inferred from the structure factor, i.e. the crystalline ordering is better than what is seen in Fig. 3.3a. However, one can discern that there a crystalline domain and a relatively disordered one in the simulation box.

We explore the (non-equilibrium) phase diagram of the nanostructures that we get as we vary σ_{4n} and σ_n for two values of μ_n, viz, $\mu_n = 16k_BT$ and $\mu_n = 8k_BT$ in Fig 3.6a and b. The quantities σ_{4n} and σ_n have been normalized by σ_4, the excluded volume diameter with which the WM chains 'see' each other. We have chosen σ_{4n} (the EV diameter between NP and micellar chain), to be different from σ_4 (the EV diameter between two chains of WM) to have an independent handle on changing NP-micellar chain interactions keeping the volume fraction on micellar chains fixed. In an experimental realization, σ_{4n} could be different from that of σ_4 due to differences in microscopic interactions (Hegmann, Qi, and Marx, 2007). We ensure that the lowest σ_{4n} chosen was such that $\sigma_{4n} \geq (\sigma + \sigma_n)/2$. As mentioned before, we get Cr arrangement of NPs when the condition $\sigma_{4n} = (\sigma + \sigma_n)/2$ is satisfied. At times, the lattice arrangement does not span the system and forms crystalline domains instead, as was seen in Fig.3.5c and d. This is because of unsuitable free volumes available to NPs in the micellar matrix. We have also obtained perfect crystal structures for $\epsilon_n = 30k_BT$, see Fig.3.6c and d. The combination of values of σ_n,σ and σ_{4n} again satisfy the above-mentioned condition for obtaining the crystalline order. As σ_{4n} is increased one gets the $\mathrm{P_n}$ phase and then the A phase for all values of σ_n when the free volume is enough to accommodate just a few small clusters of NP. However, there also exists an island of elongated clusters of NPs (E phase) in the phase diagram. The elongated NP clusters we show in Fig.3.6(e) are perfectly rod-like for $\mu_n = 8k_BT$ corresponding to $\sigma_n/\sigma_4 = 1.14$ and $\sigma_{4n}/\sigma_4 = 1.57$: this is shown in figure 3.6e.

3.4 Discussion

In summary, we have used semi-grand-canonical simulations to demonstrate the aggregation and growth of nanoparticle clusters with different morphologies. The NP-clusters get dynamically arrested within self-assembled chains of semiflexible worm-like micelles. The different nanostructures obtained are (a) a crystalline arrangement of NPs and monomers, (b) percolating networks of aggregated NPs creating a porous structure, (c) elongated rod-like structures of NPs whose length and aspect ratio can be varied, and (d) smaller clusters of different shapes and sizes.

In contrast to systems investigated previously, the size and densities of NPs in this work are such that NP-clusters and micellar matrix mutually affect and modify each other's local morphology and structure. We get different nanostructures by varying the EV of micellar chains seen by NPs, as well as the NP radius.

Systematic and anticipated changes in the morphology of nanostructures as we vary σ_n, σ_{4n} or even ϵ_n gives us confidence in the robustness of the results presented in this chapter. This is in spite of the fact that the nanostructures vary slowly, but surely, get modified with time as more NPs get gradually added at a very slow rate. However, we emphasize that we checked by giving very long runs that morphologies that we report are stable. What gives us further confidence, is that experimental realizations of the system that we have modelled have been reported very recently in literature (Sharma et al., 2011; Sharma et al., 2013; Kumaraswamy and Sharma, 2013). The experiments observe a scaffold of percolating network of nanostructures as well as elongated structures after the amphiphilic molecules of WM were washed away, similar to what we observe in our simulations.

The potential which we newly developed to model the coarse-grained self-assembly of WLM is extremely versatile and it enabled us to perform a systematic investigation of the self-organization of NPs as a function of the diameter σ_n of NPs and the excluded volume of the micellar chains. We can use the same term V_4 in the model potential to prevent branching as well as tune the excluded volume interaction between chains. Furthermore, the use of independent values for σ_4 and σ_{4n} allows us to control the minimum distance of approach of monomer and a NP, respectively, to the same micellar chain.

In the future, we plan to investigate the dynamics of micelles under shear and the use of rate constant as a parameter could affect the dynamics of association/dissociation/relaxation of the self-assembled polymers.

The strong clustering tendencies of the NPs are driven by $\epsilon_n = 14k_BT$ with a Lennard Jones potential minima of $3.5k_BT$. Since a NP is surrounded by a few neighbouring NPs, the energy of attractive interaction between NPs could be significant. We chose the number density of monomers such that the system was near the isotropic-nematic transition. We needed high values of μ and attractive interaction between NPs to be able to introduce NPs by overcoming EV interactions between NPs and monomers. In the future, we also plan to vary the monomer number density of the micellar monomers, which forms the matrix. Furthermore, we would like to increase the scope of the current work to investigate the NP-structures obtained with weak attraction between nanoparticles or just purely repulsive EV interaction between NPs.

Chapter 4

Effect of ρ_m on the self-assembly of WLM-nanoparticle system

4.1 Introduction

Nanoparticle assembly inside a polymeric matrix is a powerful route to form hybrid materials with the desired material, magnetic, optical and electronic properties by a suitable choice of system parameters (Miyashita, 2004; Black et al., 2006; Orski et al., 2011; Shenhar, Norsten, and Rotello, 2005; Zhang, Drechsler, and Müller, 2004; Jayaraman and Schweizer, 2009; Thompson et al., 2002; Sun et al., 2002; Haryono and Binder, 2006; Lin et al., 2005; Rozenberg and Tenne, 2008). The synergistic interaction between nanoparticles and the polymer matrix gives rise to a variety of hybrid systems and nanostructures having a wide range of applications like in cosmetics (Arraudeau, Patraud, and Gall, 1989; Tatum and Wright, 1988; Gadberry, Hoey, and Powell, 1997; Patel et al., 2006; Lochhead, 2008; Corcorran, Lochhead, and McKay, 2004; Laufer and Dikstein, 1996; Lochhead, 2007; Katz, 2007; Miller, 2006; Raj et al., 2012), food (Sorrentino, Gorrasi, and Vittoria, 2007; De Azeredo, 2009; Rhim, Park, and Ha, 2013; Arora and Padua, 2010; Ray et al., 2006; Sozer and Kokini, 2009), pharmacy (Sambarkar, Patwekar, and Dudhgaonkar, 2012; Ray and Bousmina, 2006; Mouriño, 2016; Dwivedi, Narvi, and Tewari, 2013), novel functional materials (Ingrosso et al., 2010; Segala and Pereira, 2012; Striccoli, Curri, and Comparelli, 2009; Mazumdar, Rattan, and Mukherjee, 2015; Carotenuto and Nicolais, 2004; Qi, 2017), ultraviolet lasers (Bloemer and Scalora, 1998; Jakšić, Maksimović, and Sarajlić, 2004; Scalora et al., 1998; Kedawat et al., 2014), hybrid nanodiodes (Gence et al., 2010; Park, Chung, and Mirkin, 2004; Das and Prusty, 2012), DNA templated electronic junctions (Turberfield, 2003; Park et al., 2004), quantum dots and thin wires (Alam, Siddiqui, Husain, et al., 2013).

The discovery of the mesoporous material MCM-41 by Mobil Oil Corporation (Kresge et al., 1992) widely popularised the method of assembling nanostructures inside polymeric matrices and thus giving rise to the "bottom-up" approach which revolutionised the whole industry of nanofabrication (Seul and Andelman, 1995; Tang et al., 2006; Van Workum and Douglas, 2006; Bedrov, Smith, and Li, 2005; Shay, Raghavan, and Khan, 2001; Fejer and Wales, 2007; Glotzer and Solomon, 2007; Lee et al., 2004). Polymeric and other supramolecular matrices have long been explored as templates for fabricating nanostructures due to low cost and ease of tailoring nanomaterials with the desired properties. Later, realising the importance of synergistic interactions between nanoparticles (NPs) and the matrix, a myriad of synergistically assembled nanocomposites have also been generated. The NPs can be incorporated in a matrix by both in situ (Xu et al., 2017; Sun and Yang, 2008) or ex-situ (Guo et al., 2014) methods. However, due to high surface interactions between NPs, it is difficult to disperse NPs inside the matrix. Therefore, in situ method is preferably

used to produce a homogeneously dispersed NP-matrix composite. Nanorods (Luo et al., 2006; Abyaneh, Parisse, and Casalis, 2016; Cao and Wang, 2004), nanowires and nanobelts (Wang, 2013), nanocombs and nanobrushes (Umar, Kim, and Hahn, 2008; Lao et al., 2006; Singh et al., 2010), nanosheets (Pandey et al., 2016; Vyborna et al., 2017), nanoporous (Xu, 2013) and mesoporous structures (Ying, Mehnert, and Wong, 1999), nanotubes, spherical and complex morphological nanostructures have been reported in the literature. However, to exploit NP properties for nanodevice fabrication, the control over their morphological structures is still a big challenge to the researchers. In this chapter, we report the transformation in the nanostructure morphology with the change in the polymeric matrix density and the excluded volume parameter between nanoparticles and polymers.

Generally, the (thermotropic) polymeric matrices have a value of elastic constants (for splay, twist or bend) of the order of $\approx 10pN$ (Sharma et al., 2009b). But there exists a class of polymers known as lyotropic systems showing interesting phase behaviour due to their low value of elastic constants ($\approx 1pN$) (Ramos et al., 2000; Sallen et al., 1995). Wormlike micelles (WLM) is one of the examples of such systems. When the concentration of the surfactant molecules in the presence of suitable salts becomes higher than a critical micellar concentration, the surfactant molecules then aggregate to form micelles. For appropriate shape and size of the surfactant molecules, they can aggregate into long thread-like polymeric wormlike micelles (Berret, 2006b). They possess an extra mode of relaxation by scission and recombination reactions giving rise to an exponential distribution of their polymeric length (Berret, 2006b; Turner and Cates, 1990; Cates, 1990). Moreover, the average spacing of WLMs in a hexagonal H1 phase is 5-10 nm, which is much larger than that of a thermotropic polymeric matrix (Ramos et al., 2000; Sharma et al., 2009b). Thus a low value of elastic constant, extra mode of relaxation and characteristic mesoscopic length scales makes the wormlike micellar matrix different from a thermotropic polymeric matrix. Therefore, the wormlike micelles have the potential to produce interesting mesoscopic structures of nanoparticles that have not been observed in polymeric matrices. In this chapter, we study the hierarchical self-organization of NPs in a model of a self-assembling polymeric matrix that mimics the characteristic behaviour of a wormlike micellar matrix. Our generic model of self-assembling polymers represents the class of polymers known as equilibrium polymers, WLMs at mesoscopic length scales are just an example of equilibrium polymers. Equilibrium polymers are those whose bond energies are of the order of the thermal energies k_BT, and thereby chains can break or rejoin due to thermal fluctuations.

We study the effect of the addition of NPs with diameters of the order of the diameter of equilibrium polymer (EP) chains on the polymeric self-assembly, which in turn affects the NP self-organization. The parameters which are systematically varied in our investigations are (1) the volume fractions of the polymeric matrix and (2) the minimum distance of approach between NPs and the matrix polymers (EVP - Excluded Volume Parameter). We show that for a low value of EVP, a uniformly mixed state of polymers and NPs is observed for all the densities of equilibrium polymers considered here. An increase in the value of the EVP leads to the formation of clusters of polymeric chains which joins to form a percolating network-like structure. The network of nanoparticles breaks into non-percolating clusters of NPs at some higher value of the EVP. We are able to present these morphological transformations in a diagram. There exist reports of a sudden decrease in the measured conductivity of polymer-nanocomposites in the literature (Li et al., 2010; Ambrosetti, 2010). This decrease in the conductivity is attributed to the transition of NPs from percolating to non-percolating state on a decrease in NP volume fraction (Li et al., 2010;

Ambrosetti, 2010). In an attempt to explain these morphological transformations, we propose that these morphological transitions are due to the competition between the repulsive interaction between nanoparticles and the polymeric matrix and the repulsion between polymeric chains themselves. We try to explain this by analyzing the behaviour of total excluded volume in the system. We thus present how the system parameters can be used to tailor the mesoporous nanostructures formed in the system. This has a great potential to optimize the shape and size of nanostructures obtained by in-situ methods and there improve the design and performance of fuel cells and batteries (especially Li-ion batteries), drug delivery, optoelectronic devices and other device-properties which depend on the nanostructure morphology.

The following section presents the potentials used to model NPs and equilibrium polymeric matrix and gives the details of the computational method. In the 3rd section, we briefly summarize our results which were published previously. In the next section, we present our new results which are divided into five sub-sections where we prove the robustness of our results and then give a detailed qualitative and quantitative analysis of the model system. We investigate the variation in EP number density and the minimum approaching distance between polymers and NPs and its effect on the system behaviour. We present our Conclusions in the last section.

4.2 Method

We use the model micelles and nanoparticles as described in Chapter.2. In a box of $30 \times 30 \times 60\sigma^3$, a fixed volume fraction of monomers is placed randomly. The monomers are allowed to equilibrate with a few NPs using the Monte Carlo method for 10^5 iterations. Then the system is evolved by using the GCMC method, which is described in Chapter 2. The resulting system morphology is tested with ten independent runs for each set of system parameters considered. The system is evolved with the GCMC scheme for 2×10^6 to 4×10^6 iterations and the thermodynamic quantities considered are averaged over ten independent runs. For the lowest value of σ_{4n} used, i.e. $\sigma_{4n} = 1.25\sigma$, a rapid introduction of a large number of NPs into the box was observed as soon as GCMC was switched on. This led to a large number of NPs ($\approx 10^4$ or more) in the simulation box and shorter runs. After the number of NPs in the simulation box had relatively stabilized, the acceptance rate of GCMC attempts for the addition of NPs was $\sim 5\%$, with a slightly lower rate of removal of NPs from the simulation box, which resulted in a net 0.1% addition of particles in the box. For the higher values of σ_{4n}, the rate of GCMC acceptance for addition of NPs is $10 - 20\%$ and also reaches to 30% in case of $\sigma_{4n} = 3.5\sigma$. The acceptance rate of attempts to remove NPs also remains approximately the same resulting in the net $0.02 - 0.07\%$ rate of addition of NPs. Therefore, the net rate with which NPs are added decreases with an increase in σ_{4n}.

We emphasize that we get statistically similar morphologies from each of the ten independent runs. Algorithms are used to find out whether the nanoparticle structure is percolating or non-percolating. Moreover, these morphologies have been analyzed and averaged over a few 10^5 iterations for a given set of parameters. Throughout these iterations, the system does not show any change in its morphology (whether percolating, non-percolating, sheets, rods, etc.).

The corresponding experimental realization of such a non-equilibrium Monte-Carlo scheme is discussed at the end.

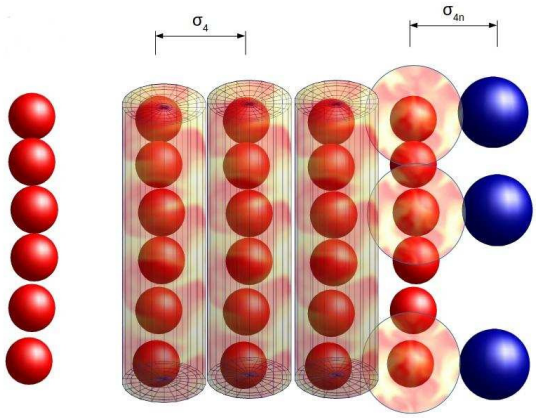

FIGURE 4.1: (colour online) The figure explains the calculation of the effective volume of monomers. Red coloured particles represent monomers, whereas the nanoparticles are shown in blue. Two neighbouring polymeric chains with distance between monomers centers $< \sigma_4 = 1.75\sigma$ are considered as the cylinders of radius σ_4. Monomers whose position is within the range $2^{1/6}\sigma_{4n}$ of repulsive potential V_{4n} are assumed as spheres of radius $(\sigma_{4n} - \sigma_n/2)$, where σ_n is the radius of nanoparticles.

4.3 Results

In this chapter, the self-assembly of the equilibrium polymeric chains + NP system is investigated as a function of the σ_{4n} (EVP) and ρ_m. Throughout the chapter, the diameter of NPs σ_n, the quantity σ_4 and the NP chemical potential are kept fixed at 1.5σ, 1.75σ and $-8k_BT$, respectively, unless otherwise mentioned. All the distances mentioned here refer to the centre-to-centre distances of the particles involved. To investigate the behaviour of NPs and wormlike micellar system, four different values of the number of monomers N_m are considered viz. $N_m = 2000, 4000, 5000$ and 6800 corresponding to the monomer number densities $\rho_m = 0.037\sigma^{-3}, 0.074\sigma^{-3}, 0.093\sigma^{-3}$ and $0.126\sigma^{-3}$, respectively.

4.3.1 Calculation of effective Volume

We realize that the system behaviour can be better characterized by considering the total excluded volume of cylindrical polymer chains and NPs due to the repulsive interactions V_4 and V_{4n} instead of only considering the volume fraction of spherical monomers. We define the total volume excluded by a chain due to the repulsive potentials from V_4 and V_{4n} as the effective volume of the chain. The effective volume of a monomer is the effective volume of the chains divided by the total number of monomers. The calculation of the effective volume of WLMs is explained in Fig.4.1. The figure shows that any two micellar chains (red spheres) at a distance of the cutoff distance ($2^{1/6}\sigma_4$) (range of the repulsive interaction (V_4)) from each other are considered as non-overlapping cylinders of diameter σ_4 (shaded cylinders). Correspondingly, the effective volume of the monomer in the chain is defined to be $v_1 = \pi(\sigma_4/2)^2\sigma$. If a monomer is at a distance less than the cutoff distance $2^{1/6}\sigma_{4n}$ (for V_{4n}) from a nanoparticle, then the monomer is considered to be a sphere of radius $(\sigma_{4n} - \sigma_n/2)$ (shaded sphere) and the effective volume of the monomer is

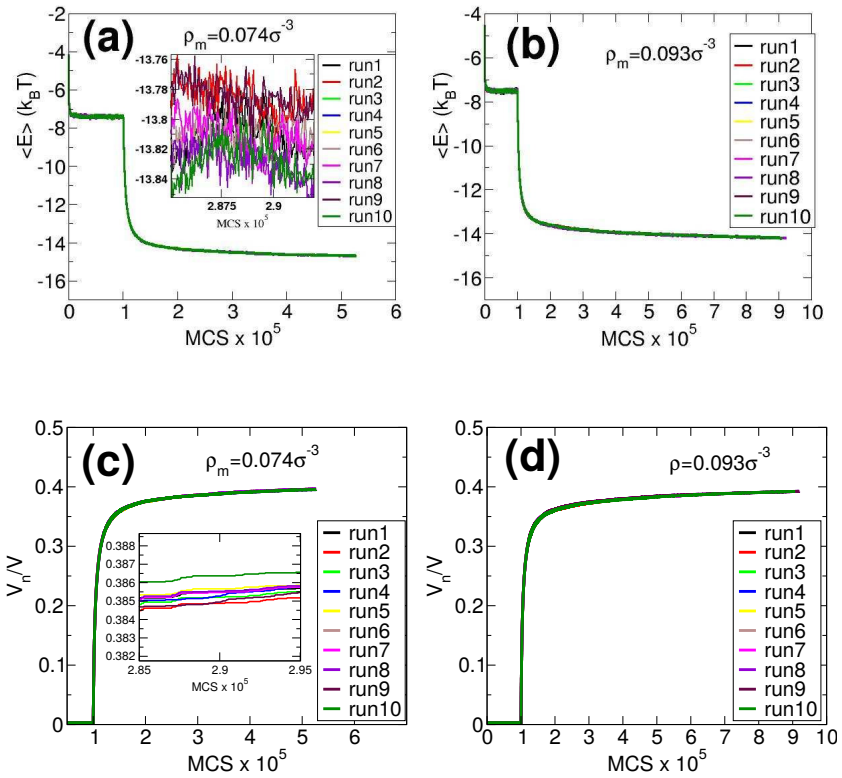

FIGURE 4.2: (colour online) The subplots (a),(b) shows the plots of average energy per particle (both monomers and NPs) for two different values of monomer number density ρ_m. The subplots (c),(d) shows nanoparticle volume fraction V_n/V versus MCSs, V_n is the volume of NPs and V is the volume of the simulation box. The parameter σ_{4n} is kept fixed at 1.25σ. Each figure shows multiple graphs generated from 10 independent runs initialized with different initial configurations which can be clearly seen in the magnified parts of the graphs shown in the inset of figures (a) and (c). The system is evolved with MC steps for a first 10^5 iterations and then subjected to the grand-canonical MC (GCMC) scheme on nanoparticles. The data show a sudden jump in their values when we switch on GCMC.

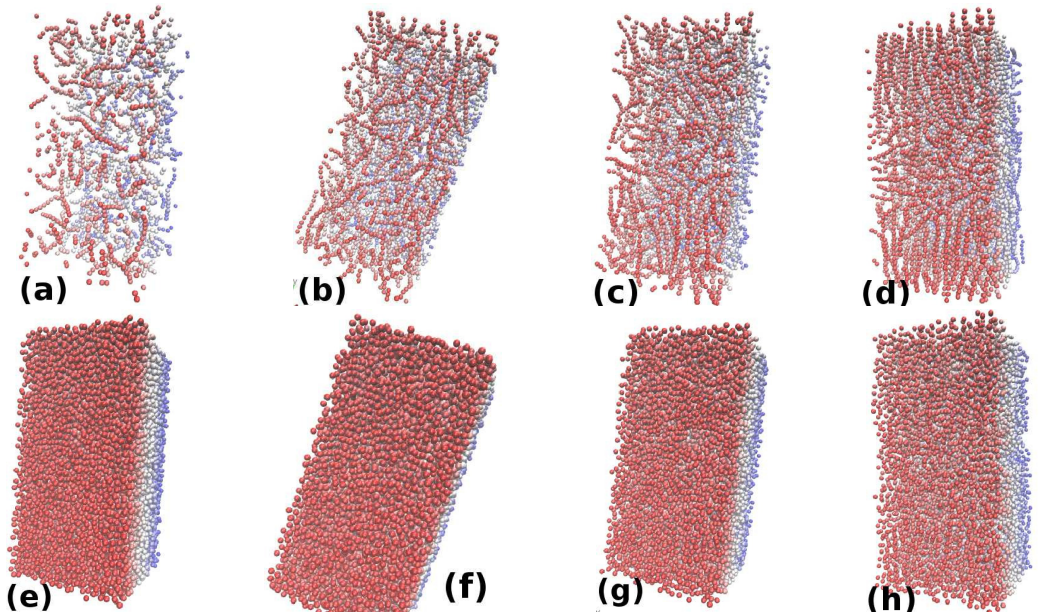

FIGURE 4.3: (colour online) The upper row of snapshots shows snapshots of only the equilibrium polymers (micellar chains) and the lower row shows only the nanoparticles of the NP+polymer system. Different snapshots are for different values of monomer densities; (a),(e) is for $\rho_m = 0.037\sigma^{-3}$, (b),(f) is for $\rho_m 0.074 = \sigma^{-3}$, (c),(g) is for $\rho_m = 0.093\sigma^{-3}$ and (d),(h) is for $\rho_m 0.126\sigma^{-3}$. The value of σ_n and σ_{4n} is kept fixed at 1.5σ and 1.25σ, respectively. All the snapshots show that the nanoparticle-monomer system is in a uniformly mixed state, and clustering of micellar chains is not observed. All the figures have a gradient in their colour varying from red to blue to identify and distinguish between the particles which are near the front plane (red) and the ones which are closer to the back of the box (blue).

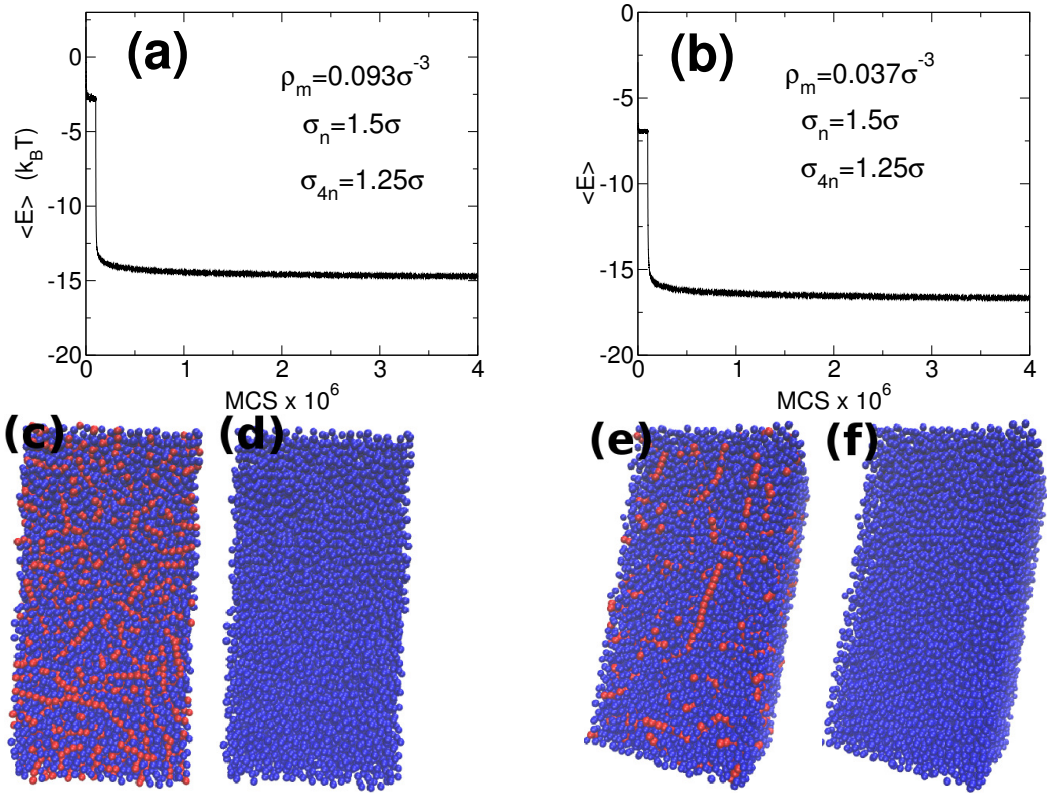

FIGURE 4.4: The figure shows the evolution of average energy per particle of the system with Monte Carlo steps for the value of $\sigma_n = 1.5\sigma$, $\sigma_{4n} = 1.25\sigma$ and $\rho_m =$ (a) $0.093\sigma^{-3}$ and (b) $0.037\sigma^{-3}$. As the system is very dense, these runs take a very long time spanning from weeks to months. However, after a very long time, the energy values show on an average a constant value. These graphs correspond to the snapshots shown in Figs. 4.4(a) and 4.4(c), respectively. The snapshots corresponding to the graphs in (a) and (b) are shown in subfigures (c), (d) and (e), (f), respectively. The red particles indicate monomers while the blue particles indicate nanoparticles in the snapshots. Subfigures (d) and (f) only show the nanoparticles in the snapshots of (c) and (e), respectively.

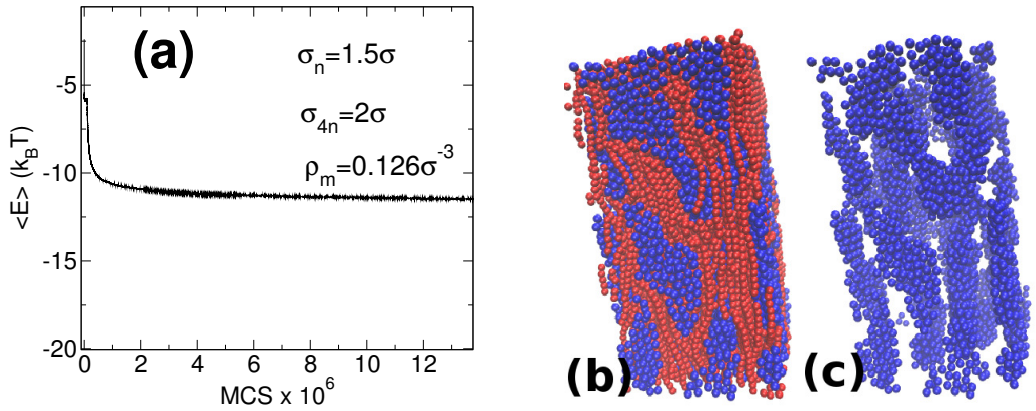

FIGURE 4.5: The subfigure (a) shows the evolution of the average energy graph versus Monte Carlo steps for $\sigma_n = 1.5\sigma$, $\sigma_{4n} = 2\sigma$ and $\rho_m = 0.126\sigma^{-3}$. It is a very long run showing a constant value of energy and confirming the stability of the system structure. The snapshots corresponding to the energy plot are shown in (b) and (c) where monomers and nanoparticles are indicated by red and blue particles, respectively. The subfigure (c) only shows the nanoparticles from the system of monomer+nanoparticles as shown in (b).

$v_2 = 4\pi/3(\sigma_{4n} - \sigma_n/2)^3$. Any monomer that is not involved in any of the repulsive interactions V_4 and V_{4n} has the volume $v_3 = 4\pi/3(\sigma/2)^3$.

To calculate this effective volume using a suitable algorithm, first, we identify and label the monomers which are part of a chain. All monomers within a distance of 1.5σ (cutoff distance for V_3) from each other are considered as bonded and thus form part of a chain. We do not observe branching in the chains. Then all the chains that are involved in the repulsive interactions from other chains or nanoparticles are identified and the effective volume of micelles is calculated according to the scheme discussed above and illustrated in Fig.4.1. If a monomer interacts with a monomer of a neighbouring chain as well as a NP simultaneously, then, the higher of the two values of effective volume (v_1 or v_2) is considered. The effective volume fraction of micelles, thus calculated, depicts the actual excluded volume fraction because of the repulsive potentials V_4 and V_{4n} in addition to the volume fraction of monomers ($\rho_m 4/3\pi(\sigma/2)^3$). If there are n_1 monomers interacting with other monomers with potential V_4, n_2 monomers having repulsive interaction V_{4n} with a nanoparticle and n_3 monomers out of range of the potentials V_4 and V_{4n} then, $n_1v_1 + n_2v_2 + n_3v_3$ depicts the effective volume of micelles. This effective volume of monomers is not only dependent upon the value of σ_4 and σ_{4n} but also on the arrangement of the constituent particles. The effective volume thus calculated will help in understanding the behaviour of the system. For monomers situated in between a micellar chain and NPs, the volume may get slightly overestimated when $\sigma_{4n} - \sigma_n > \sigma_4$. This is because of the over-calculation of the volume in case of overlapping of the shaded (red) spheres and shaded monomer chains (cylinders) as shown in the Fig.4.1. However, this overestimation does not change the interpretation of results.

4.3.2 Investigation for systems with $(\sigma_{4n})_{min} = 1.25\sigma$: Formation of a dispersed state of polymeric chains

In order to study the effect of change of micellar density, the system is simulated with different monomer number densities at $\sigma_{4n} = 1.25\sigma$ (minimum allowed value

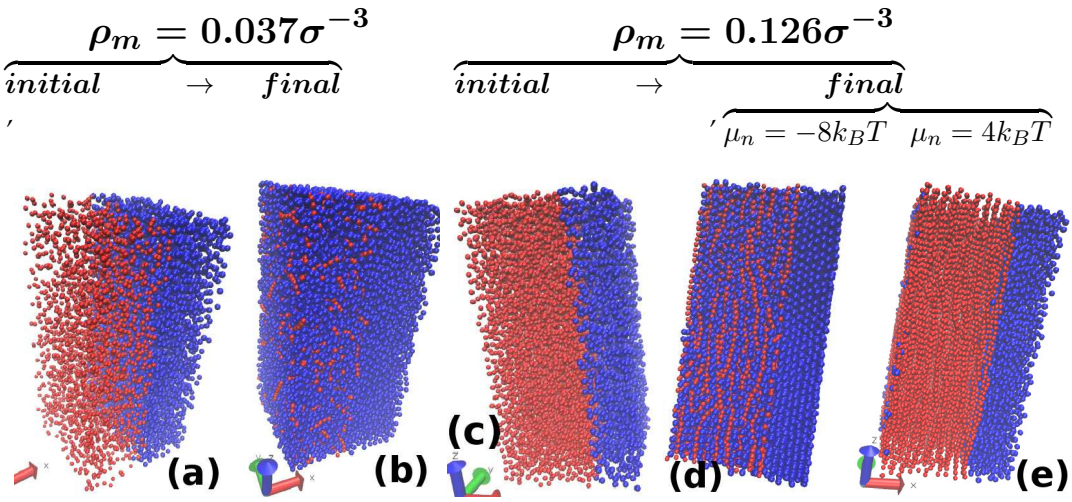

FIGURE 4.6: (colour online) The figure shows the snapshots of the system for monomer number densities $\rho_m = 0.037\sigma^{-3}$ (figures (a) and (b)) and $0.126\sigma^{-3}$ (figures (c), (d) and (e)). Red particles indicate monomers while nanoparticles are shown in blue. For each ρ_m, the two snapshots in (a) and (c) represent the initial configuration of monomers and NPs, where NPs and monomers are kept on two sections of the simulation box. The snapshots in (b) and (d) show the microstates after 4×10^6 iterations (with GCMC switched on after 10^5 iterations). In both the cases of densities, the final state deviates from the initial state forming uniformly mixed states of micellar chains + nanoparticles, this coexists with a state which occupies part of the box which has only densely packed nanoparticles (without micellar chains). The snapshot in figure (e) shows the final state of the system initialized as in (c) but with a higher value of chemical potential $\mu_n = 4k_BT$. The states reached after the runs for $\mu_n = -8k_BT$ (figure (d)) and $\mu_n = 4k_BT$ (figure (e)) are different. The state in (e) shows a phase-separated state.

of σ_{4n}; refer Fig.2.4). To check the robustness of the results, for each number density of monomers, the system is observed over ten independent runs each starting with different initial random configurations. First, the system is evolved by applying Monte Carlo technique for 10^5 iterations and then the GCMC scheme is switched on for the rest of the iterations. Fig.4.2 shows the evolution of the average energy of the constituent particles ($\langle E \rangle$) and the NP volume fraction V_n/V with MCSs, for two different values of monomer number densities. The NP volume V_n is given by $V_n = N_n 4\pi {\sigma_n}^3/3$ where, N_n is the number of NPs in the simulation box. Both the figures for energy per unit constituent particle (Fig.4.2(a) and (b)) and the volume fraction of NPs graphs (Fig.4.2(c) and (d)) show data for multiple runs generated from ten independent runs. All these graphs from different independent runs overlap and look indistinguishable from each other. Therefore, magnified parts of the graphs are shown in the insets of figures (a) and (c). The inset figures clearly show different graphs for different independent runs indicated by different colours, for a small range of iterations. All the graphs show a jump on switching to the GCMC scheme at 10^5 of MCSs, indicating an increase in the NP volume fraction in the system. The insets clearly show the energy fluctuations and a gradual increase in the number of NPs with MCS.

All the independent runs for each ρ_m produce similar configurations after (2

to 4)$\times 10^5$ iterations and the energy and NP volume fraction graphs converge to the same value. For each ρ_m, a very long run (4×10^6 iterations) was given to check if there is any change in the morphology of the system within thermal fluctuations. The system is found to maintain its morphology across all independent runs. After $\approx 2 \times 10^5$ iterations, the system morphology remains relatively unchanged for the length of the runs varying from 4×10^5 to 4×10^6 of iterations. Once the energy graphs show a very slow variation in its values and no further change in the polymer-NP morphology is observed, we show the representative snapshots for each of the monomer number densities ρ_m in Fig.4.3. The monomers and the NPs are shown separately in the upper row and the lower row, respectively. All the snapshots have a gradient in colour varying from red (front plane) to blue (rear plane) along one of the box lengths, for better visualisation of a three-dimensional figure. The figure shows the snapshots for (a) $\rho_m = 0.037\sigma^{-3}$, $(b)0.074\sigma^{-3}$, $(c)0.093\sigma^{-3}$ and (d) $0.126\sigma^{-3}$. No clustering of micellar chains is observed, i.e. any two neighbouring chains are always found with NPs in between. In other words, the NP-monomer system forms a uniformly mixed state.

An increase in the nematic ordering of polymeric chains and their chain length can be recognized from the figures as a result of the change in ρ_m in Fig.4.3. The snapshot in Fig.4.3(a) shows smaller chains in a disordered state and the chain length and order increases for Figs.4.3(b) and 4.3(c) and finally the system forms a nematic state with longer and aligned chains in Fig.4.3(d). All the systems shown in the figure may show different polymer arrangements, but for all the micellar densities a uniformly mixed state of polymeric chains and NPs is observed. These systems are also is checked with very long runs. The results for such long runs are shown in Fig.4.4 for (a) $\rho_m = 0.093\sigma^{-3}$ and (b) $\rho_m = 0.037\sigma^{-3}$. Similar result is shown for $\rho_m = 0.126\sigma^{-3}$ in Fig.4.5.

All the independent runs discussed till now had the systems initialized in a state where the positions of both the monomers and 200-300 seed nanoparticles are randomly chosen. To ensure that our conclusions are not dependent on initial conditions, we gave additional runs initialized with all monomers on one side and all the NPs on the other side of the box. The representative snapshots from these runs after 4×10^6 iterations, for $\rho_m = 0.037\sigma^{-3}$ [Fig.4.6(a) and (b)] and $\rho_m = 0.126\sigma^{-3}$ [Fig.4.6(c), (d) and (e)] are shown. Figure 4.6(a) [and (c)] shows the initial state with $\rho_m = 0.037\sigma^{-3}$ with $N_m = 2000$ [$\rho_m = 0.126\sigma^{-3}$ with $N_m = 6800$] and 5000 [5000] NPs in the box. Figures 4.6 (b) and (d) show the snapshots after 4×10^6 MCSs for systems initialized as shown in Figs. (a) and (c), respectively. The Fig.4.6(e) shows the snapshot initialized with the same configuration shown in (c) but having the value of $\mu_n = 4k_BT$. For both the densities of monomers considered for $\mu = -8k_BT$, the final state is different from the initial state forming a uniformly mixed state of monomer chains and NPs (left side of the box) coexisting with NPs without monomers (right side of the box) (figures (b) and (d)). The runs were tested with different initial numbers of NPs, but all the runs resulted in a mixed state of polymeric chains and NPs (as shown in the left part of the boxes in Figs.4.6(b) and 4.6(d)). These mixed states are found to be coexisting with NPs shown in the right sides of the boxes. We expect that if the system reaches equilibration, the systems will evolve to a completely mixed state as in Figs.4.3(e), (f), (g) and (h) for $\sigma_{4n} = 1.25\sigma$ and $\mu_n = -8k_BT$. But in our studies, the density of monomers and NPs are locally very high, which leads to very packed structures which are unable to relax to equilibrium. However, keeping the initial state similar to Fig.4.6(c) and increasing the value of μ_n from $\mu_n = -8k_BT$ to $\mu_n = 4k_BT$ for $\rho_m = 0.126\sigma^{-3}$ resulted in a phase-separated state as shown in Fig.4.6(e).

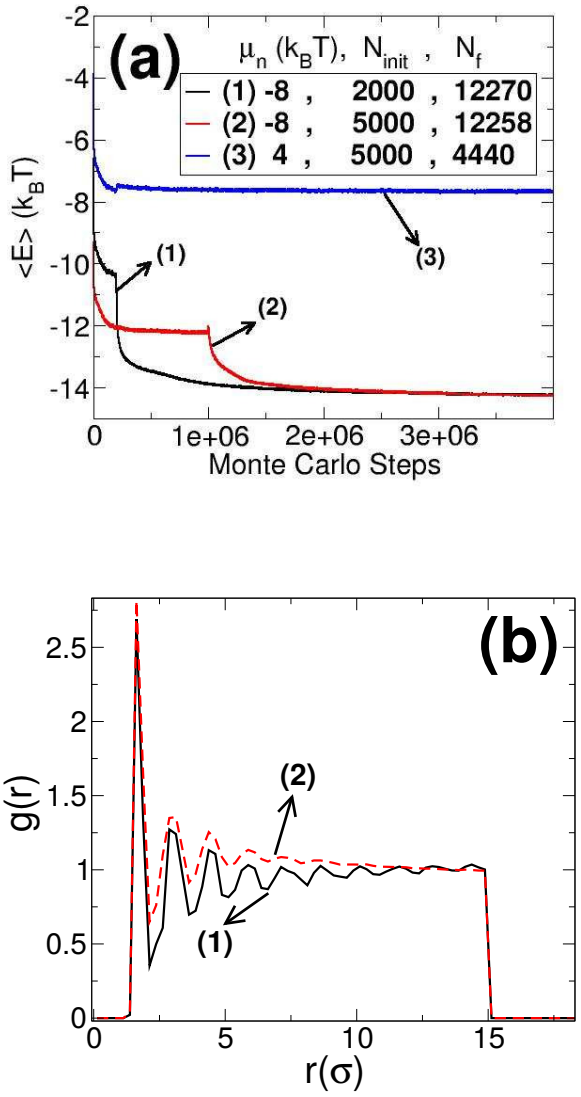

FIGURE 4.7: (colour online) (a) The figure compares the average potential energy $\langle E \rangle$ of the constituent particles (monomers and NPs) versus MCSs of the systems that are initialized as shown in Fig.4.6(c). Lines (1) and (2) correspond to data with $\mu_n = -8k_BT$ and line (3) corresponds to data with $\mu_n = 4k_BT$. The graphs (2) and (3) correspond to the systems represented in Figs.4.6(d) and (e), respectively, at the end of the run. The graphs (1) and (2) differs in their number of nanoparticles in the initial configuration N_{init} as well as in the value of iterations/MCS after which the GCMC scheme is switched on. The two graphs (1) and (2) illustrates that the results are independent of the value of N_{init} and the number of iterations after which the GCMC scheme is switched on, as for both cases $\langle E \rangle$ converges to the same value within statistical fluctuations. On switching on to GCMC scheme, graphs (1) and (2) jumps to a lower value of $\langle E \rangle$. This is indicative of the rapid addition of nanoparticles in the system. The line (3) jumps to a slightly higher value of energy indicating the removal of nanoparticles. The legends N_f indicates their final value of the number of nanoparticles after 4×10^6 MCS. (b) The figure shows the pair correlation function $g(r)$ for the NPs in left two-thirds of the box represented by line-2 and the NPs in the right one-third of the box (line-1) corresponding to the configuration shown in the Fig.5(d). The pair correlation function shows the presence of a long-range correlations in the position of NPs corresponding to a crystalline ordered state in the right section of the box.

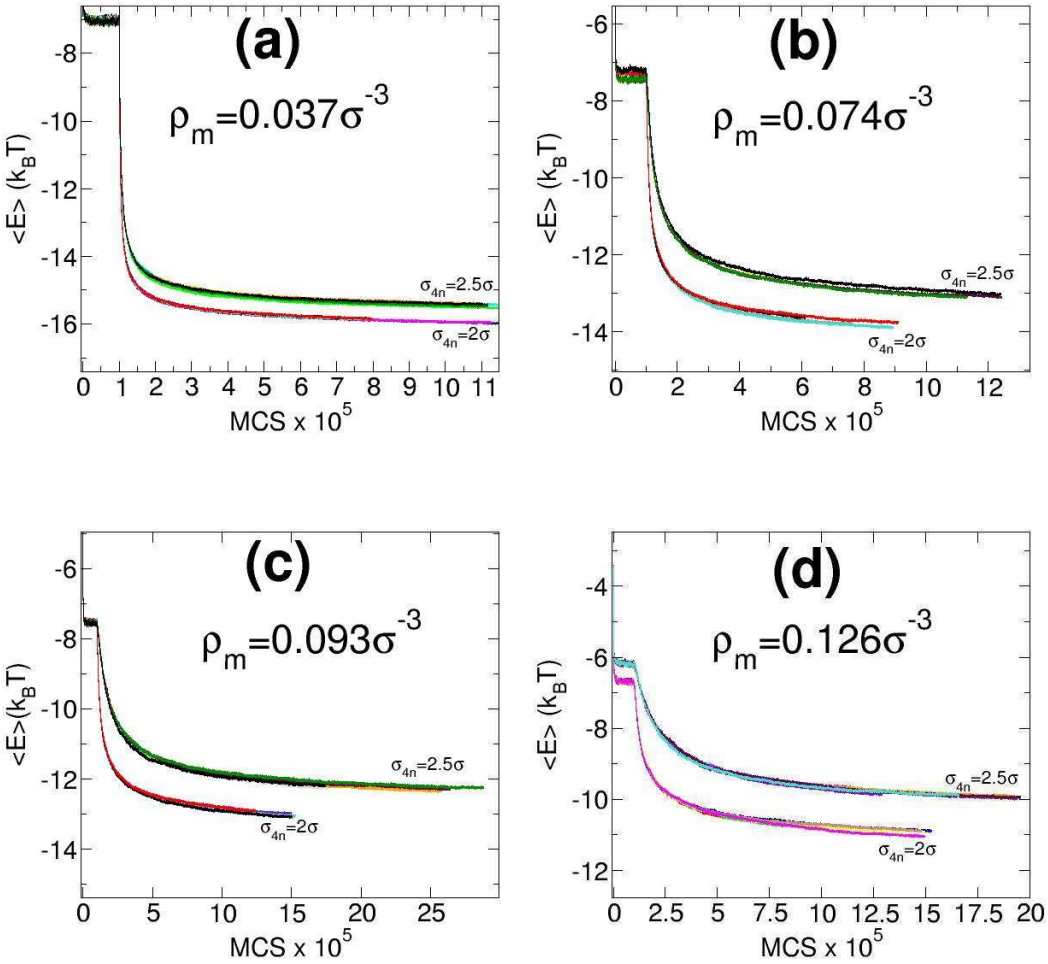

FIGURE 4.8: (colour online) Plots of average potential energy $\langle E \rangle$ per particle (monomer and NP) of the system for different values of monomer number densities (a) $\rho_m = 0.037\sigma^{-3}, (b)0.074\sigma^{-3}, (c)0.093\sigma^{-3}$ and (d) $0.126\sigma^{-3}$. Each figure shows the energy graphs for two different values of $\sigma_{4n} = 2\sigma$ and 2.5σ. For each value of σ_{4n}, there are ten graphs overlapping each other and converging to the same values. The Monte Carlo scheme (without GCMC) is applied for first 10^5 iterations. Then the GCMC scheme is switched on which leads to a further decrease in the energy values indicated by jumps in the values of $\langle E \rangle$ in each graph.

Thus, it is observed that for $\mu_n = -8k_BT$, the system initialized as shown in Fig.4.6(c) always leads to form a mixed state while, for $\mu_n = 4k_BT$, the system remains in a phase-separated state. This difference in the behaviour of the systems with different values of μ_n can be confirmed by the plots shown in Fig.4.7(a). The figure shows three graphs (1), (2) and (3). For all the graphs, the state of initialization is as shown in Fig.4.6(c) but with a different initial number of nanoparticles N_{init} as indicated in the figure. Graphs (1) and (2) shows the evolution of energy with MCSs for $\mu_n = -8k_BT$ initialized with 2000 and 5000 NPs, respectively. Both the graphs show convergence to the same value of energy after 4×10^6 iterations with a jump to lower energy values on switching on the GCMC scheme at 10^5 and 10^6 iterations, respectively. This jump to lower energy indicates the addition of NPs into the box on switching *on* the GCMC scheme. Irrespective of (i) the number of MCSs at which the GCMC scheme is switched *on* and (ii) the initial number of NPs N_{init}, all the systems are observed to evolve to form a mixed state and converges to the same value of energy for $\mu_n = -8k_BT$ (two of which constitutes the graphs (1) and (2)). Graph (3) shows the evolution of energy for the system initialized with the same state as in Fig.4.6(c) with 5000 NPs in the box, but having a higher value of $\mu_n = 4k_BT$. On switching *on* the GCMC scheme, the graph shows a jump at 10^5 MCSs to a higher value of energy indicating the removal of NPs from the box. The system evolves to form an equilibrated phase separated state as shown in 4.6(e) after removal of ≈ 550 NPs from the box. Since all the systems initialized with the configuration shown in 4.6(c) and $\mu_n = -8k_BT$ evolves to form a mixed state irrespective of the initial number of NPs in the system, it can be concluded that for $\mu_n = -8k_BT$, a phase-separated state is not a thermodynamically preferred state. Therefore, we can now claim from the snapshots shown in Fig.4.3 that the mixed state will remain the thermodynamically preferred state as well, for $\sigma_{4n} = 1.25\sigma$. We remind the reader that we do not claim that the microstates corresponding to the snapshots of Fig.4.3 are in equilibrium that the values of both the average energy as well as V_n/V are evolving.

For the value of $\mu_n = -8k_BT$, one more difference can be observed for different values of ρ_m which can be seen in Figs.4.6(b) and 4.6(d). Both the figures are initialized with similar configurations (unmixed state) and number of NPs $N_{init} = 5000$, but with different values of monomer number density $\rho_m = 0.037\sigma^{-3}$ [Fig.4.6(a)] and $\rho_m = 0.126\sigma^{-3}$ [Fig.4.6(c)]. In case of higher density of monomers, the phase of NPs which is devoid of monomers (in the right part of the box in Fig.4.6(d)) seems to have a long-range crystalline order compared to the lower density case [refer the right part of the box in Fig.4.6(b)]. The figure 4.7(b) compares the pair correlation function for the NPs in left section box in Fig.4.6(d) as well as the right section where the NPs dont have monomers interspersed between them. The correlation graphs for NPs in the mixed state (in the left part of the box in Fig.4.6(d)) depicted in graph (2) shows very few and low peaks which die out quickly compared to the graph for NPs (in the right part of the box of Fig.4.6(d)) as depicted by graph (1). The graph (1) has very sharp peaks and shows a longer range of correlation hence, confirming the observed ordered structure of NPs. We expect that these two coexisting states, as shown in Fig.4.6(b) and (d) are stuck in a metastable state, and they will form a fully mixed state after equilibration.

All the results for ten independent runs and the runs shown in Fig.4.6 indicate that the mixed state of NP and micellar chains could be the thermodynamically preferred state of the system for the value of $\mu_n = -8k_BT$. The systems considered here are quite dense and show a very slow increase in the number of nanoparticles even after a very long run (Fig.4.8(c,d)). Therefore, we assume that the structures discussed in the previous sections (see Fig.4.3) are most probably kinetically arrested

states that are relaxing slowly to equilibrium. The rest of the chapter considers the systems initialized with a randomly mixed state of micelles and NPs and investigates the effect of the change in σ_{4n} for each value of ρ_m.

4.3.3 $\sigma_{4n} > 1.25\sigma$: Polymer and NP clusters with different morphologies

We next investigate the effect of the change in the value of σ_{4n} for different monomer densities by varying ρ_m and σ_{4n}. The results from these runs were further substantiated with ten independent runs for each value of ρ_m and σ_{4n}. The average energy of the system for ten independent runs for two different values of $\sigma_{4n} = 2.5\sigma$ and 2σ is shown in Fig.4.8 for values of densities (a) $0.037\sigma^{-3}, (b)0.074\sigma^{-3}, (c)0.0931\sigma^{-3}$ and $(d)0.126\sigma^{-3}$. The system is evolved with Monte Carlo steps without GCMC for the first 10^5 iterations and then the GCMC scheme is switched on which is marked by a rapid lowering in the energy values in Fig.4.8. This lowering of energy values corresponds to the rapid addition of nanoparticles in the system but, the rate of addition slows down after $(2-5) \times 10^5$ iterations. In each figure, each visible line shows multiple lines overlapping each other, generated by ten independent runs. All the ten independent runs converge to the same value of energy. Here, we would like to emphasise again that all the systems are initialized with random positions of monomers and 200-300 seed nanoparticles and with the grand-canonical Monte Carlo steps NPs get introduced in the midst of the micellar chains. This method of initialization is reminiscent of the in situ method of preparation of nanoparticles inside the matrix of polymers, where the NPs start nucleating out from a chemical solution on a suitable addition of a reactant.

After evolving the system for $(2-4) \times 10^6$ iterations, the representative snapshots for four different values of $\rho_m = 0.037\sigma^{-3}$, $0.074\sigma^{-3}$, $0.093\sigma^{-3}$ and $0.126\sigma^{-3}$ are shown in figures 4.9, 4.10, 4.11 and 4.12, respectively. For each NP+micelles system, the monomers and NPs are shown separately in the upper and lower rows, respectively, in figures 4.9, 4.10, 4.11 and 4.12. Each figure shows the snapshots for four different values of σ_{4n} increasing from (a) to (d) for monomers (in red) (or (e) to (h) for NPs in blue). Only for snapshots of NPs in Figs.4.9, 4.10(a) and 4.10(e), there exists a gradient in colour (varying from red to blue along one of the lengths of the simulation box) from front plane to the rear plane. This helps to identify particles lying in different planes and thereby clearly see the pores in NP aggregates. These pores are occupied by monomers.

In each of the figures, one can see in the leftmost snapshot (snapshots (a) and (e), which are for a lower value of σ_{4n}) a network-like structure of micellar chains or NPs which spans the system. An increase in the value of σ_{4n} leads to a decrease in number of nanoparticles that gradually breaks the network connections, thus, gradually breaking the network of NPs as shown in Figs.4.10(g), 4.11(f,g) and 4.12(f). With further increase in σ_{4n}, these networks break into non-percolating clusters as shown for $\sigma_{4n} = 3.25\sigma, 3\sigma$ and 2.25σ in figures 4.10(h), 4.11(h) and 4.12(g), respectively. We do not observe the breaking of networks into individual NP clusters for $\rho_m = 0.037\sigma^{-3}$ in Fig.4.9 for the range of values of σ_{4n} considered here. Therefore with an increase in ρ_m, the value of σ_{4n} at which the network breaks into non-percolating clusters gets shifted to a lower value of σ_{4n}. From the snapshots 4.10(h), 4.11(h) and 4.12(g), it can be clearly seen that different densities of micelles lead to different shape-anisotropy of nanoparticle clusters. It forms sheet-like structures for $\rho_m = 0.074\sigma^{-3}$ [Fig.8(h)] and $0.0931\sigma^{-3}$ [Fig.9(h)] while rods are formed for higher density of monomers [Fig.10(h)]. We give the reasons of how the sheet-like structures are formed at the end of the chapter.

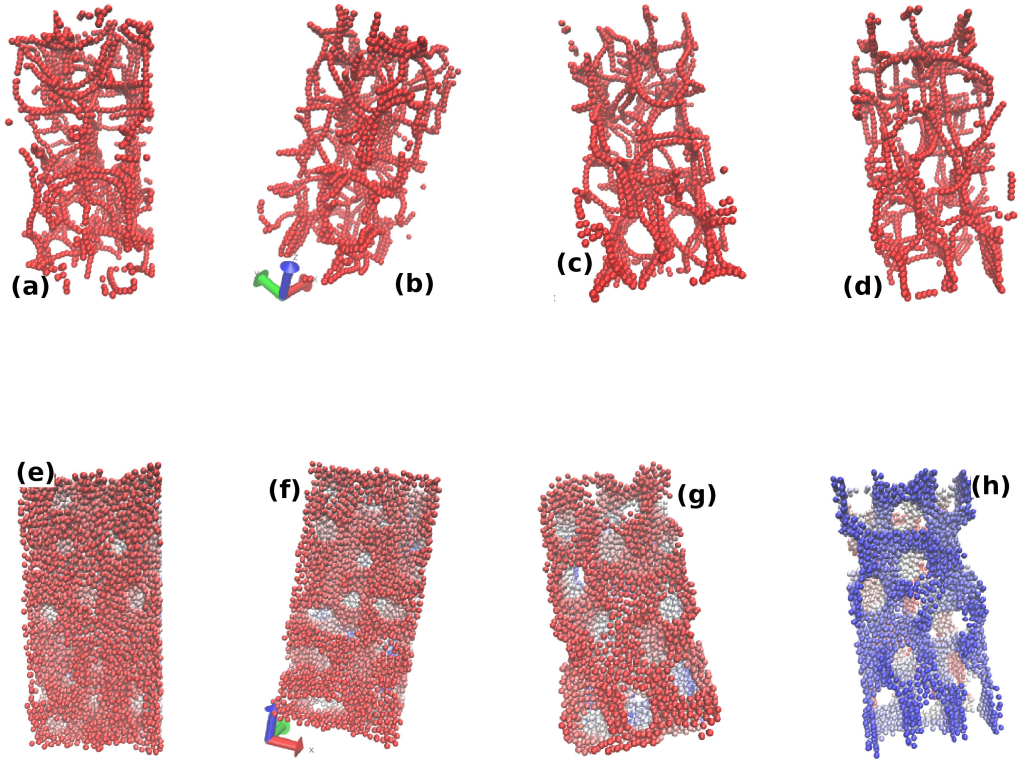

FIGURE 4.9: (colour online) The figure shows the snapshots for NPs and monomers from the NP + micellar-polymer system for the lowest value of monomer number density$\rho_m = 0.037\sigma^{-3}$. The snapshots in the upper row show only the micellar monomers while only the nanoparticles are shown in the lower row. The snapshots from (a) to (d) [and correspondingly (e) to (h)] are for $\sigma_{4n} = 2.0\sigma, 2.5\sigma, 3\sigma$ and 3.5σ, respectively. There is a gradient in colour along one of the shorter axes of the box for the snapshots (e) to (h), to help reader differentiate the particles present near the front plane from those at the rear. All the snapshots indicate the formation of the network-like structure of aggregates of nanoparticles and micellar chains interpenetrating each other.

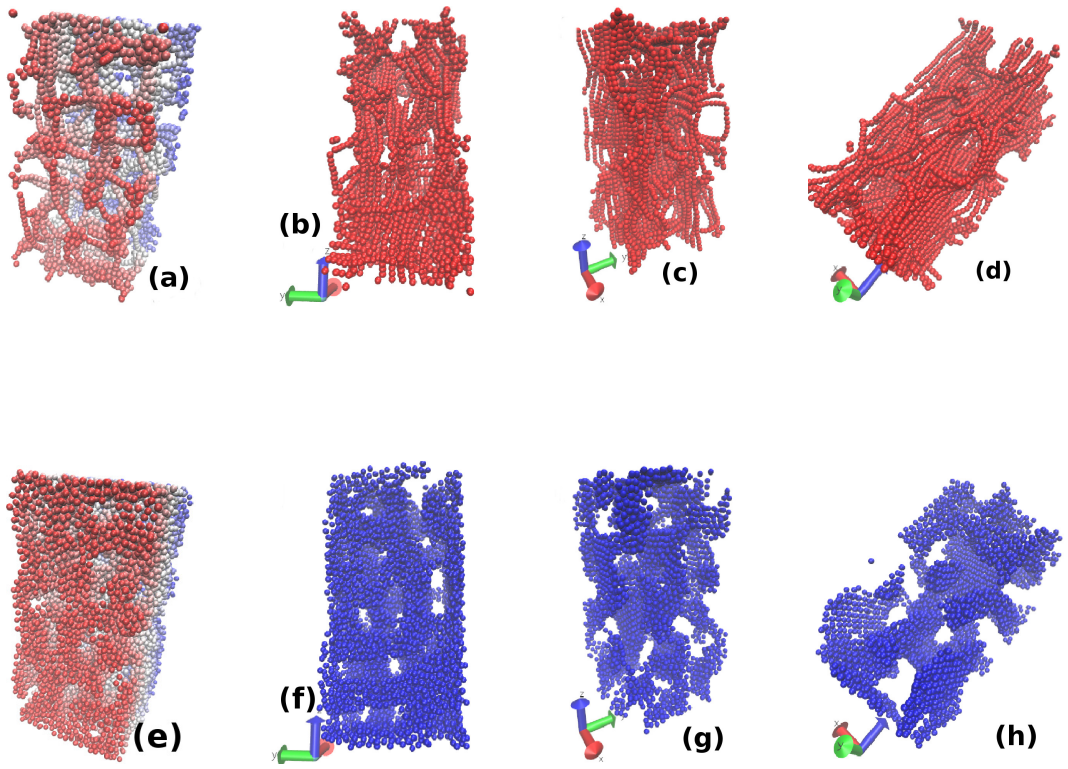

FIGURE 4.10: (Colour online) The figure shows the snapshots of NPs and monomers from the NP + micellar-polymer system for the value of monomer number density $\rho_m = 0.074\sigma^{-3}$. The snapshots in the upper row show only the micellar monomers while the lower row only shows the nanoparticles. Snapshots from (a) to (d) [or correspondingly (e) to (h)] are for $\sigma_{4n} = 1.75\sigma, 2.25\sigma, 2.75\sigma$ and 3.25σ, respectively. The snapshots (a) and (e) have a gradient in colour varying from red to blue along one of the shorter axis of the simulation box to help the reader differentiate the particles at the front plane and those closer to the rear. Snapshots (e), (f), and (g) are forming network-like structures of nanoparticles, while the nanoparticle network breaks down into non-percolating clusters in the figure (h) by forming individual sheetlike nano-structures.

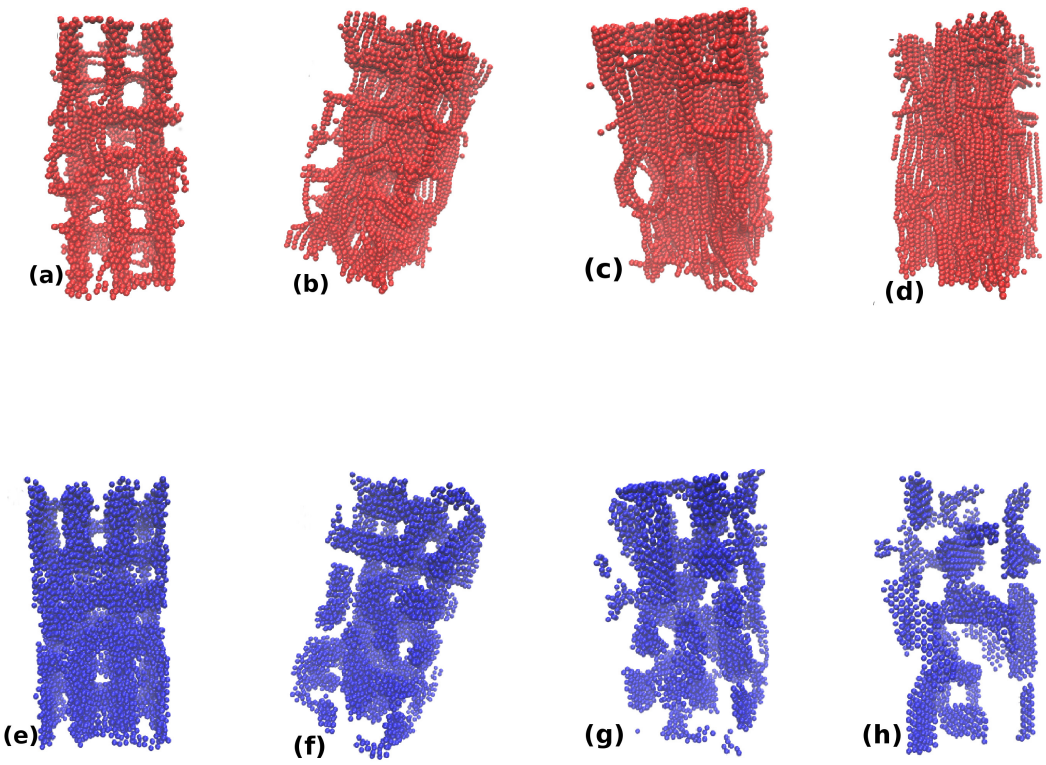

FIGURE 4.11: (colour online). The figure shows the snapshots of NPs and monomers from the NP + micellar-polymer system for the value of number density of monomers $\rho_m = 0.093\sigma^{-3}$. Snapshots in the upper row show only micellar monomers (red) while the snapshots in the lower row only show nanoparticles (blue). Snapshots from (a) to (d) [or correspondingly (e) to (h)] are for $\sigma_{4n} = 1.75\sigma, 2.25\sigma, 2.5\sigma$ and 3σ, respectively. With the increase in the value of σ_{4n} from left to right, the snapshots of nanoparticles show that the network gradually breaks and form individual sheet-like clusters for a high value of σ_{4n}, as shown in the snapshot (h).

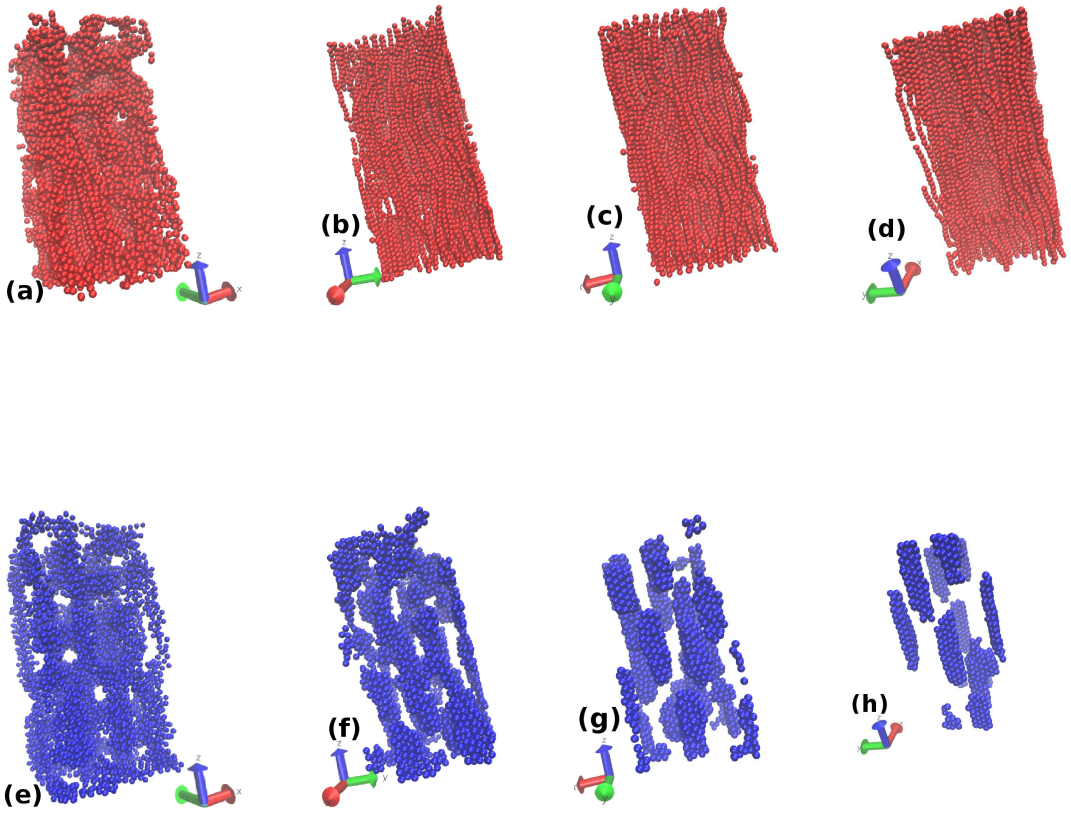

FIGURE 4.12: (colour online). Figure shows the snapshots of NPs and monomers from the NP + micellar-polymer system for monomer number density $\rho_m = 0.126\sigma^{-3}$. The snapshots in the upper row show only micellar monomers while, only the NPs are shown in the lower row. Snapshots (a) to (d) (or (e) to (h)) correspond to $\sigma_{4n} = 1.75\sigma$, 2σ, 2.25σ and 2.5σ, respectively. With the increase in the value of σ_{4n}, the figure shows the nanoparticle networks in (e) and (f) breaking into individual rod-like nanostructures as shown in the snapshots (g) and (h).

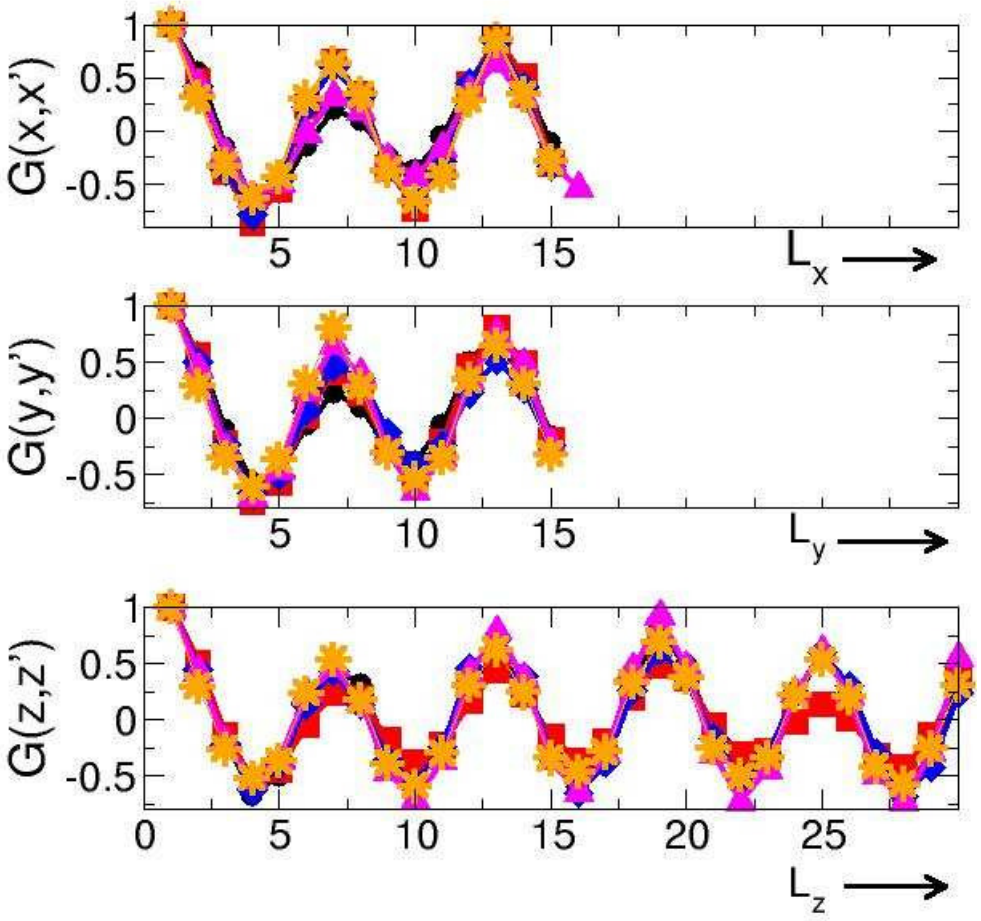

FIGURE 4.13: (colour online) The figure shows the average of the local density-density correlation function for monomers for $\sigma_{4n} = 1.5\sigma$ and different values of micellar densities indicated by different symbols. The density correlations along x, y and z-axis are shown separately from top to bottom. The different symbols are for $\rho_m = 0.037\sigma^{-3}$ (circle-black), $0.074\sigma^{-3}$ (square-red), $0.093\sigma^{-3}$(diamond-blue), and $0.126\sigma^{-3}$ (triangle-magenta). The symbols (star-orange) indicate the correlation plots for $\rho_m = 0.037\sigma^{-3}$ but $\sigma_{4n} = 3\sigma$.

It is observed that not only the non-percolating clusters of NPs have different shapes but also the clusters which constitute the NP-networks differ in their morphologies. The snapshots in figures 4.9, 4.10(e) (& 4.11(e)) and 4.12(e) show networks of NP aggregates, network of sheet-like clusters of NPs and network of rod-like clusters of NPs, respectively. Thus the density of micelles governs the morphology of NP structures with the anisotropy of NP clusters increasing with increase in micellar density viz. clusters to sheets to rods. We also observe that as soon as the value of σ_{4n} changes from 1.25σ (Fig.4.3) to 1.5σ (Fig.4.9(e), 4.10(e), 4.11(e), 4.12(e)), the micellar chains aggregate to form clusters which joins to form a system spanning network such that the networks of micellar chains and NPs are inter-penetrating each other. These networks at $\sigma_{4n} = 1.5\sigma$ seem to have the same periodicity in their structure irrespective of the micellar density.

4.3.4 Polymeric chains of the matrix: quantitative analysis of micro-structure

To confirm the above observations, we plot the density correlation function for monomers which is shown in Fig.4.13. It shows the density correlation function for monomers along the x, y, and z-axes of the box for $\sigma_{4n} = 1.5\sigma$. The function is calculated using the expression,

$$G(x_i, x_i') = \frac{\left\langle (\rho(x_i) - \langle \rho(x_i') \rangle)(\rho(x_i) - \langle \rho(x_i') \rangle) \right\rangle}{\left\langle (\rho(x_i) - \langle \rho(x_i) \rangle)^2 \right\rangle}, \tag{4.1}$$

where, $\rho(x_i)$ is the density of the monomers in a cubic box of size σ^3 at x_i. The term $\langle \rho(x_i) \rangle$ is the mean density of monomers in the simulation box. The term in the denominator normalizes the function from 1 to -1. The different symbols indicate the different values of micellar densities in Fig.4.13. All the plots for different densities overlap each other and are indistinguishable from each other. They have the same spatial period for all the densities and along the different axes. This indicates the periodic nature of the network-like structures in all three directions, and this remains unaltered by the change in monomer number density. This is observed not only for the value of $\sigma_{4n} = 1.5\sigma$ but also for all the values of σ_{4n} considered for $\rho_m = 0.037\sigma^{-3}$ (refer Fig.4.9).

For the lowest density of micelles considered here, i.e. $\rho_m = 0.037\sigma^{-3}$, the morphological change from networks of NPs to sheets to rod-like structures is not observed for $\sigma_{4n} > 1.25\sigma$. The effect of an increase in the value of σ_{4n} is observed to decrease the number density of NPs without changing the periodicity of the networks. The plot of density correlation function for all the values of σ_{4n} considered for $\rho_m = 0.037\sigma^{-3}$, has the same periodicity as shown by the plots in figure. 4.13. To confirm this, the plots shown in figure 4.13 shows graphs for $\rho_m = 0.037\sigma^{-3}$ for two different values of $\sigma_{4n} = 1.5\sigma$ (circle-black symbols) and 3σ (star-orange symbols).

Furthermore, the snapshots in figure 4.9 show that as σ_{4n} increases (from left to right), the pore size increases and the wall thickness (or the branch thickness of the network) is seen to be decreasing. Hence, we conclude that the thickness of the walls of the NP networks decreases as a result of an increase in σ_{4n}. This behaviour affects the porosity of the network. We define porosity as the volume fraction of the void inside the NP network. The porosity is calculated by subtracting the NP volume fraction from 1. The figure 4.14 shows the variation of porosity versus σ_{4n} quantifying the observed behaviour of the porosity with the increase in σ_{4n}. For a

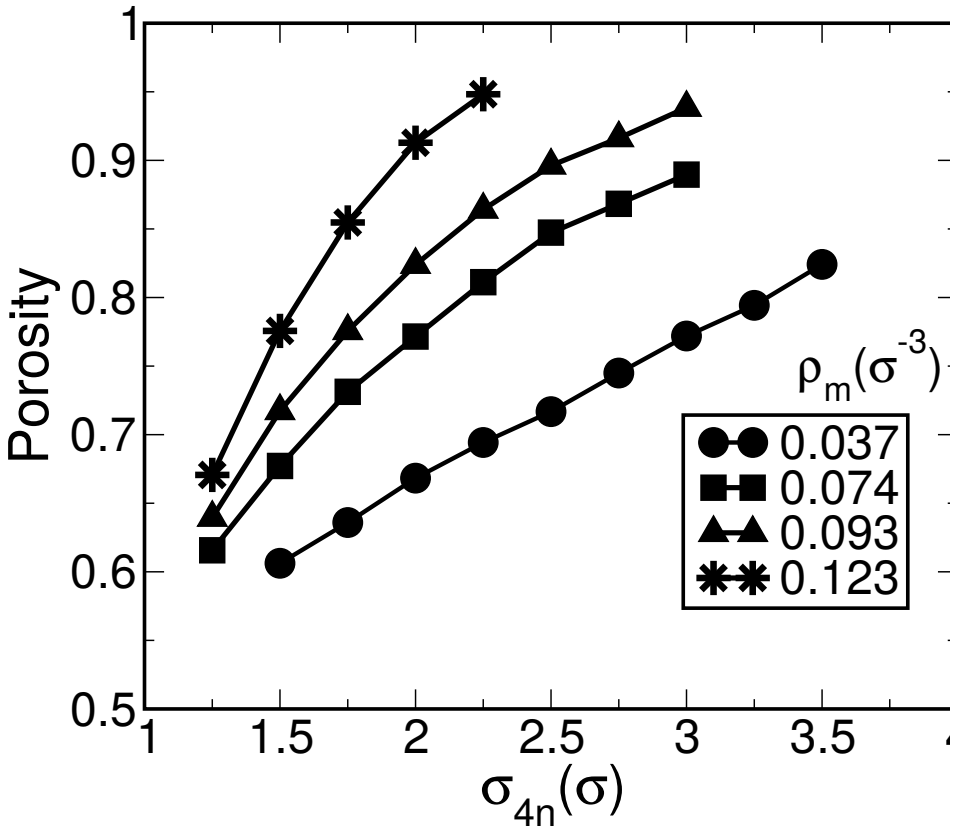

FIGURE 4.14: (colour online) The figure shows the variation in the porosity of the network of nanoparticles. Porosity is calculated by subtracting the nanoparticle volume fraction from 1, i.e. it represents the variation in the volume fraction of the void (currently occupied by monomers, but which can be dissolved away) inside a porous network of NPs due to the change in σ_{4n} values. The different symbols indicate the different values of micellar densities. It can be seen that the porosity of the networks increases with either increase in the value of σ_{4n} or increase in monomer number density ρ_m, as expected.

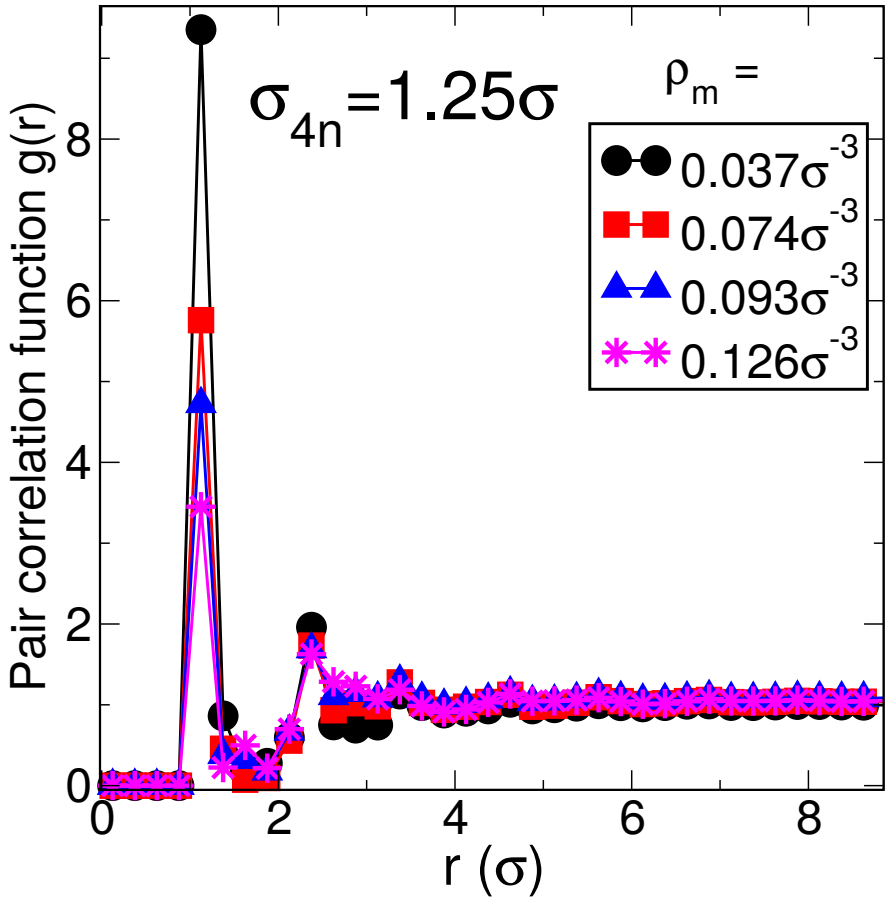

FIGURE 4.15: The figure shows the pair correlation function $g(r)$ for monomers at $\sigma_{4n} = 1.25\sigma$. It shows four different plots for $\rho_m = 0.037\sigma^{-3}, 0.074\sigma^{-3}, 0.093\sigma^{-3}$ and $0.126\sigma^{-3}$ which are indicated by different symbols in the figure. The absence of a peak around 1.75σ indicates that polymeric chains are out of the range of repulsive interaction V_4 from each other and hence depicts the dispersed state of chains, with NPs in between adjacent chains.

given value of σ_{4n}, an increase in micellar density decreases the available volume for NPs, thereby, increasing the porosity of the NP network. Therefore, the figure 4.14 also shows an increase in porosity with the increase in micellar density ρ_m for a fixed value of σ_{4n}, as expected. The non-linear behaviour of the plot for $\rho_m = 0.123\sigma^{-3}$ is related to the drop in the number of NPs which can get introduced into the box as one increases σ_{4n}. The nanoparticle porous structure can be obtained and used after removing by dissolving away the polymeric matrix.

In figures 4.9, 4.10, 4.11 and 4.12, we observe the clustering of NPs and micellar chains into different morphologies for values of $\sigma_{4n} \geq 1.5\sigma$ whereas, Fig.4.3 shows that for $\sigma_{4n} = 1.25\sigma$ (the minimum possible value of σ_{4n}), we obtain a uniformly mixed state of self-assembled micellar chains and NPs. To get an insight into the spatial arrangement of micellar chains, we calculate the pair correlation function g(r) of monomers corresponding to the snapshots shown in figures 4.3, 4.9, 4.10, 4.11 and 4.12. The plots in Fig. 4.15 corresponds to correlation function for the snapshots shown in Fig.4.3 while the plots in figures 4.16(a), 4.16(b), 4.16(c) and 4.16(d) correspond to the snapshots shown in figures 4.9, 4.10, 4.11 and 4.12, respectively. Different symbols represents $g(r)$ for different values of σ_{4n}.

In the correlation function of monomers, a first peak is expected to occur around the value of the diameter σ of the monomer (which is set as 1) followed by peaks at its multiples indicating the distance between bonded monomers along a chain. If there are chains that are situated at a distance $r <= 1.75\sigma$ (i.e. having the repulsive interaction V_4) from other chains, then peaks around 1.75σ and its multiples are expected. We do not observe any peak around 1.75σ in Fig.4.15 for all the values of micellar densities. This indicates that the micellar chains in all the snapshots shown in Fig.4.3 (for $\sigma_{4n} = 1.25\sigma$), are situated at a distance $r > 1.75\sigma$. This is consistent with the observation that no two micellar chains in Fig.4.3 are found to exist without NPs in between. With a NP of size 1.5σ between two monomer chains, the monomer chains have no possibility to remain within the range of repulsive potential ($r \leq 1.75\sigma$). Thus, it confirms the observation that, for all the snapshots shown in Fig.4.3, no clustering of micellar chains is observed, and a uniformly mixed state of micellar chains and NPs is formed.

In contrast to the plots in Fig.4.15, there appears a peak around 1.75σ in Figs.4.16(a), 4.16(b), 4.16(c) and 4.16(d). Except for the plots in Fig.4.16(a), it is observed that the height of this peak decreases with the increase in the value of σ_{4n} and finally vanishes for a higher value of σ_{4n}. The appearance of a peak around 1.75σ is consistent with the observed clustering of micellar chains as shown in the snapshots in Figs.4.9, 4.10, 4.11 and 4.12 where, they form network-like structures. As the value of σ_{4n} increases, the NP network gradually starts breaking and hence giving more space for micellar chains to be relatively further away from each other. This explains the decrease in the peak height around 1.75σ with an increase in σ_{4n}. When the NP network breaks to the extent that most of the micellar chains get enough volume to be at a distance $r > 1.75\sigma$, this peak disappears and a minimum is observed at that point. The value of σ_{4n} at which this happens can be seen to be decreasing with increase in micellar density viz. 3σ and 2.25σ for $\rho_m = 0.093\sigma^{-3}$ and $0.126\sigma^{-3}$, respectively.

However, this behaviour is not observed for $\rho_m = 0.037\sigma^{-3}$ [refer Fig.4.16(a)] where for all the values of σ_{4n} the peaks are present around 1.75σ. This is because, with an increase in σ_{4n}, the network-like structure is not observed to be breaking as shown in Fig.4.9. Therefore, for all the values of σ_{4n}, the polymeric chains show the formation of clusters of chains that is reflected in the form of peaks around 1.75σ for all the values of σ_{4n} in Fig.4.16(a).

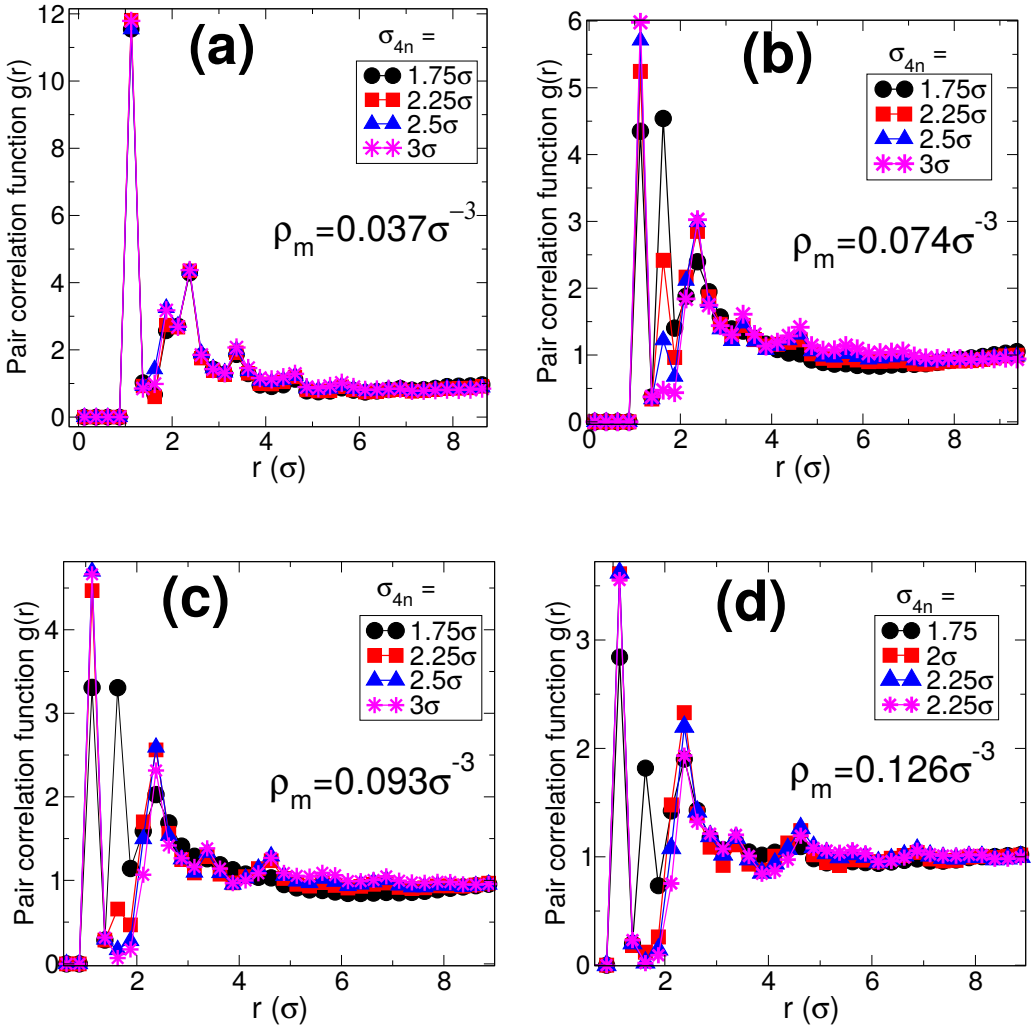

FIGURE 4.16: (colour online). The figure shows the pair correlation function for micellar monomers for $\sigma_{4n} = 1.25\sigma$ and micellar densities (a) $\rho_m = 0.037\sigma^{-3}$, (b) $\rho_m = 0.074\sigma^{-3}$, (c) $0.093\sigma^{-3}$ and (d) $0.126\sigma^{-3}$. Each figure shows the correlation function for four different values of $\sigma_{4n} > 1.25\sigma$ as indicated in the graph. Contrary to the observations from $g(r)$ data shown in Fig.4.15 (for $\sigma_{4n} = 1.25\sigma$), all the figures here show the appearance of peaks around 1.75σ. The appearance of a peak around 1.75σ indicates that the distance between adjacent monomer chains $\approx 1.75\sigma$ (the range of V_4). Therefore, chains are forming clusters that joins to form a network-like structure as shown in Fig.4.9, 4.10, 4.11, 4.12 for $\sigma_{4n} > 1.25\sigma$. With the increase in the value of σ_{4n}, the height of the peak around 1.75σ decreases and finally vanishes for a higher value of σ_{4n}, except for the lowest density shown in (a) for $\rho_m = 0.037\sigma^{-3}$. For the lowest density, the micellar chains forms networks of clusters of micellar chains for all the values of $\sigma_{4n} > 1.25\sigma$ as shown in Fig.4.9.

For the lowest micellar density considered $\rho_m = 0.037\sigma^{-3}$, only the network-like structures are observed for the range of values of σ_{4n} considered here (except for the case of $\sigma_4 = 1.25\sigma$). To ensure that the network architecture observed in the snapshots in Fig.4.9 is not an artefact of the small box size, these structures were reproduced in a larger box size of $60 \times 60 \times 60\sigma^3$ for all values of σ_{4n} considered for $\rho_m = 0.037\sigma^{-3}$. A representative snapshot for $\sigma_{4n} = 2.5\sigma$ and $\rho_m = 0.037\sigma^{-3}$ is shown in fig. 4.17(a). The figure shows that the snapshot has statistically similar network of micellar chains as in the smaller box size shown in Fig.4.9. The Fig.4.17(b) shows a magnified image of one of the junctions of the network. Moreover, some of the runs were also given involving only Monte Carlo moves for lower densities. Those runs also produce statistically similar results. The results for two of such runs are shown in Fig.4.18 for $\rho_m = 0.093\sigma^{-3}$, $\sigma_n = 1.5\sigma$ and $\sigma_{4n} =$ (a) 2.25σ and (b) 2.5σ. The corresponding snapshots are shown in Fig.4.19.

As seen in the snapshots of Figures.4.10(h), 4.11(h) and 4.12(g)&(h), the anisotropy of the NP clusters depends on the micellar density. Moreover, the nanoparticle clusters that form a percolating network as in Figs.4.9(e), 4.10(e), 4.11(e) and 4.12(e) also differ in their anisotropy thereby resulting in different pore shapes. Since, the structure of the nanoparticles also effects the arrangement of chains, or vice versa, the arrangement of micellar chains can be used to indirectly interpret the anisotropy of the NP structures. The distribution of angle between micellar chains $P(\theta)$ is analyzed and the plots are shown in Fig.4.20 for $\rho_m = 0.037\sigma^{-3}, 0.074\sigma^{-3}, 0.093\sigma^{-3}$, and $0.126\sigma^{-3}$ from (a) to (d), respectively. It is calculated by,

$$P(\theta) = \frac{N(\theta)}{\sum_\theta N(\theta)}, \tag{4.2}$$

where, $N(\theta)$ is the total number of pair of chains at an angle θ and the angle θ between two chains is calculated by using the largest eigenvectors of the corresponding gyration tensors of the chains as follows,

$$\theta = \cos^{-1} \frac{\vec{e_1}.\vec{e_2}}{|\vec{e_1}||\vec{e_2}|}, \tag{4.3}$$

where, $\vec{e_1}$ and $\vec{e_2}$ are the largest eigenvectors of the gyration tensors of the two chains.

The distribution $P(\theta)$ is normalized for different values of σ_{4n} by dividing it by the number of all possible combinations of the pair of chains. Each plot in Fig.4.20 shows the distribution of angles between micellar chains for different values of σ_{4n} as indicated in the figures. The lowest density of micellar system considered $\rho_m = 0.037\sigma^{-3}$ shows a high value of the distribution around 90° for all values of σ_{4n}. This shows the perpendicular arrangement of micellar chains at the network junction, as can be seen in the Fig.4.17(b). The similar correlation plots in Fig.4.13 and the same distribution function for angles in Fig.4.20(a) for $\rho_m = 0.037\sigma^{-3}$ confirms the similarly periodic architecture of monomers networks for all σ_{4n} as shown in Fig.4.9. The distribution plots for the monomer densities $\rho_m = 0.074\sigma^{-3}$ and $0.0931\sigma^{-3}$ in figures 4.20(b) and (c) shows that after a particular value of σ_{4n}, there appear two peaks around 10° and 90° indicating a preference for a parallel and a perpendicular arrangement of micellar chains, respectively. These are the densities where NPs form sheet-like structures. The parallel arrangement indicates that the chains within an aligned micellar domain form sheet-like structures. The peak around 90° in the distribution plot corresponds to the perpendicular arrangement of these sheet-like domains of aligned micellar chains. We find the formation of sheet-like domains to be unexpected and interesting, and the reason for this will

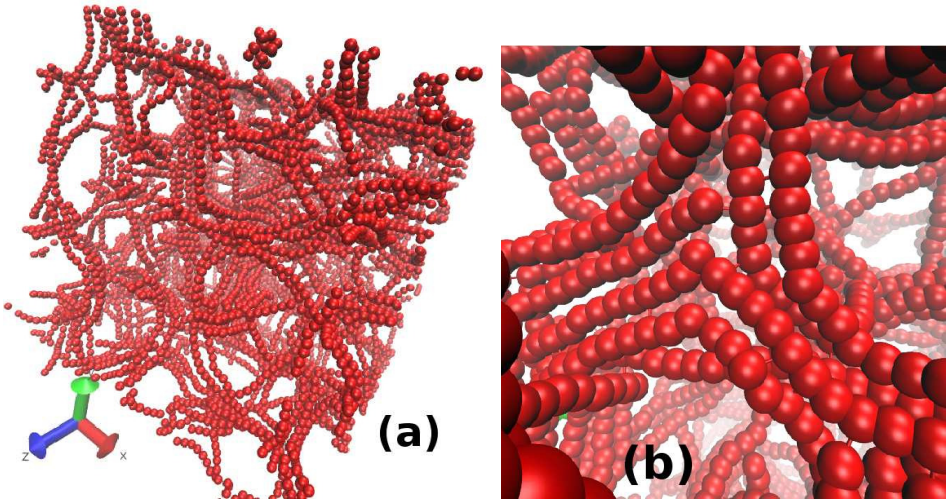

FIGURE 4.17: The representative snapshot in (a) shows only the monomer configurations from a NP + micellar-polymer system for $\sigma_{4n} = 2.5\sigma$ for the lowest value of monomer number density $\rho_m = 0.037\sigma^{-3}$ for simulations performed in a larger box size of $60 \times 60 \times 60\sigma^3$. This monomer-network is similar to the monomer-network structures obtained in a smaller box size 0f $30 \times 30 \times 30\sigma^3$ as shown in Fig.4.9. A magnified image of one of the network junction is shown in figure (b). Irrespective of the value of σ_{4n}, all the network structures obtained for $\rho_m = 0.037\sigma^{-3}$ produce statistically similar monomeric network structures (with the same periodicity).

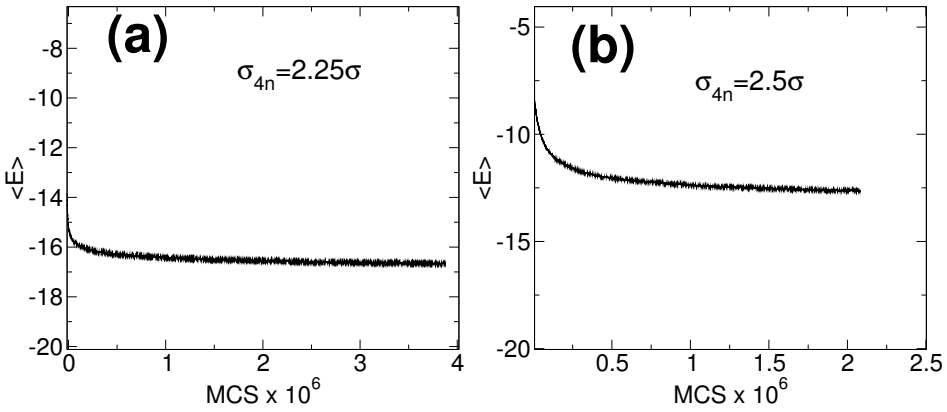

FIGURE 4.18: The figure shows the evolution of the energy graphs using only Monte Carlo runs for $\rho_m = 0.093\sigma^{-3}$ and $\sigma_n = 1.5\sigma$ for two different values of σ_{4n} (a) 2.25σ and (b) 2.5σ. These graphs correspond to the snapshots shown in Figs.8b (or 8(f)) and 8(c) (or 8(g)) in the main text. Initialized with the random positions of monomers and nanoparticles and evolved using Monte Carlo technique, these runs produce similar structures as shown in the corresponding figures in the main text. The snapshots corresponding to these graphs are shown in the next figure (Fig.4.19).

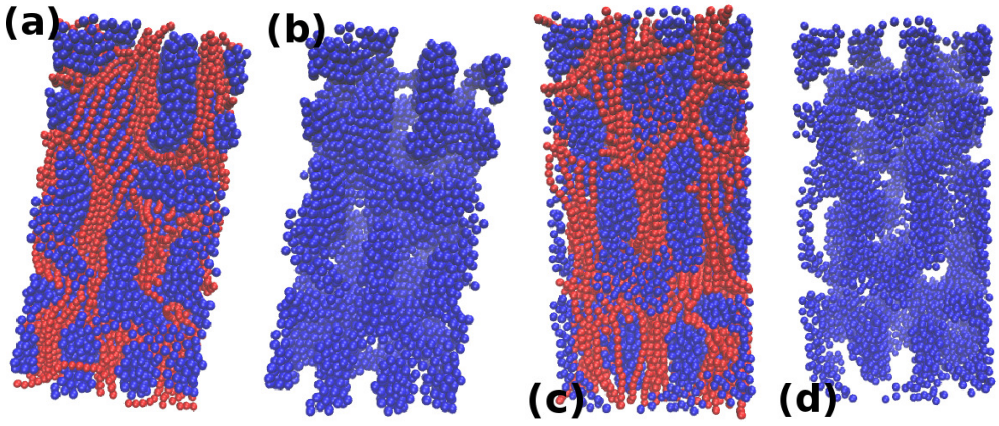

FIGURE 4.19: The figure shows the snapshots corresponding to the graphs shown in Fig.4.18 for $\rho_m = 0.093\sigma^{-3}$ and $\sigma_n = 1.5\sigma$ for two different values of $\sigma_{4n} = 2.25\sigma$ ((a) and (b)) and 2.5σ ((c) and (d)). The snapshots (a) and (c) show both the monomers (red) and nanoparticles (blue) while, snapshots in (b) and (d) show only nanoparticles. These figures correspond to the snapshots shown in Figs.8b (or 8(f)) and 8(c) (or 8(g)) in the main text. Initialized with the random positions of monomers and nanoparticles and evolved using Monte Carlo technique, these runs produce similar structures as shown in the corresponding figures in the main text.

be explained later in the text. All the neighbouring NP sheets as shown in Figure. 4.10 and 4.11 are arranged such that their planes are perpendicular to each other. Finally for the highest micellar density considered $\rho_m = 0.126\sigma^{-3}$, for $\sigma_{4n} \geq 2\sigma$, there appears a high peak around 10°. Here, the presence of peaks only around 10° is indicative of the nematic ordering of micellar chains and correspondingly we observe the rod-like structure of NPs. The height of the peaks at 90° gradually reduces from (b) to (d) and resulting in only peaks for parallel arrangement in (d). This is indicative of the change in the anisotropy of NP clusters. This can be confirmed by calculating the shape anisotropy S_{AN} of NP clusters using the following formula,

$$S_{AN} = 1 - 3\frac{\lambda_1\lambda_2 + \lambda_2\lambda_3 + \lambda_1\lambda_3}{(\lambda_1 + \lambda_2 + \lambda_3)^2}, \tag{4.4}$$

where, $\lambda_1, \lambda_2, \lambda_3$ are the eigenvalues of the gyration tensor of the NP cluster. Using the above formula, the average shape anisotropy of the nanoparticle clusters shown in snapshots of Figs.4.10(h), 4.11(h) and 4.12(h) is calculated to be $0.165, 0.211$ and 0.414, respectively. This shows that the shape anisotropy of the NP clusters increases with the increase in micellar density and the shape of the NP clusters is varying from sheet-like to rod-like structures. This shows that the anisotropy of the NP structures increases with increase in micellar density with nanostructures varying from sheets to rod-like structures.

4.3.5 The morphological changes: our understanding

The purpose of the introduction of the parameter σ_{4n} is to control the minimum approaching distance between micelles and NPs, but it also influences the arrangement and the number of NPs in the system and hence affects the effective volume of micelles. An increase in the value of σ_{4n} indicates an increase in the effective volume of micelles. We remind the reader that, as discussed at the beginning of the section

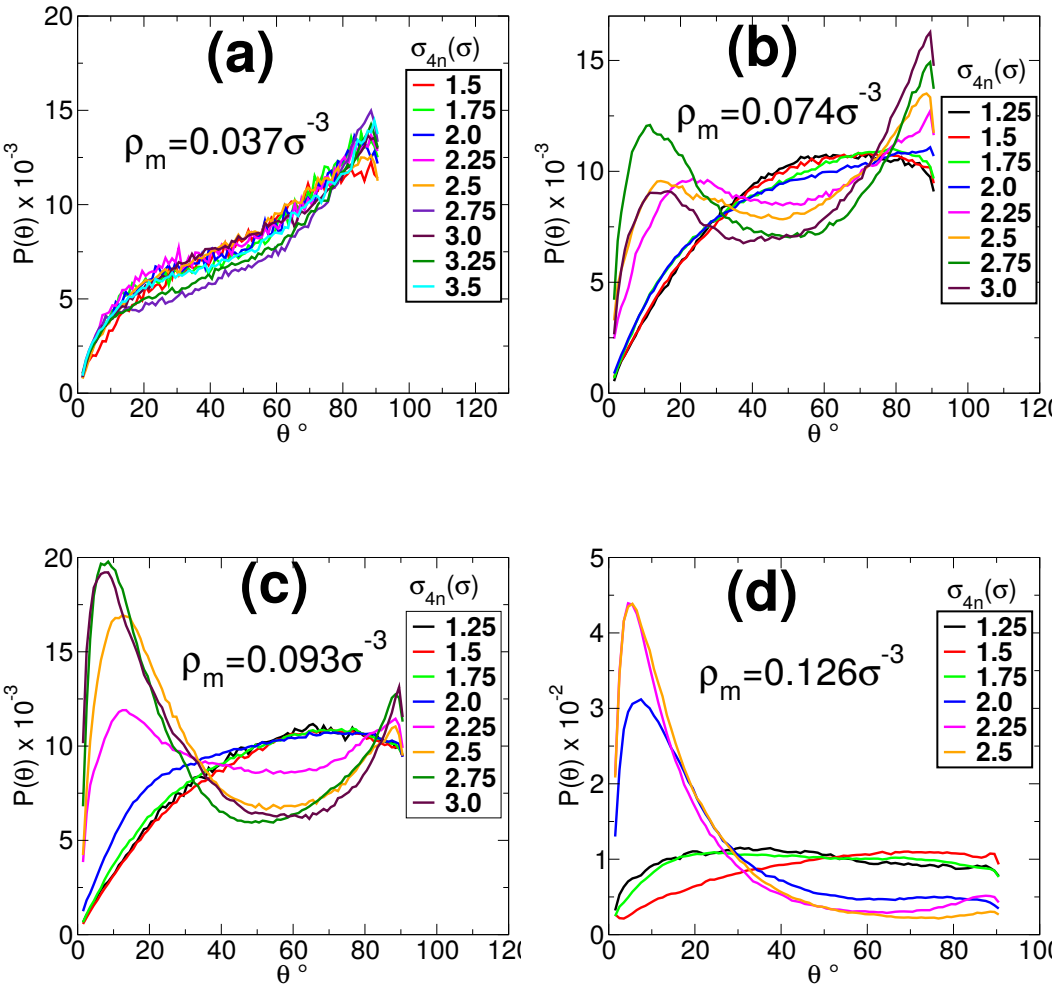

FIGURE 4.20: The figure shows the distribution of angles subtended between pairs of micellar chains at different values of monomer densities, ρ_m = (a) $0.037\sigma^{-3}$, (b) $0.074\sigma^{-3}$, (c) $0.093\sigma{-}3$ and (d) $0.126\sigma^{-3}$, respectively. Each figure shows graphs for different values of σ_{4n}. For the lowest micellar density (a), it shows a peak at 90° angle, hence confirming that many of the polymers lie to each other, as seen in snapshots of Fig.4.17(b). Plots in (b) and (d) show two peaks one around 10° and the other around 90°. The peak around 10° corresponds to the formation of aligned domains of micellar chains which result in sheet-like structures, while the peak around 90° shows the perpendicular arrangement of these sheet-like domains. The figure (d) shows a peak for a parallel arrangement of micellar chains which in turn results in the formation of rod-shaped aggregates of nanoparticles.

(refer Fig.4.1), the effective volume of micelles also gets modified by the density of NPs present in the system. In the presence of a large number of NPs (lower value of σ_{4n}), there are relatively more contacts between monomers and NPs, which leads to a higher value of the effective volume of monomers. Moreover, the number of contacts also depend on the assembly architecture and the relative organization between NPs and micellar chains. Therefore, the effective volume of micelles not only depends on the value of σ_{4n} but also on the NP density as well as the morphology and corresponding monomer-NP contacts. Hence, the effect of the transformation from a network-like structure to non-percolating clusters can be understood in terms of change in the effective volume of micelles.

From the experimental perspective, different values of σ_4 would correspond to micellar chains made up of different chemical compositions such that they have different diameters of micellar chains. Here, it is kept constant ($\sigma_4 = 1.75\sigma$). Now, with a given value of σ_4 and micellar density, it is the parameter σ_{4n} that effectively determines the space available for the incoming NPs inside the simulation box. Experimentally, in the micelle-NP mixture, the effective repulsion between micellar chains of a particular composition (with a particular value of σ_4) and NPs can be tuned in to change the value of σ_{4n} and thereby the effective volume available to NPs. That, in turn, will determine the morphology of NP mesostructures formed in the presence of a background micellar matrix.

A characteristic quantity that changes with the density of monomers is the average length of monomer chains. The average chain length of WLMs increases with increase in the value of monomer density. In the presence of a large number of NPs (in case of a system spanning network of NPs), monomers are more packed. This is also seen from the behaviour of $g(r)$ in Fig.4.16) and can be compared to the systems with a lower number of NPs which result in non-percolating clusters. Therefore, the effect of the change of NP morphology from network to non-percolating clusters is expected to be seen in the value of average chain length of micelles. We first discuss the behaviour of the average length of micellar chains with a change in σ_{4n}, because that will help us quantitatively better appreciate the behaviour of the effective volume fraction of micelles.

The behaviour of the average micellar chain length is shown in Fig.4.21(a). Different symbols indicate different micellar number densities. The average length at $\sigma_{4n} = 1.25\sigma$ increases with an increase in the number density of monomers. This is also consistent with the snapshots shown in Fig.4.3. In that figure, we observe longer chains for higher values of monomer number densities. An increase in the value of σ_{4n} from 1.25σ to 1.5σ, reverses this behaviour. This is due to the fact that, at $\sigma_{4n} = 1.5\sigma$, the micellar chains undergo a change in their arrangement from a dispersed to a network-like structure with clusters of micellar chains. This transition is such that the network-like structure of NPs has the same period for all micellar densities (refer Fig.4.13 and the corresponding snapshots in Fig.4.9, 4.10(a), 4.11(a) and 4.12(a)). At $\sigma_{4n} = 1.5\sigma$, with the same periodicity of NP networks (refer Fig.4.13), micellar chains with a high ρ_m are more "crushed" (having smaller chains) compared to the systems with lower density. Therefore, denser micellar systems have a lower average length of micellar chains for this particular value of σ_{4n}. This can also be realized by comparing the snapshots shown in Fig.4.9(a), 4.10(a), 4.11(a) and 4.12(a). With further increase in the value of σ_{4n}, the number of nanoparticles in the system decreases and the NP networks start breaking. Therefore, the micellar monomers get some space to join and form longer chains, thus increasing the chain length. Due to the presence of a higher number of monomer-nanoparticle contacts in the systems with higher monomer densities, the effect of the increase in the value of σ_{4n} is also

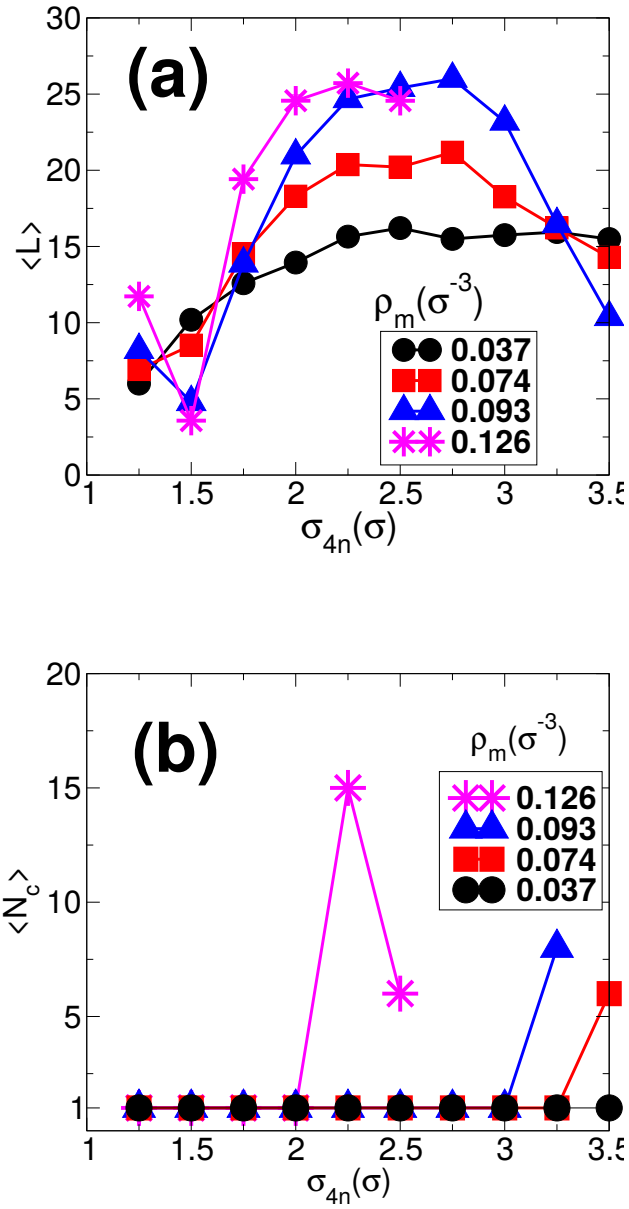

FIGURE 4.21: (colour online) Figure (a) shows the variation in the average length $\langle L \rangle$ of micellar chains with σ_{4n} where L is the number of monomers in a particular chain. Figure (b) shows the plot for the number of nanoclusters $\langle N_c \rangle$ in the system. The quantity $\langle L \rangle$ shows a decrease in its value at a higher value of σ_{4n} where the number of nanoparticles decreases and the nanoparticle network breaks into non-percolating clusters. Due to this, the effective density of micellar chains decreases and hence, the average length of micellar chains decreases. The quantity $< N_c >$ shows a jump from its value of 1 to a larger value when the nanoparticle network breaks into non-percolating clusters. The nanoparticles aggregates with $< N_c >= 1$ spans the length of the simulation box as seen in the snapshots and also confirmed by calculating the largest eigenvalue of the gyration tensor for these aggregates.

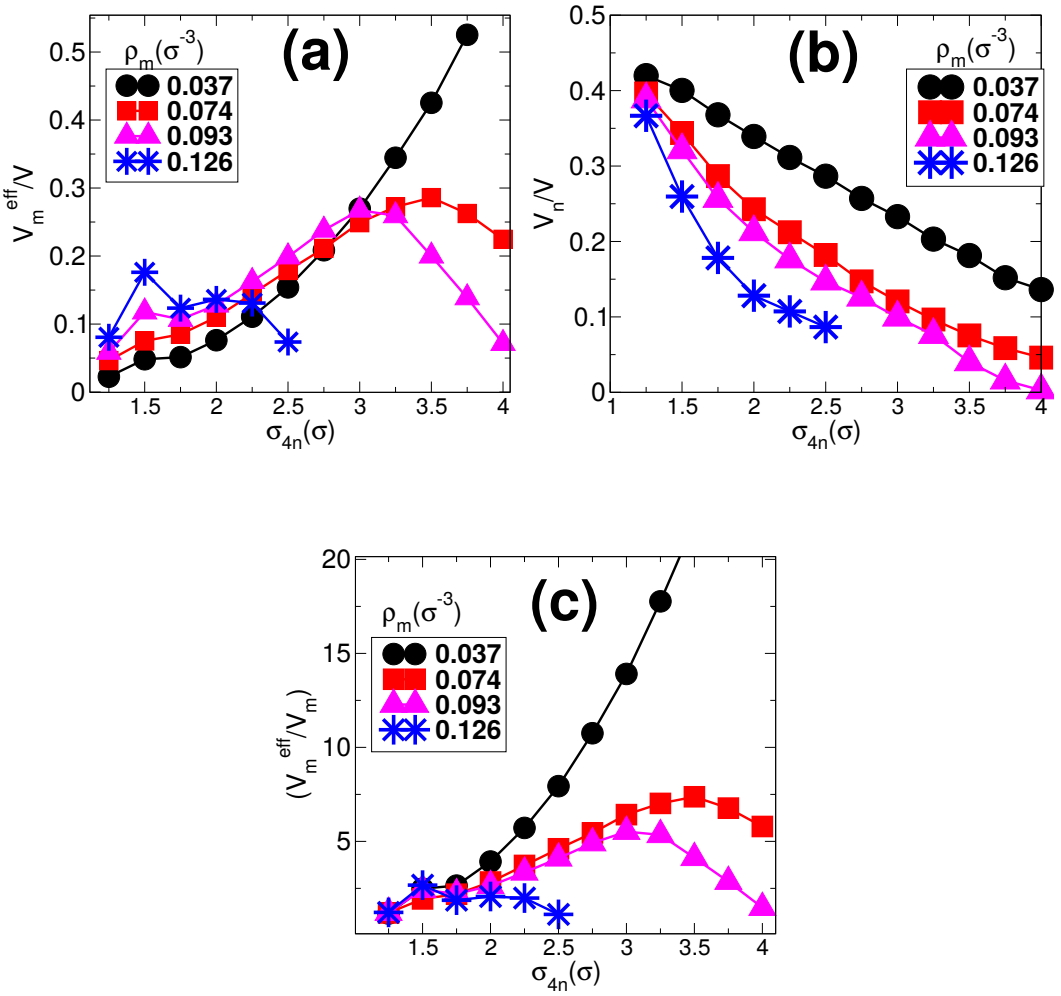

FIGURE 4.22: (colour online) The figure shows the behaviour of (a) effective monomer volume fraction (${V_m}^{eff}/V$), (b) nanoparticle volume fraction (V_n/V) and (c) the ratio of effective monomer volume to the monomer volume (${V_m}^{eff}/V_m$), with change in the value of σ_{4n}, where $V_m = \rho_m 4/3\pi(\sigma/2)^3 V$. Each figure shows graphs for four different values of number density of monomers i.e. $\rho_m = 0.037\sigma^{-3}, 0.074\sigma^{-3}, 0.093\sigma^{-3}$ and $0.125\sigma^{-3}$ as indicated by the symbols. With an increase in the value of σ_{4n}, the nanoparticle volume fraction in (b) decreases while the effective monomeric volume fraction in (a) increases. At a higher value of σ_{4n}, the monomeric volume fraction shows a decrease in its value indicating a change of nanoparticle structure from network to non-percolating clusters. In figure (c), the graph represents the variation of the ratio of the effective monomer volume fraction to the monomer volume fraction. In other words, it represents the extent of the effect of the repulsive interactions on effective monomer volume fraction. A high value of ${V_m}^{eff}/V_m$ indicates that the presence of a large number of interacting pairs having repulsive interactions V_4 and V_{4n}, which have a cut-off distances σ_4 and σ_{4n}, respectively. The graph in (c) shows high values for intermediate values of σ_{4n}, where the system shows the formation of a network-like structure of nanoparticles. However, for very low values or high values of σ_{4n}, the ratio $V_m/{V_m}^{eff}$ shows low values (~ 0.1 for $\rho_m = 0.126\sigma^{-4}$). This shows that the constituent particles in the system are away from each other, i.e., at a distance greater than the cutoff distances of the repulsive interactions V_4 and V_{4n}, for very low or higher values of σ_{4n}.

higher. Therefore, for the same increase in the value of σ_{4n} beyond 1.5σ, the decrease in the number of nanoparticles is more for a higher value of ρ_m. Hence, the nanoparticle network is "*more broken*" for higher ρ_m. Hence, the average length reverses its behaviour at 1.75σ, and the average length again increases with ρ_m as was seen for the $\sigma_{4n} = 1.25\sigma$ system.

As explained earlier, the effective polymeric chain volume depends on the combination of the value of σ_{4n}, the NP number density and more importantly, the number of contacts with NP and monomers. Therefore, at a higher value of σ_{4n} ($> 2.5\sigma$ when the introduction of NPs inside the system becomes relatively difficult), the number of NPs in the system decreases. Due to this, the effective micellar volume decreases and hence, a decrease in the average length of micellar chains can be seen. Lower the number of NPs in the system, lower is the connection between the percolating network. Thus, decrease in the average length shows the extent of the breaking of NP network, and the breaking of network-like structures to non-percolating clusters of NPs is recorded once the average length of chains starts to decrease. This occurs at $\sigma_{4n} = 2.25\sigma, 3.25\sigma$ and 3.5σ for the values of micellar densities $\rho_m = 0.126\sigma^{-3}, 0.093\sigma^{-3}$ and $0.074\sigma^{-3}$, respectively. Thus, the behaviour of the average length of micelles clearly indicates the existence of two points of structural changes. The first one is for the change from dispersed state to clustering of micellar chains (from $\sigma_{4n} = 1.25\sigma$ to $\sigma_{4n} = 1.5\sigma$), and the other is for the breaking of NP network into non-percolating clusters at some higher value of σ_{4n} depending on micellar density. The second point where the nanoparticle network breaks from percolating to non-percolating clusters decreases in σ_{4n} with an increase in the micellar density. Thus the peak in the average length gets broader and shifts to the right as the value of micellar density decreases. This peak corresponds to 2.25σ and 2.5σ for the values of $\rho_m = 0.126\sigma^{-3}$ and $0.093\sigma^{-3}(0.074\sigma^{-3})$. The decreasing part of the graph is not yet reached for the case of $\rho_m = 0.037\sigma^{-3}$.

Since the change in average length indirectly indicates a change in the effective volume of micelles, a decrease in the effective volume of micelles is expected around the point of transformation. To confirm these observations, the behaviour of the volume fractions of the constituents and the average energies of NPs and monomers are examined, and the plots are shown in Figs.4.22 and 4.23, respectively.

The Fig.4.22 shows (a) the plot of the effective monomer volume fraction ${V_m}^{eff}/V$ (b) NP volume fraction V_n/V and (c) the ratio of effective volume fraction of monomers to monomers volume fraction ${V_m}^{eff}/V_m$. Change in the value of σ_{4n} from 1.25σ to 1.5σ corresponds to the formation of clusters of micellar chains from a dispersed state, as discussed before. These clusters of micellar chains join to form a system spanning network-like structure. With further increase in σ_{4n}, the effective volume fraction of monomers increases at first but then starts to decrease after a certain value of σ_{4n} ($> 2.5\sigma$) for the highest three number densities. The decrease in the value of the effective volume fraction of monomers corresponds to the transition from the network-like structure of nanoparticles to non-percolating clusters. This happens at $\sigma_{4n} = 2.25\sigma$ for $\rho_m = 0.126\sigma^{-3}$, $\sigma_{4n} = 3.25\sigma$ for $\rho_m = 0.093\sigma^{-3}$ and at $\sigma_{4n} = 3.5\sigma$ for $\rho_m = 0.074\sigma^{-3}$. This change in nanoparticle structure is not observed for the lowest density of micelles for the values of σ_{4n} considered here. Hence, ${V_m}^{eff}/V_m$ keeps on increasing for $\rho_m = 0.037\sigma^{-3}$. In Fig.4.22(b), the nanoparticle volume fraction decreases with increase in σ_{4n} as introducing nanoparticles in the system becomes increasingly difficult with increasing σ_{4n}.

The ratio of the effective volume fraction of monomers to their actual volume

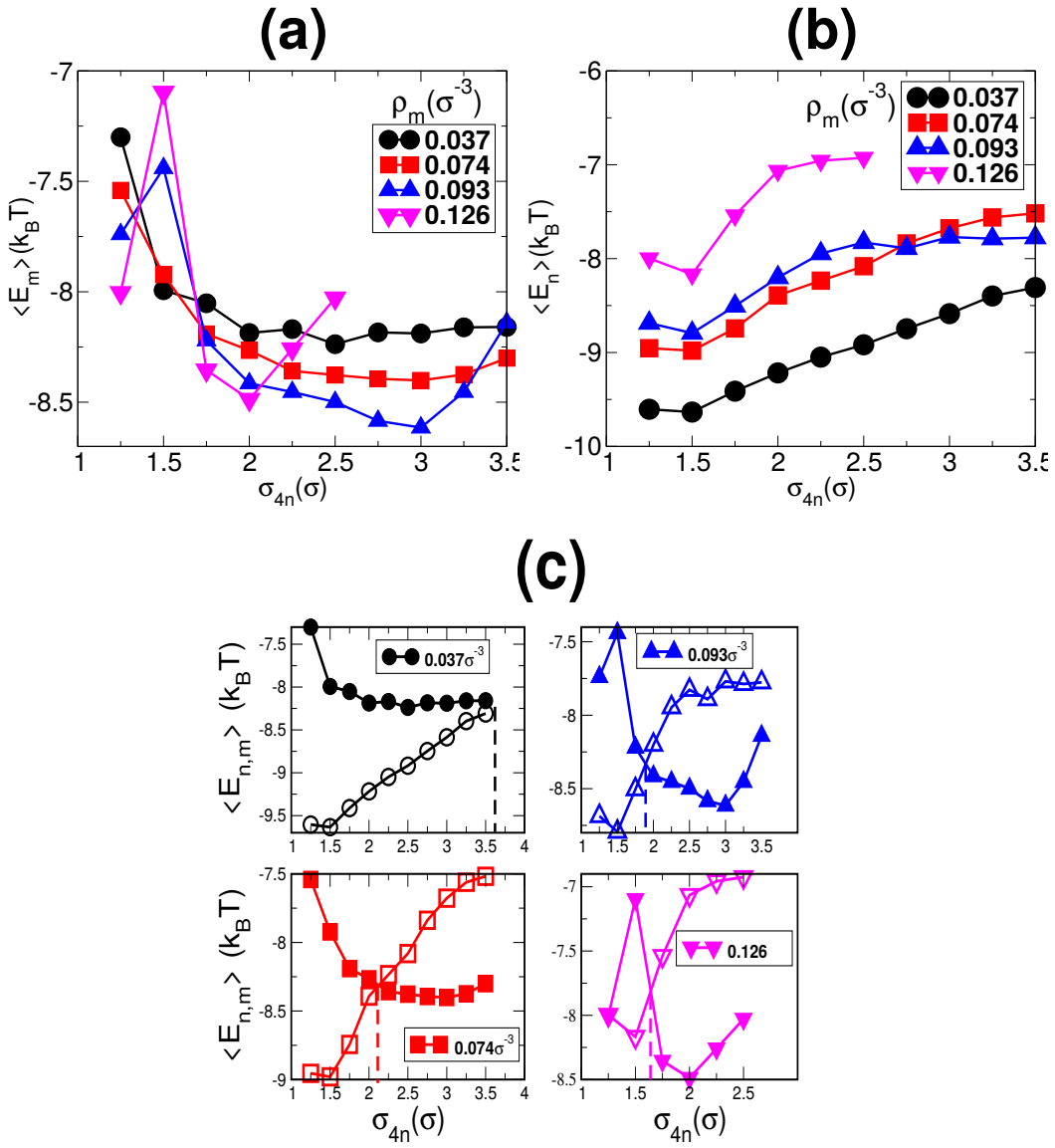

FIGURE 4.23: The Figure shows graphs for variation in the average potential energy (PE) of (a) monomers, (b) nanoparticles and for different values of monomer densities. Plot (c) shows the monomer and NP PEs in the same plot, but each subfigure shows data for a particular value of ρ_m. With an increase in the value of σ_{4n}, the nanoparticle energy decreases while the energy of micelles increases. At a higher value of σ_{4n}, the monomer volume fraction shows a decrease in its value marking the change from network-like structure to non-percolating clusters of nanoparticles. In (c), the lines showing variation in monomer PE (filled symbols) and PE of nanoparticles (empty symbols) intersects at some intermediate value of σ_{4n}. The change from network to non-percolating clusters of the nanoparticle takes place at a value of σ_{4n} higher than the σ_{4n}-value at which the intersection occurs. The points of intersections of the energies of monomers and nanoparticles for different values of monomer densities are indicated by the vertical lines which get shifted to lower values of σ_{4n} with the increase in micellar densities. Therefore, with an increase in the micellar densities the point of change of nanoparticle morphology from network to non-percolating clusters also gets shifted to a lower value of σ_{4n}.

fraction [refer Fig.4.22(c)] shows the extent of the effect of σ_{4n} on the effective volume fraction of micelles. Its behaviour is exactly similar to the behaviour of the effective volume of monomers. The behaviour of the ratio ${V_m}^{eff}/V_m$ indicates the role of σ_{4n} and micellar density in the arrangement of constituent particles and hence the morphology of the system. A high value of ${V_m}^{eff}/V_m$ is obtained when there exists a clustering of micellar chains as a consequence of an increase in σ_{4n}. When $(V_m^{eff}/V_m) \approx 1$, it shows a dispersed state of micellar chains.

The Fig.4.23 shows the graphs of average energy per particle of (a) monomers $\langle E_m \rangle$ and (b) NPs $\langle E_n \rangle$. The plot in (c) shows the average energy per particle for both monomers (filled symbols) and NPs (empty symbols), with data for different values of densities shown in separate graphs. For the change in σ_{4n} from 1.25σ to 1.5σ, the $\langle E_m \rangle$ shows an increase in its value for $\rho_m = 0.126\sigma^{-3}$ and $\rho_m = 0.093\sigma^{-3}$ while, it decreases for $\rho_m = 0.074\sigma^{-3}$ and $\rho_m = 0.037\sigma^{-3}$. This change corresponds to the transition of polymeric chains from dispersed state to the network of its clusters. We can consider that these networks are formed in between the network of nanoparticle aggregates. This is because the volume fraction of nanoparticles is higher than the effective volume fraction of monomers. The network of monomer chains show same periodicity of the structure for all ρ_m (refer Fig.4.13) at $\sigma_{4n} = 1.5\sigma$. Therefore, the monomers with number densities $\rho_m = 0.126\sigma^{-3}$ and $\rho_m = 0.093\sigma^{-3}$ are "crushed" in between nanoparticle clusters forming smaller chains compared to the systems with number densities $\rho_m = 0.037\sigma^{-3}$ and $\rho_m = 0.074\sigma^{-3}$ (refer Fig.4.21).

The existence of smaller chains in the box increases the values of both V_2 and V_4 for $\rho_m = 0.126\sigma^{-3}$ and $\rho_m = 0.093\sigma^{-3}$. Hence, the energy of monomers $\langle E_m \rangle$ shows an increase in its value for $\rho_m = 0.126\sigma^{-3}$ and $\rho_m = 0.093\sigma^{-3}$ but decreases for $\rho_m = 0.037\sigma^{-3}$ and $\rho_m = 0.074\sigma^{-3}$, for the same change in value of σ_{4n} from 1.25σ to 1.5σ. For the same change in σ_{4n} (from 1.25σ to 1.5σ), the energy of NPs $\langle E_n \rangle$ show a decrease in their value. This decrease in nanoparticle energy is a result of an increase in the packing of nanoparticles due to increase in σ_{4n}.

With further increase in σ_{4n}, $\langle E_m \rangle$ decreases while $\langle E_n \rangle$ shows an increase. This decrease in the $\langle E_m \rangle$ is due to the increase in the effective volume fraction of monomers whcih results in an increased chain length. However, $\langle E_m \rangle$ again shows an increase after $\sigma_{4n} = 2\sigma$, $\sigma_{4n} = 3\sigma$ and $\sigma_{4n} = 3.25\sigma$ for $\rho_m = 0.126\sigma^{-3}$, $\rho_m = 0.093\sigma^{-3}$ and $\rho_m = 0.074\sigma^{-3}$, respectively. This increase in the value of $\langle E_m \rangle$ corresponds to the breaking of the nanoparticle network into non-percolating clusters that results in the decrease in micellar chain length (refer Figs.4.21 and 4.22(a)). Thus the dependence of average monomer energy on ρ_m changes for the change in σ_{4n} from 1.25σ to 1.5σ, this is a consequence of the change from a dispersed state of chains of monomers to a network-like structure.

Moreover, the transition from nanoparticle network to non-percolating clusters is also indicated by an increase in $\langle E_m \rangle$ for higher values of $\sigma_{4n} > 1.5\sigma$. In Fig.4.23(c) shows the variation in E_m and E_n with σ_{4n} on the same plot for each value of ρ_m, the points of intersection of both the energies are shown by vertical lines (dashed). As the NP network gradually breaks with the increase in σ_{4n}, the NP energy decreases and energy of monomers increases. At a value of σ_{4n}, just higher than the point of intersection of these two energy plots, the nanoparticle network breaks into individual clusters. With the decrease in micellar density ρ_m, the point of intersection of the two energies gets shifted to higher values of σ_{4n}. Therefore, the value of σ_{4n} at which the NP network breaks into non-percolating clusters also gets shifted to higher values with the decrease in micellar density.

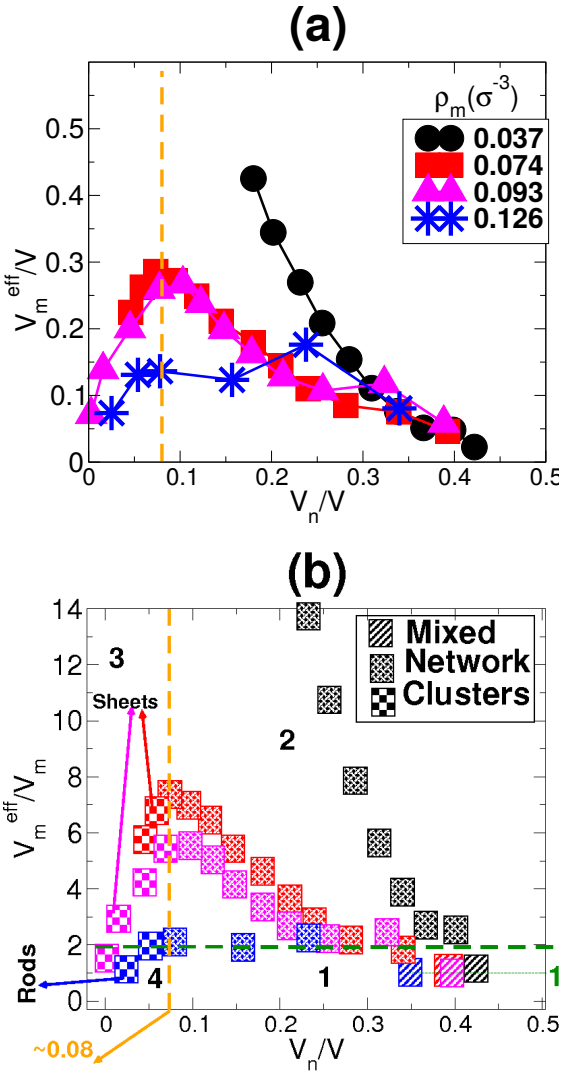

FIGURE 4.24: (a) The figure shows the effective volume fraction ${V_m}^{eff}/V$ of equilibrium polymers (micelles) versus the nanoparticle volume fraction V_n/V. The vertical broken line (orange) separates the values of V_n/V which correspond to formation of network morphology of NPs and micelles (right of the vertical line) from the V_n/V values which correspond to the non-percolating clusters of NPs (left of vertical line). The exceptions to network morphology are the points with the highest nanoparticle volume fraction for each rho_m. These correspond to the mixed-phase of NPs and micellar chains. (b) The figure shows the replot of the figure shown in (a) with the variable shown in Y-axis replaced by the ratio of ${V_m}^{V_m}$ and the symbols indicating the morphology of the system. These two lines divide the graph into four different regions marked as 1, 2, 3 and 4. The points in region-1 are for $\sigma_{4n} = 1.25\sigma$ which form a dispersed state (no clustering) of micellar chains (all joined by a (thin-green) horizontal line intersecting the Y-axis at ≈ 1). Region-2 shows the systems with network-like structures of both nanoparticles and micellar chains. Regions-3 belongs to the systems forming non-percolating clusters of nanoparticles in between the clusters of micellar chains. Finally, the region-4 depicts the systems with non-percolating clusters of nanoparticles in the background matrix of dispersed micellar chains.

All these observations can be well explained in a plot of effective micellar volume fraction versus NP volume fraction, which is shown in Fig.4.24(a). Different monomer number densities are represented by different symbols. The orange coloured dashed vertical line divides the parameter region where NP network structures are observed from the region of parameters where NPs form non-percolating clusters. All the points to the left of this line show the systems with non-percolating clusters of NPs, while all the points to the right show the percolating network-like structures of both NPs and polymeric chains. The rightmost point for each case of micellar density (the maximum value of NP volume fraction for each ρ_m) belongs to the system which has polymeric chains dispersed in between NPs. In this plot, the regions having the points showing uniformly dispersed and network-like structures of micellar chains are not well separated, and they overlap. If we replot this graph with the variable along the Y-axis replaced by ${V_m}^{eff}/V_m$, then the regions with the dispersed and the network of clusters of micellar chains can also be captured, and both the morphological transformations can be clearly marked on the graph. This is shown in Fig.4.24(b).

In Fig.4.24(b), the ratio ${V_m}^{eff}/V_m$ shows the extent of the effect of change in σ_{4n} on the effective volume of micelles (refer Fig.4.22(c)). The different morphologies of the system are indicated by the different symbols. For any symbol, the different colours correspond to the different micellar densities. At $\sigma_{4n} = 1.25\sigma$ and for all the values of ρ_m, the value of the ratio ${V_m}^{eff}/V_m$ remains ≈ 1. All such points are joined by a horizontal line (thin-broken-green) intersecting the Y-axis at ≈ 1. An increase in the value of σ_{4n} from 1.25σ to 1.5σ leads to the onset of formation of clusters of micellar chains. All such points with a network-like structure of polymeric chains are indicated by the corresponding symbol spanning over a large parameter space in the graph. All the points that show a network-like structure of clusters of micellar chains occurs above a value of ${V_m}^{eff}/V_m \approx 2$ that is shown by a dashed horizontal line (green). Therefore, this line approximately marks the change from a uniformly dispersed state to a network-like structure of micellar chains. With further increase in σ_{4n}, the NP volume fraction decreases and effective monomer volume fraction increases. At an even higher value of σ_{4n} (depending on ρ_m), the NP networks break to form non-percolating clusters. This is marked by a decrease in the value of the effective volume of micelles, and all such points are shown by the corresponding symbol for non-percolating clusters of NPs. Depending on the number density of monomers, the morphology of these non-percolating clusters changes from sheets to rod-like structures (with increasing ρ_m). For all the values of ρ_m, the change from network-like morphology to non-percolating clusters of NPs is observed to occur at a value of NP volume fraction ≈ 0.08. This is marked by a dashed vertical line (orange).

The combination of the vertical line (orange-broken) and the horizontal line (green-broken) divides the space into four different regions which are marked as 1, 2, 3 and 4. Each region defines the structural morphology of the system as follows;
Region 1: Uniformly mixed state of micellar chains and nanoparticles with micellar chains dispersed in between nanoparticles.
Region 2: Both the polymeric chains and the nanoparticles form network-like structures which interpenetrate each other.
Region 3: Individual clusters of nanoparticles in between the clusters of micellar chains.
Region 4: In this region all the points show the value of $\frac{{V_m}^{eff}}{V_m} \approx 1$, therefore, the

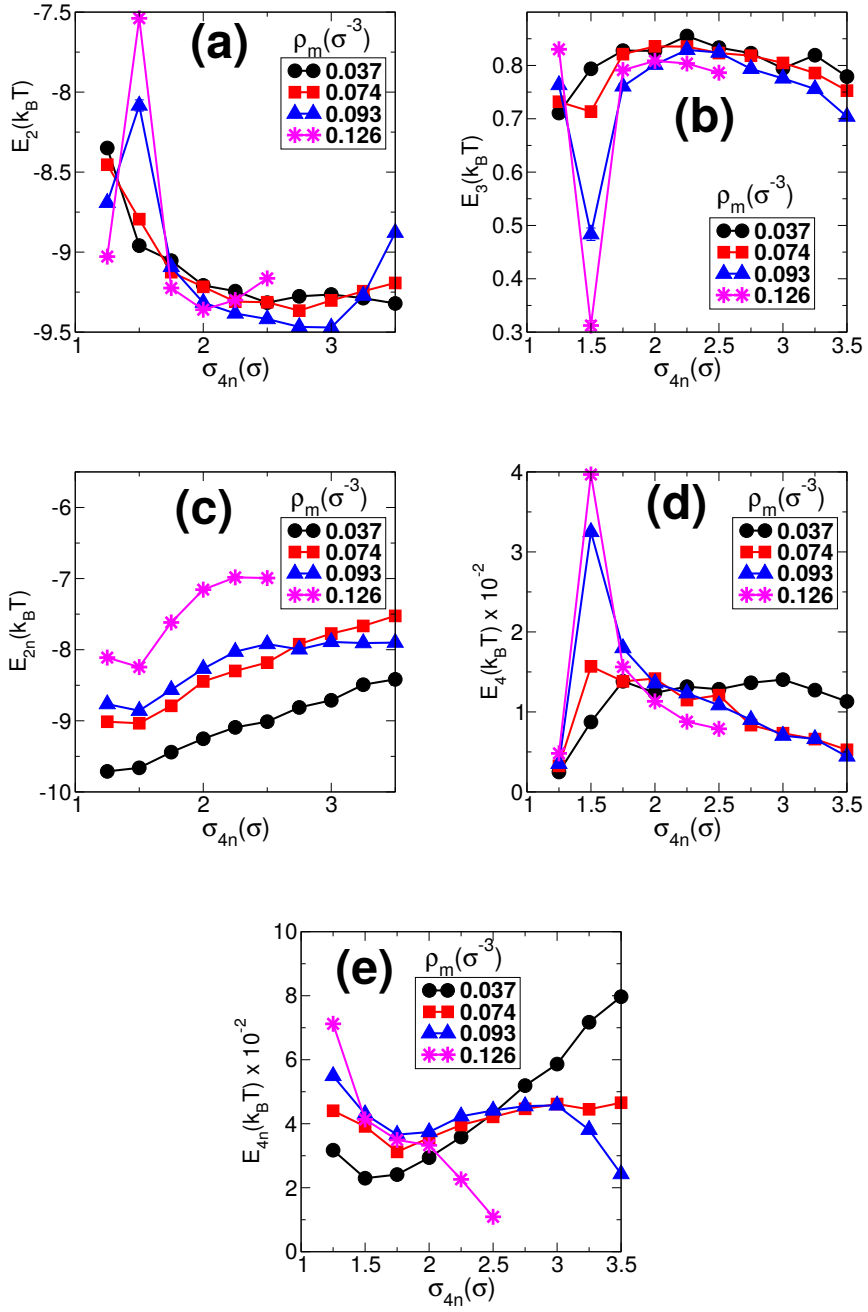

FIGURE 4.25: The figure shows the variations of the potential energies due to (a) $V_2, (b)V_3, (c)V_{2n}, (d)V_4$ and (e) V_{4n} with the excluded volume parameter σ_{4n}. The potentials are explained in the modeling section. All the points are represented along with the error bars for 10 independent runs. The error bars are too low to be visible for all the plots.

monomer chains are in a dispersed state. However, the nanoparticles form non-percolating clusters. Therefore, in this region, non-percolating clusters of nanoparticles are present in the background of dispersed chains of micelles.

All the observations discussed in this chapter for the NP-micellar system can be verified by examining the behaviour of the potential energies involved in the system. The plots of these potential energies $E_2, E_3, E_{2n}, E_4, E_{4n}$ are shown in Figs.4.25(a), (b), (c), (d) and (e) due to the potentials V_2, V_3, V_{2n}, V_4 and V_{4n}, respectively. All the potential energy values are averaged over 10 independent runs with $(15-20)\times 10^5$ iterations for each run and are plotted with an error bar. The error bars are too small to be visible. Moreover, these potential energies are normalized by dividing them with the number of all combinations of the particles that are interacting with the concerned potential. A lower value of E_2 indicates a higher average length of the chains and vice versa. The behaviour of E_2 in Fig.4.25(a) shows an increase in its value for a change of $\sigma_{4n} = 1.25\sigma$ to 1.5σ for $\rho_m = 0.126\sigma^{-3}$ and $\rho_m = 0.093\sigma^{-3}$ indicating scission of chains. Apart from these two points E_2 decreases with increase in σ_{4n} for all monomer densities indicating the increase in chain lengths. However, with further increase in σ_{4n}, it shows a decrease in its value (except $\rho_m = 0.037\sigma^{-3}$). This happens at $\sigma_{4n} = 2.25\sigma$ for $\rho_m = 0.126\sigma^{-3}$ and at $\sigma_{4n} = 3.25\sigma$ for $\rho_m = 0.093\sigma^{-3}$ and $0.074\sigma^{-3}$. Thus, it confirms the behaviour of the average length of chains shown in Fig.4.21.

Figure 4.25(b) shows the behaviour of E_3 with σ_{4n} for different values of ρ_m. Longer chains will give rise to a large number of bonded triplets along a chain resulting in a higher value of E_3 while, smaller chains will result in a lower value of E_3. Therefore, the decrease in the value of E_3 for change of $\sigma_{4n} = 1.25\sigma$ to 1.5σ for $\rho_m = 0.126\sigma^{-3}$ and $\rho_m = 0.093\sigma^{-3}$ is indicative of the formation of smaller chains at 1.5σ. Moreover, with further increase in the value of σ_{4n}, E_3 shows relatively higher values indicating the presence of longer chains. The interaction potential energies between NPs E_{2n}, shown in Fig.4.25(c), also shows a decrease at 1.5σ indicating an increase in the packing of nanoparticles in spite of the decrease in its number density. It then shows an increase in its value at a higher value of σ_{4n} due to a decrease in its number density.

The potential energies E_4 in Fig.4.25(d) which shows the repulsive interaction between micellar chains shows an increase in its value when the micellar chains transform to a network-like structure at $\sigma_{4n} = 1.5\sigma$ from a dispersed state at $\sigma_{4n} = 1.25\sigma$. The quantity E_4 then decreases, indicating that the average distance between micellar chains increases (chains get out of the range of the potential E_4) as σ_{4n} increases. The repulsive interaction energy between NPs and micellar chains E_{4n} shown in Fig.4.25(e) also shows the two points of morphological transformations, first a decrease in E_{4n} at $\sigma_{4n} = 1.5\sigma$ indicating the change in the structure of micellar chains from dispersed to clusters that join to form network-like structure. The decrease in E_{4n} is due to the re-organization of micellar chains to form clusters that reduce the number of monomer-NPs contacts. Then, it increases (or remains constant for $\rho_m = 0.126\sigma^{-3}$), but again show a decrease in its value when the morphology of NPs changes from a network-like structure to non-percolating clusters. This decrease is due to the low density of NPs present in the system at high σ_{4n}. The values of the repulsive potential energies E_4 and V_{4n} are of the order of $10^{-2}k_BT$, thereby, indicating that the rearrangement of the system architecture with the increase in σ_{4n} is to avoid the repulsive interactions within the system.

Thus, the plots of E_4 and E_{4n} with very low values (of the order of $10^{-2}k_BT$) points to the emergence of different kind of self-assembled structures as a result of

the system trying to decrease the interfacial or repulsive interactions. The repulsive interaction potential between NPs and micellar chains V_{4n} will form a phase-separated state at higher densities in order to reduce the repulsion between them. But the presence of the steep repulsive interaction potential within the micellar chains (V_4) themselves evokes a competition between the two potentials V_4 and V_{4n}. Micellar chains aligned parallelly with the average distance between chains $r < \sigma_4$, lead to a higher value of the potential energy due to V_4. Therefore, reducing the value of V_4 as well as V_{4n} not only requires a reduction of the interface area between micelles and NPs but also encourages micellar chains to arrange such that they are out of the range of the repulsive interaction V_4 acting between themselves. For a system with low monomer density (Fig.4.9), the perpendicular arrangement between micellar chains which meet at the junctions of the network (refer Fig.4.17(b) and Fig.4.20) is a consequence of the requirement to reduce the repulsive interaction between them. By remaining at an angle of 90°, the possibility of the chains of monomers coming in contact with each other is very low. With an increased density of micelles (Fig.4.10 and 4.11), the average length of the micellar chains also increases. Therefore, for higher monomer density if the same structures as shown in figure 4.9 is maintained, it will lead to increased width of the clusters of micellar chains in the network resulting in high repulsive energy due to V_4. Hence, the micellar chains arrange in an aligned fashion forming thin sheet-like domains and relatively away from each other in order to reduce values of V_4. The steep increase of the potential V_4 with r_4 discourages those Monte Carlo steps which bring the monomers from adjacent chains just below σ_4, and thus the values of E_4 remains much lower than k_BT. Micellar chains which form sheet-like domains have a relatively lower number of neighbouring chains compared to chains in a hexagonally packed arrangement. Moreover, the arrangement of these sheetlike planes at an angle perpendicular to neighbouring domains (as noted in Figure. 4.20(b) and (c)) also seems to be the part of the strategy to lower the repulsive potential between micellar chains by reducing the possibility of contact between the domains. At even higher number densities of micelles, the chains become very long, and formation of a sheet-like structure would lead to an increase in the interfacial area between micellar sheets and NPs. This, in turn, will result in an increase in potential energy due to V_{4n}. Therefore, in this case, the NPs prefer to nematically arrange themselves with the polymeric chains maintaining a distance $r > 1.75\sigma$ from each other to be out of the range of the repulsive potential V_4.

Chapter 5

Conclusion and future directions

In this thesis, we examine in detail the behaviour of the mixture of nanoparticle (NPs) and equilibrium polymers (EPs), examples of which are wormlike micellar systems, with the variation of monomer number density and the excluded volume parameter (EVP) between micellar chains and nanoparticles. The density of monomers which self-assemble to form equilibrium polymers affect the self-organization of aggregates of NPs, which in turn affect the organization and length of the self-assembled polymeric chains. One obtains a number of interesting equilibrium or kinetically arrested configurations of NP morphologies, starting from a mixed phase of NPs and EPs, when the size of NPs are relatively small compared to the width of micellar chains. For higher values of the EVP, the morphology of the NP aggregates varies from porous percolating connected network of NPs, where the thickness of the pores can be suitably controlled by the EVP and number density of monomers to disconnected aggregates of NPs with varying shape anisotropy values. The NPs aggregate between clusters of semi-flexible polymeric chains, hence instead of nucleating to spherically symmetric aggregates, they develop into the anisotropic rod-like aggregates which grow parallel to the alignment of the background semi-flexible micellar matrix. We establish that the anisotropy of the NP clusters is governed by the density of the equilibrium polymeric matrix. Furthermore, the steep repulsive potential between neighbouring micellar chains and its contribution relative to the repulsive potential between chains and NPs can lead to the formation of a planar sheet-like arrangement of micellar chains due to self-avoidance, which in turn lead to planar sheets of NP-aggregates. Apriori, this was an unexpected result for us. This and the other morphologies obtained are examples of the production of nanostructures via synergistic interactions of the equilibrium polymeric matrix and the NPs. The value of the volume fraction of NPs for the transformation from network-like morphology to non-percolating clusters of NPs is approximately identified as ≈ 0.08. We summarize the different kinetically arrested morphologies obtained in a (non-equilibrium) phase diagram with the effective volume fraction of EPs and the volume fraction of NPs on the two axes. There have been experimental studies (Helgeson et al., 2010) which explore the fundamental aspects of the wormlike micelle and NP interactions, where they see "double network" of micelles and NPs. But there the underlying interactions are expected to be different, with chains getting attached to NPs to form a network of micelles. We have purely repulsive interaction between chains and NPs.

Understanding the underlying physical mechanism and energetics of the different morphologies obtained due to synergistic interactions between self-assembling polymers and attractive NPs is expected to help the experimental scientist fine-tune the relevant parameters to control the yield of different porous nanostructures with the required surface area and porosity. The Figs.4.24(a) and (b) can be used as a guide

to chose a suitable volume fractions of wormlike micelles and nanoparticles in order to obtain the desired morphology. It should be noted that the non-percolating clusters are obtained only when the nanoparticle volume fraction is less than 0.08. Moreover, the desired shape of the non-percolating NP clusters can be obtained by a suitable choice of micellar volume fraction. It is clear from the plot that the shape anisotropy of the NP clusters is governed by the micellar volume fraction. The micellar volume fraction also governs the shape anisotropy of the NP clusters in case of percolating networks. Thus, affecting the pore shape and pore size of the network. However, the pore size can also be tuned by changing NP volume fraction. Therefore, a suitable choice of the volume fraction of wormlike micelles and NPs gives rise to the desired morphology.

The micelles can be dissolved away once the NPs aggregate and self-organize to suitable morphology. This might have significant relevance, for example, in the design of batteries materials and super-capacitors, where one needs to balance between large surface area (to increase charge storage) as well as large pores to enable quick dynamics of ions during the charging and discharging process, which affects power density. On the other hand, the NPs could also be possibly dissolved away after the self-assembled polymers are made into gels by addition of suitable additives to enable the experimentalist to obtain polymeric sponges as has been demonstrated using ice-templating techniques (Biswas, Choudhury, and Kumaraswamy, 2016; Chatterjee et al., 2017). We expect the EP-NP morphologies to be kinetically arrested phase separating states, except when the value of $\sigma_{4n} = 1.25\sigma$ when we get a thermodynamically stable mixed state. We use grand-canonical Monte Carlo scheme to introduce (and remove) NPs at randomly chosen positions in the box, this might seem difficult to realize experimentally in a relatively dense polymeric matrix. However, one could possibly have a background solution in which the monomers self-assemble to form equilibrium polymers, and then appropriately chemical reagents could be added to initiate nucleation of nanoparticles out of the solution which would then aggregate and self-organize into the suitable morphologies depending on the synergistic interactions with the background polymeric matrix.

We also would like to increase the scope of this work to investigate the effect of change of nanoparticle interaction, their size and shear.

Bibliography

AA Soler-Illia, Galo J de et al. (2003). "Block copolymer-templated mesoporous oxides". In: *Current Opinion in Colloid & Interface Science* 8.1, pp. 109–126.

Abyaneh, Majid K, Pietro Parisse, and Loredana Casalis (2016). "Direct formation of gold nanorods on surfaces using polymer-immobilised gold seeds". In: *Beilstein journal of nanotechnology* 7, p. 809.

Affdl, JC and JL Kardos (1976). "The Halpin-Tsai equations: a review". In: *Polymer Engineering & Science* 16.5, pp. 344–352.

Alam, M, AM Siddiqui, M Husain, et al. (2013). "Synthesis, characterization and properties of Se nanowires intercalated polyaniline/Se nanocomposites." In: *Express Polymer Letters* 7.9, pp. 723–732.

Alder, Berni Julian and Thomas Everett Wainwright (1957). "Phase transition for a hard sphere system". In: *The Journal of chemical physics* 27.5, pp. 1208–1209.

Ambrosetti, Gianluca (2010). *On the insulator-conductor transition in polymer nanocomposites*. EPFL.

Anderson, Valerie J and Henk NW Lekkerkerker (2002). "Insights into phase transition kinetics from colloid science". In: *Nature* 416.6883, pp. 811–815.

Aniansson, EA G_ and SN Wall (1975). "Kinetics of step-wise micelle association. Correction and improvement". In: *The Journal of Physical Chemistry* 79.8, pp. 857–858.

Aniansson, EAG and S N_ Wall (1974). "Kinetics of step-wise micelle association". In: *The Journal of Physical Chemistry* 78.10, pp. 1024–1030.

Araki, Takeaki and Hajime Tanaka (2006). "Colloidal aggregation in a nematic liquid crystal: topological arrest of particles by a single-stroke disclination line". In: *Physical review letters* 97.12, p. 127801.

Arora, Amit and GW Padua (2010). "Nanocomposites in food packaging". In: *Journal of Food Science* 75.1.

Arraudeau, J.P., J. Patraud, and L.L. Gall (1989). *Composition based on cationic polymers, anionic polymers and waxes for use in cosmetics*. US Patent 4,871,536. URL: https://www.google.com/patents/US4871536.

Asakura, Sho and Fumio Oosawa (1954). "On interaction between two bodies immersed in a solution of macromolecules". In: *The Journal of Chemical Physics* 22.7, pp. 1255–1256.

Bartlett, Paul (1998). "Soft matter in the real world". In: *Physics World* 11.6, p. 23. URL: http://stacks.iop.org/2058-7058/11/i=6/a=23.

Baxter, R J (1968a). "Percus–Yevick Equation for Hard Spheres with Surface Adhesion". In: *The Journal of Chemical Physics* 49.6, pp. 2770–2774. DOI: 10.1063/1.1670482. URL: http://dx.doi.org/10.1063/1.1670482.

Baxter, RJ (1968b). "Ornstein-Zernike relation for a disordered fluid". In: *Australian Journal of Physics* 21.5, pp. 563–570.

Bedrov, Dmitry, Grant D Smith, and Liwei Li (2005). "Molecular dynamics simulation study of the role of evenly spaced poly (ethylene oxide) tethers on the aggregation of C60 fullerenes in water". In: *Langmuir* 21.12, pp. 5251–5255.

Berret, J.-F. (2004). "Rheology of Wormlike Micelles : Equilibrium Properties and Shear Banding Transition". In: *eprint arXiv:cond-mat/0406681*. eprint: cond-mat/0406681.

Berret, Jean-François (2006a). "Rheology of wormlike micelles: equilibrium properties and shear banding transitions". In: *Molecular gels*. Springer, pp. 667–720.

— (2006b). "Rheology of wormlike micelles: equilibrium properties and shear banding transitions". In: *Molecular gels*. Springer, pp. 667–720.

Bianchi, Emanuela, Ronald Blaak, and Christos N. Likos (2011). "Patchy colloids: state of the art and perspectives". In: *Physical Chemistry Chemical Physics* 13.14, p. 6397. ISSN: 1463-9076. DOI: 10.1039/c0cp02296a. URL: http://xlink.rsc.org/?DOI=c0cp02296a.

Binder, K et al. (2008). "Phase transitions of single polymer chains and of polymer solutions: insights from Monte Carlo simulations". In: *Journal of Physics: Condensed Matter* 20.49, p. 494215. URL: http://stacks.iop.org/0953-8984/20/i=49/a=494215.

Binder, Kurt, Peter Virnau, and Antonia Statt (2014). "Perspective: The Asakura Oosawa model: A colloid prototype for bulk and interfacial phase behavior". In: *The Journal of chemical physics* 141.14, p. 559.

Binder, Kurt et al. (1993). "Monte Carlo simulation in statistical physics". In: *Computers in Physics* 7.2, pp. 156–157.

Bird, R. Byron (2004). *Five Decades of Transport Phenomena*. DOI: 10.1002/aic.10026.

Biswas, B., C. K. Choudhury, and G. Kumaraswamy (2016). "Colloidal assembly through ice-templating". In: *Faraday Discussions* 186, pp. 61–76.

Black, CT et al. (2006). "Highly porous silicon membrane fabrication using polymer self-assembly". In: *Journal of Vacuum Science & Technology B: Microelectronics and Nanometer Structures Processing, Measurement, and Phenomena* 24.6, pp. 3188–3191.

Bloemer, Mark J and Michael Scalora (1998). "Transmissive properties of Ag/MgF 2 photonic band gaps". In: *Applied Physics Letters* 72.14, pp. 1676–1678.

Bolhuis, Peter and Daan Frenkel (1994). "Numerical study of the phase diagram of a mixture of spherical and rodlike colloids". In: *The Journal of Chemical Physics* 101.11, pp. 9869–9875. ISSN: 0021-9606. DOI: 10.1063/1.467953. URL: http://aip.scitation.org/doi/10.1063/1.467953.

Bolhuis, Peter G, Evert Jan Meijer, and Ard A Louis (2003). "Colloid-polymer mixtures in the protein limit". In: *Physical review letters* 90.6, p. 068304.

Bolhuis, PG, AA Louis, and JP Hansen (2002). "Influence of polymer-excluded volume on the phase-behavior of colloid-polymer mixtures". In: *Physical review letters* 89.12, p. 128302.

Brader, Joseph M (2010). "Nonlinear rheology of colloidal dispersions". In: *Journal of Physics: Condensed Matter* 22.36, p. 363101.

Bruinink, Christiaan M et al. (2006). "Capillary force lithography: fabrication of functional polymer templates as versatile tools for nanolithography". In: *Advanced Functional Materials* 16.12, pp. 1555–1565.

Camargo, Pedro Henrique Cury, Kestur Gundappa Satyanarayana, and Fernando Wypych (2009). "Nanocomposites: synthesis, structure, properties and new application opportunities". In: *Materials Research* 12, pp. 1–39. ISSN: 1516-1439. URL: http://www.scielo.br/scielo.php?script=sci{_}arttext{\&}pid=S1516-14392009000100002{\&}nrm=iso.

Cao, Guozhong and Ying Wang (2004). *Nanostructures and nanomaterials: synthesis, properties, and applications*. World Scientific.

Carolan, D et al. (2017). "Toughened carbon fibre-reinforced polymer composites with nanoparticle-modified epoxy matrices". In: *Journal of Materials Science* 52.3, pp. 1767–1788.

Carotenuto, G and L Nicolais (2004). "Synthesis and characterization of goldbased mesoscopic additives for polymers". In: *Polymer International* 53.12, pp. 2009–2014. DOI: 10.1002/pi.1616. eprint: https://onlinelibrary.wiley.com/doi/pdf/10.1002/pi.1616. URL: https://onlinelibrary.wiley.com/doi/abs/10.1002/pi.1616.

Cates, ME (1990). "Nonlinear viscoelasticity of wormlike micelles (and other reversibly breakable polymers)". In: *Journal of Physical Chemistry* 94.1, pp. 371–375.

— (1996). "Flow behaviour of entangled surfactant micelles". In: *Journal of Physics: Condensed Matter* 8.47, p. 9167.

Cates, ME and SJ Candau (1990a). "Statics and dynamics of worm-like surfactant micelles". In: *Journal of Physics: Condensed Matter* 2.33, p. 6869.

— (1990b). "Statics and dynamics of worm-like surfactant micelles". In: *Journal of Physics: Condensed Matter* 2.33, p. 6869.

Chandran, Sivasurender et al. (2014). "Confinement enhances dispersion in nanoparticle–polymer blend films". In: *Nature Communications* 5. ISSN: 2041-1723. DOI: 10.1038/ncomms4697. URL: http://www.nature.com/doifinder/10.1038/ncomms4697.

Charleux, Bernadette et al. (2012). "Polymerization-induced self-assembly: from soluble macromolecules to block copolymer nano-objects in one step". In: *Macromolecules* 45.17, pp. 6753–6765.

Chatterjee, S. et al. (2017). "Capillary Uptake in Macroporous Compressible Sponges". In: *Soft Matter* 13, pp. 5731–5740.

Chatterji, A and R Pandit (2001a). "Semiflexible equilibrium polymers: A self-assembling molecular model". In: *EPL (Europhysics Letters)* 54.2, p. 213.

— (2001b). "Semiflexible equilibrium polymers: A self-assembling molecular model". In: *EPL (Europhysics Letters)* 54.2, p. 213.

Chatterji, Apratim and Rahul Pandit (2001c). "Semiflexible Equilibrium Polymers: A Self Assembling Molecular Model". In: *Europhysics Letters* 54.2, pp. 213–219.

— (2003). "The statistical mechanics of semiflexible equilibrium polymers". In: *Journal of Statistical Physics* 110.3, pp. 1219–1248.

Chervanyov, A. I. and G. Heinrich (2009). "Potential theory of the depletion interaction in the colloid-polymer mixtures". In: *Journal of Chemical Physics* 131.23. ISSN: 00219606. DOI: 10.1063/1.3273416.

Choi, Jinsub et al. (2007). "Controlled self-assembly of nanoporous alumina for the self-templating synthesis of polyaniline nanowires". In: *Electrochemistry Communications* 9.5, pp. 971–975. ISSN: 13882481. DOI: 10.1016/j.elecom.2006.11.038.

Coleman, Jonathan N. et al. (2006). *Small but strong: A review of the mechanical properties of carbon nanotube-polymer composites*. DOI: 10.1016/j.carbon.2006.02.038. arXiv: 0306026 [cond-mat].

Corcorran, Shelly, Robert Y. Lochhead, and Tonya McKay (2004). "Particle-Stabilized Emulsions: A Brief Overview". In: *Cosmetics and Toiletries* 119.8, pp. 47–52. URL: http://www.cosmeticsandtoiletries.com/research/chemistry/2113192.html.

Corrin, ML (1948). "Interpretation of X-Ray Scattering from Solutions of Long-Chain Electrolytes on the Basis of a Spherical Micelle". In: *The Journal of Chemical Physics* 16.8, pp. 844–845.

Curk, Tine et al. (2014). "Nanoparticle organization in sandwiched polymer brushes". In: *Nano letters* 14.5, pp. 2617–2622.

Danino, Dganit (2012). "Cryo-TEM of soft molecular assemblies". In: *Current opinion in colloid & interface science* 17.6, pp. 316–329.

Das, Tapan K and Smita Prusty (2012). "Review on conducting polymers and their applications". In: *Polymer-Plastics Technology and Engineering* 51.14, pp. 1487–1500.

De Azeredo, Henriette MC (2009). "Nanocomposites for food packaging applications". In: *Food Research International* 42.9, pp. 1240–1253.

De Gennes, PG (1987). "Polymers at an interface; a simplified view". In: *Advances in Colloid and Interface Science* 27.3-4, pp. 189–209.

De Gennes, Pierre-Gilles and Thomas A Witten (1980). *Scaling concepts in polymer physics*.

De Hek, H and A Vrij (1981). "Interactions in mixtures of colloidal silica spheres and polystyrene molecules in cyclohexane: I. Phase separations". In: *Journal of Colloid and Interface Science* 84.2, pp. 409–422.

Debye, P (1948). "Note on light scattering in soap solutions". In: *Journal of colloid science* 3.4, pp. 407–409.

Debye, P and EW Anacker (1951). "Micelle shape from dissymmetry measurements." In: *The Journal of Physical Chemistry* 55.5, pp. 644–655.

Derjaguin, BV (1941). "Theory of the stability of strongly charged lyophobic sols and the adhesion of strongly charged particles in solutions of electrolytes". In: *Acta Physicochim. USSR* 14, pp. 633–662.

Dijkstra, Marjolein, Joseph M Brader, and Robert Evans (1999). "Phase behaviour and structure of model colloid-polymer mixtures". In: *Journal of Physics: Condensed Matter* 11.50, p. 10079.

Dijkstra, Marjolein et al. (2006). "Effect of many-body interactions on the bulk and interfacial phase behavior of a model colloid-polymer mixture". In: *Physical Review E - Statistical, Nonlinear, and Soft Matter Physics* 73.4. ISSN: 15393755. DOI: 10.1103/PhysRevE.73.041404.

Dreiss, Cecile A (2017). "Chapter 1 Wormlike Micelles: An Introduction". In: *Wormlike Micelles: Advances in Systems{,} Characterisation and Applications*. The Royal Society of Chemistry, pp. 1–8. ISBN: 978-1-78262-516-2. DOI: 10.1039/9781782629788-00001. URL: http://dx.doi.org/10.1039/9781782629788-00001.

Dufton, Peter W (1998). *Functional Additives for the Plastics Industry: Trends in Use*. iSmithers Rapra Publishing.

Duleba, Branislav, Emil Spišák, and František Greškovič (2014). "Mechanical properties of PA6/MMT polymer nanocomposites and prediction based on content of nanofiller". In: *Procedia Engineering* 96, pp. 75–80.

Dvorak, GEORGE J (1991). "Plasticity theories for fibrous composite materials". In: *Metal Matrix Composites: Mechanisms and Properties* 2, p. 1.

Dwivedi, Poushpi, Shahid S Narvi, and Ravi P Tewari (2013). "Application of polymer nanocomposites in the nanomedicine landscape: envisaging strategies to combat implant associated infections". In: *Journal of Applied Biomaterials & Functional Materials* 11.3, pp. 129–142.

Edwards, John et al. (1984). "Phase separation in model colloidal dispersions". In: *Journal of the Chemical Society, Faraday Transactions 1: Physical Chemistry in Condensed Phases* 80.9, pp. 2599–2607.

Edwards, Sam F et al. (1986). *The theory of polymer dynamics*. Oxford Univ. Press.

Edwards, SF (1966). "The theory of polymer solutions at intermediate concentration". In: *Proceedings of the Physical Society* 88.2, p. 265.

Elboujdaini, Mimoun et al. (2000). "Stress corrosion crack initiation processes: pitting and microcrack coalescence". In: *CORROSION 2000*. NACE International.

Escobedo, Fernando A. (2014). "Engineering entropy in soft matter: the bad, the ugly and the good". In: *Soft Matter* 10 (42), pp. 8388–8400. DOI: 10.1039/C4SM01646G. URL: http://dx.doi.org/10.1039/C4SM01646G.

Fåhraeus, Robin (1929). "The suspension stability of the blood". In: *Physiological Reviews* 9.2, pp. 241–274.

Fejer, Szilard N and David J Wales (2007). "Helix self-assembly from anisotropic molecules". In: *Physical Review Letters* 99.8, p. 086106.

Feldman, Dorel (2008). "Polymer History". In: *Designed Monomers & Polymers* 11.1, pp. 1–15. ISSN: 1385772X. DOI: 10.1163/156855508X292383. URL: http://www.tandfonline.com/doi/full/10.1163/156855508X292383.

Fenniri, H. et al. (2002). "Entropically driven self-assembly of multichannel rosette nanotubes". In: *Proceedings of the National Academy of Sciences* 99.Supplement 2, pp. 6487–6492. ISSN: 0027-8424. DOI: 10.1073/pnas.032527099. URL: http://www.pnas.org/cgi/doi/10.1073/pnas.032527099.

Findenegg, GH (1986). "JN Israelachvili: Intermolecular and Surface Forces (With Applications to Colloidal and Biological Systems). Academic Press, London, Orlando, San Diego, New York, Toronto, Montreal, Sydney, Tokyo 1985. 296 Seiten, Preis: 65.00.". In: *Berichte der Bunsengesellschaft für physikalische Chemie* 90.12, pp. 1241–1242.

Frenkel, Daan and David J Wales (2011). "Colloidal self-assembly: designed to yield". In: *Nature materials* 10.6, p. 410.

Fukuda, Jun-ichi, Slobodan Žumer, et al. (2009). "Confinement effect on the interaction between colloidal particles in a nematic liquid crystal: An analytical study". In: *Physical Review E* 79.4, p. 041703.

Gadberry, James F, Michael Hoey, and Clois E Powell (1997). *Organoclay compositions*. US Patent 5,663,111.

Ganesan, Venkat, Christopher J Ellison, and Victor Pryamitsyn (2010). "Mean-field models of structure and dispersion of polymer-nanoparticle mixtures". In: *Soft Matter* 6.17, pp. 4010–4025.

Gast, Alice P, Carol K Hall, and William B Russel (1983a). "Phase separations induced in aqueous colloidal suspensions by dissolved polymer". In: *Faraday Discussions of the Chemical Society* 76, pp. 189–201.

Gast, AP, CK Hall, and WB Russel (1983b). "Polymer-induced phase separations in nonaqueous colloidal suspensions". In: *Journal of Colloid and Interface Science* 96.1, pp. 251–267.

— (1983c). "Polymer-induced phase separations in nonaqueous colloidal suspensions". In: *Journal of Colloid and Interface Science* 96.1, pp. 251–267.

Gast, AP, WB Russel, and CK Hall (1986). "An experimental and theoretical study of phase transitions in the polystyrene latex and hydroxyethylcellulose system". In: *Journal of colloid and interface science* 109.1, pp. 161–171.

Gence, L et al. (2010). "Conjugated polymer and hybrid polymer-metal single nanowires: correlated characterization and device integration". In: *Nanowires Science and Technology*. InTech.

Germann, Natalie et al. (2016). "Validation of constitutive modeling of shear banding, threadlike wormlike micellar fluids". In: *Journal of Rheology* 60.5, pp. 983–999.

Gharbi, Mohamed Amine, Maurizio Nobili, and Christophe Blanc (2014). "Use of topological defects as templates to direct assembly of colloidal particles at nematic interfaces". In: *Journal of colloid and interface science* 417, pp. 250–255.

Glotzer, Sharon C and Michael J Solomon (2007). "Anisotropy of building blocks and their assembly into complex structures". In: *Nature Materials* 6.8, pp. 557–562.

Goetz, Rüdiger and Reinhard Lipowsky (1998). "Computer simulations of bilayer membranes: self-assembly and interfacial tension". In: *The Journal of chemical physics* 108.17, pp. 7397–7409.

Gonzalez, I, JI Eguiazabal, and J Nazabal (2006). "Nanocomposites based on a polyamide 6/maleated styrene–butylene-co-ethylene–styrene blend: Effects of clay loading on morphology and mechanical properties". In: *European Polymer Journal* 42.11, pp. 2905–2913.

Goodwin, Jim W (2004). "The Nature of Colloids". In: *Colloids and Interfaces with Surfactants and Polymers – An Introduction*, pp. 1–26. ISBN: 9780470093917. DOI: 10.1002/0470093919.ch1. URL: http://dx.doi.org/10.1002/0470093919.ch1.

Gouy, GL (1913). "J. de Phys. 9, 457 (1910); DL Chapman". In: *Phil. Mag* 25, p. 475.

Graham, Carl and Denis Talay (2013). "Strong Law of Large Numbers and Monte Carlo Methods". In: *Stochastic Simulation and Monte Carlo Methods: Mathematical Foundations of Stochastic Simulation*. Berlin, Heidelberg: Springer Berlin Heidelberg, pp. 13–35. ISBN: 978-3-642-39363-1. DOI: 10.1007/978-3-642-39363-1_2. URL: http://dx.doi.org/10.1007/978-3-642-39363-1_2.

Grzelczak, Marek et al. (2010a). "Directed self-assembly of nanoparticles". In: *ACS nano* 4.7, pp. 3591–3605.

— (2010b). "Directed self-assembly of nanoparticles". In: *ACS nano* 4.7, pp. 3591–3605.

Guareschi, Icilio (1911). "Francesco Selmi and Colloidal Solutions". In: *Chemiker-Zeitung* 34, pp. 1189–1190.

Guarini, KW et al. (2002). "Process integration of self-assembled polymer templates into silicon nanofabrication". In: *Journal of Vacuum Science & Technology B: Microelectronics and Nanometer Structures Processing, Measurement, and Phenomena* 20.6, pp. 2788–2792.

Guo, Qingchuan et al. (2014). "Comparison of in situ and ex situ methods for synthesis of two-photon polymerization polymer nanocomposites". In: *Polymers* 6.7, pp. 2037–2050.

Gupta, Vinod Kumar N, Anurag Mehra, and Rochish Thaokar (2012). "Worm-like micelles as templates: formation of anisotropic silver halide nanoparticles". In: *Colloids and Surfaces A: Physicochemical and Engineering Aspects* 393, pp. 73–80.

Haile, JM (1992). *Molecular dynamics simulation*. Vol. 18. Wiley, New York.

Halsey Jr, GD (1953). "On the structure of micelles". In: *The Journal of Physical Chemistry* 57.1, pp. 87–89.

Hamaker, HC (1937). "The London—van der Waals attraction between spherical particles". In: *physica* 4.10, pp. 1058–1072.

Harkins, William D, Earl CH Davies, and George L Clark (1917). "The orientation of molecules in the surfaces of liquids, the energy relations at surfaces, solubility, adsorption, emulsification, molecular association, and the effect of acids and bases on interfacial tension. 1 (surface energy vi.)" In: *Journal of the American Chemical Society* 39.4, pp. 541–596.

Hartley, GS (1949). "Organised Structure in Soap Solutions". In: *Nature* 163.4150, p. 767.

Hartley, GS and DF Runnicles (1938). "The determination of the size of paraffin-chain salt micelles from diffusion measurements". In: *Proceedings of the Royal Society of London. Series A. Mathematical and Physical Sciences* 168.934, pp. 420–440.

Haryono, Agus and Wolfgang H Binder (2006). "Controlled Arrangement of Nanoparticle Arrays in Block-Copolymer Domains". In: *Small* 2.5, pp. 600–611.

Hastings, W Keith (1970). "Monte Carlo sampling methods using Markov chains and their applications". In: *Biometrika* 57.1, pp. 97–109.

He, Chaobin et al. (2008). "Microdeformation and fracture mechanisms in polyamide-6/organoclay nanocomposites". In: *Macromolecules* 41.1, pp. 193–202.

Hegmann, Torsten, Hao Qi, and Vanessa M Marx (2007). "Nanoparticles in liquid crystals: synthesis, self-assembly, defect formation and potential applications". In: *Journal of Inorganic and Organometallic Polymers and Materials* 17.3, pp. 483–508.

Helgeson, M. E. et al. (2010). "Formation and Rheology of Viscoelastic "Double Networks" in Wormlike MicelleNanoparticle Mixtures". In: *Langmuir* 26.11, pp. 8049–8060.

Helmholtz, H von (1853). "Ueber einige Gesetze der Vertheilung elektrischer Ströme in körperlichen Leitern mit Anwendung auf die thierisch-elektrischen Versuche". In: *Annalen der Physik* 165.6, pp. 211–233.

Higuera, FJ and J Jimenez (1989). "Boltzmann approach to lattice gas simulations". In: *EPL (Europhysics Letters)* 9.7, p. 663.

Hobbs, Marcus E (1951). "The effect of salts on the critical concentration, size, and stability of soap micelles." In: *The Journal of Physical Chemistry* 55.5, pp. 675–683.

Hoeve, CAJ and GC Benson (1957). "On the statistical mechanical theory of micelle formation in detergent solutions". In: *The Journal of Physical Chemistry* 61.9, pp. 1149–1158.

Hoover, William G and Francis H Ree (1968). "Melting transition and communal entropy for hard spheres". In: *The Journal of Chemical Physics* 49.8, pp. 3609–3617.

Horsch, Mark A, Zhenli Zhang, and Sharon C Glotzer (2005). "Self-assembly of polymer-tethered nanorods". In: *Physical review letters* 95.5, p. 056105.

Hosler, Dorothy, Sandra L Burkett, and Michael J Tarkanian (1999). "Prehistoric Polymers: Rubber Processing in Ancient Mesoamerica". In: *Science* 284.5422, pp. 1988–1991. ISSN: 0036-8075. DOI: 10.1126/science.284.5422.1988. URL: http://science.sciencemag.org/content/284/5422/1988.

Huang, C-C, J-P Ryckaert, and H Xu (2009). "Structure and dynamics of cylindrical micelles at equilibrium and under shear flow". In: *Physical Review E* 79.4, p. 041501.

Ikkala, Olli and Gerrit ten Brinke (2004). "Hierarchical self-assembly in polymeric complexes: Towards functional materials". In: *Chemical Communications* 19, p. 2131. ISSN: 1359-7345. DOI: 10.1039/b403983a. URL: http://xlink.rsc.org/?DOI=b403983a.

Ilett, Steve M et al. (1995). "Phase behavior of a model colloid-polymer mixture". In: *Physical Review E* 51.2, p. 1344.

Ingrosso, Chiara et al. (2010). "Colloidal inorganic nanocrystal based nanocomposites: functional materials for micro and nanofabrication". In: *Materials* 3.2, pp. 1316–1352.

Israelachvili, Jacob N, D John Mitchell, and Barry W Ninham (1976). "Theory of self-assembly of hydrocarbon amphiphiles into micelles and bilayers". In: *Journal of the Chemical Society, Faraday Transactions 2: Molecular and Chemical Physics* 72, pp. 1525–1568.

Jain, Sumeet and Frank S Bates (2003). "On the origins of morphological complexity in block copolymer surfactants". In: *Science* 300.5618, pp. 460–464.

Jakšić, Zoran, Milan Maksimović, and Milija Sarajlić (2004). "Silver–silica transparent metal structures as bandpass filters for the ultraviolet range". In: *Journal of Optics A: Pure and Applied Optics* 7.1, p. 51.

Jayalakshmi, Yalia and Eric W. Kaler (1997). "Phase Behavior of Colloids in Binary Liquid Mixtures". In: *Physical Review Letters* 78.7, pp. 1379–1382. ISSN: 0031-9007. DOI: 10.1103/PhysRevLett.78.1379. URL: http://link.aps.org/doi/10.1103/PhysRevLett.78.1379.

Jayaraman, Arthi and Kenneth S Schweizer (2009). "Effective interactions and self-assembly of hybrid polymer grafted nanoparticles in a homopolymer matrix". In: *Macromolecules* 42.21, pp. 8423–8434.

Kashiwagi, Takashi et al. (2007). "Relationship between dispersion metric and properties of PMMA/SWNT nanocomposites". In: *Polymer* 48.16, pp. 4855–4866. ISSN: 00323861. DOI: 10.1016/j.polymer.2007.06.015.

Katz, Linda M. (2007). "Nanotechnology and Applications in Cosmetics: General Overview". In: *Cosmetic Nanotechnology*. ACS Publications. Chap. 11, pp. 193–200. DOI: 10.1021/bk-2007-0961.ch011. eprint: https://pubs.acs.org/doi/pdf/10.1021/bk-2007-0961.ch011. URL: https://pubs.acs.org/doi/abs/10.1021/bk-2007-0961.ch011.

Kedawat, Garima et al. (2014). "Fabrication of a flexible UV band-pass filter using surface plasmon metal–polymer nanocomposite films for promising laser applications". In: *ACS Applied Materials & Interfaces* 6.11, pp. 8407–8414.

Khokhlov, AR and AN Semenov (1981). "Liquid-crystalline ordering in the solution of long persistent chains". In: *Physica A: Statistical Mechanics and its Applications* 108.2-3, pp. 546–556.

Kim, G-M and GH Michler (1998). "Micromechanical deformation processes in toughened and particle filled semicrystalline polymers: Part 2. model representation for micromechanical deformation processes". In: *Polymer* 39.23, pp. 5699–5703.

Kim, YongJoo and Alfredo Alexander-Katz (2011). "Phase behavior of symmetric disk-coil macromolecules with stacking interactions". In: *The Journal of chemical physics* 135.2, p. 024902.

Klevens, HB (1948). "Critical micelle concentrations as determined by refraction". In: *The Journal of Physical Chemistry* 52.1, pp. 130–148.

— (1953). "Structure and aggregation in dilate solution of surface active agents". In: *Journal of the American Oil Chemists' Society* 30.2, pp. 74–80.

Kline, Steven R and Eric W Kaler (1996). "Aggregation of Colloidal Silica by n-Alkyl Sulfates". In: *Langmuir* 12.10, pp. 2402–2407. DOI: 10.1021/la9507161. URL: http://dx.doi.org/10.1021/la9507161.

Kooij, F. M. van der, M. Vogel, and H. N W Lekkerkerker (2000). "Phase behavior of a mixture of platelike colloids and nonadsorbing polymer". In: *Physical Review E - Statistical Physics, Plasmas, Fluids, and Related Interdisciplinary Topics* 62.4, pp. 5397–5402. ISSN: 1063651X. DOI: 10.1103/PhysRevE.62.5397.

Kresge, CT et al. (1992). "Ordered mesoporous molecular sieves synthesized by a liquid-crystal template mechanism". In: *Nature* 359.6397, p. 710.

Kröger, M and R Makhloufi (1996). "Wormlike micelles under shear flow: a microscopic model studied by nonequilibrium-molecular-dynamics computer simulations". In: *Physical Review E* 53.3, p. 2531.

Kumaraswamy, Guruswamy and Kamendra P Sharma (2013). "Polymer and Colloidal Inclusions in Lyotropic Lamellar and Hexagonal Surfactant Mesophases". In: *Advances in Planar Lipid Bilayers and Liposomes*. Vol. 18. Elsevier, pp. 181–208.

Kwolek, Stephanie, Hiroshi Mera, and Tadahiko Takata (2002). "High-performance fibres". In: *Ullmann's encyclopedia of industrial chemistry. Weinheim: Wiley-VCH*.

Lajovic A. Tomšič, M. and A. Jamnik (2009). "Depletion effects in a mixture of hard and attractive colloids". In: *Journal of Chemical Physics* 130.10. ISSN: 00219606. DOI: 10.1063/1.3081144.

Lalander, Cecilia H. et al. (2010). "DNA-directed self-assembly of gold nanoparticles onto nanopatterned surfaces: Controlled placement of individual nanoparticles into regular arrays". In: *ACS Nano* 4.10, pp. 6153–6161. ISSN: 19360851. DOI: 10.1021/nn101431k.

Langmuir, Blodget K.B. (1935). In: *Kolloid Zeitschrift* 73, pp. 257–263.

Lao, Chang Shi et al. (2006). "Formation of double-side teethed nanocombs of ZnO and self-catalysis of Zn-terminated polar surface". In: *Chemical physics letters* 417.4, pp. 358–362.

Laufer, A and S Dikstein (1996). "Objective measurement and self-assessment of skin-care treatments". In: *Cosmetics and toiletries* 111.6, pp. 91–98.

Lee, Hyuk-soo et al. (2005). "TPO based nanocomposites. Part 1. Morphology and mechanical properties". In: *Polymer* 46.25, pp. 11673–11689.

Lee, Jae-Youn et al. (2002). "Entropically Driven Formation of Hierarchically Ordered Nanocomposites". In: *Phys. Rev. Lett.* 89 (15), p. 155503. DOI: 10.1103/PhysRevLett.89.155503. URL: https://link.aps.org/doi/10.1103/PhysRevLett.89.155503.

Lee, Jae Youn et al. (2004). "Self-Assembly of Amphiphilic Nanoparticle- Coil "Tadpole" Macromolecules". In: *Macromolecules* 37.10, pp. 3536–3539.

Lekkerkerker, H. N. W et al. (1992a). "Phase Behaviour of Colloid + Polymer Mixtures". In: *Europhysics Letters (EPL)* 20.6, pp. 559–564. ISSN: 0295-5075. DOI: 10.1209/0295-5075/20/6/015. URL: http://stacks.iop.org/0295-5075/20/i=6/a=015?key=crossref.edbb40a622f4f72deefe1262f5518c55.

Lekkerkerker, HNW et al. (1992b). "Phase behaviour of colloid+ polymer mixtures". In: *EPL (Europhysics Letters)* 20.6, p. 559.

Leontidis, Epameinondas et al. (2003). "Composite nanotubes formed by self-assembly of PbS nanoparticles". In: *Nano letters* 3.4, pp. 569–572.

Lerouge, S. and J.-F. Berret (2010). "Shear-Induced Transitions and Instabilities in Surfactant Wormlike Micelles". In: *Polymer Characterization, Advances in Polymer Science, Volume 230. ISBN 978-3-642-13531-6. Springer Berlin Heidelberg, 2010, p. 1*. Ed. by K. Dusek and J.-F. Joanny, p. 1. DOI: 10.1007/12_2009_13.

Li, Shanghua et al. (2010). "Nanocomposites of polymer and inorganic nanoparticles for optical and magnetic applications". In: *Nano reviews* 1.1, p. 5214.

Li, Zhan-Wei et al. (2012). "Model, self-assembly structures, and phase diagram of soft Janus particles". In: *Soft Matter* 8.25, pp. 6693–6697.

Liang, Yi-Ling (2008). *The toughening mechanisms in epoxy-silica nanocomposites and hybrid epoxy-silica-rubber nanocomposites*. Lehigh University.

Liedl, Claudia (2011). "Top-down vs. Bottom-up". In: *Centre for European Studies*, pp. 3–94.

Lin, Yao et al. (2005). "Self-directed self-assembly of nanoparticle/copolymer mixtures". In: *Nature* 434.7029, pp. 55–59.

Lionberger, RA and William B. Russel (1999). *Advances in Chemical Physics*. Vol. 111, pp. 399–474. ISBN: 9780470141700. DOI: 10.1002/9780470141700. URL: http://onlinelibrary.wiley.com/doi/10.1002/9780470141700.ch3/summary{\%}0Ahttp://doi.wiley.com/10.1002/9780470141700.

Lochhead, Robert Y. (2007). "The Role of Polymers in Cosmetics: Recent Trends". In: *Cosmetic Nanotechnology*. ACS Publications. Chap. 1, pp. 3–56. DOI: 10.1021/bk-2007-0961.ch001. eprint: https://pubs.acs.org/doi/pdf/10.1021/bk-2007-0961.ch001. URL: https://pubs.acs.org/doi/abs/10.1021/bk-2007-0961.ch001.

Lochhead, Robert Y. (2008). "Skin Care Polymer Trends". In: *HAPPI* 3, p. 08. URL: http://www.happi.com/contents/view_features/2008-03-28/skin-care-polymer-trends/.

Lopes, Ward A and Heinrich M Jaeger (2001). "Hierarchical self-assembly of metal nanostructures on diblock copolymer scaffolds". In: *Nature* 414.6865, p. 735.

LTD., Amir Bahrami-TWI. *Nano Composite Network, Technology Review-Nanocomposite.* https://compositesuk.co.uk/system/files/documents/Nanocomposites.pdf.

Lu, Peter J et al. (2008). "Gelation of particles with short-range attraction". In: *Nature* 453.7194, p. 499.

Luo, Yongming et al. (2006). "Formation of the Si C N nanorod in polymer matrix". In: *Materials Science and Engineering: A* 432.1, pp. 69–70.

Ma, Lin et al. (2005). "Numerical analysis of interaction and coalescence of numerous microcracks". In: *Engineering fracture mechanics* 72.12, pp. 1841–1865.

Mackay, M. E. (2006). "General Strategies for Nanoparticle Dispersion". In: *Science* 311.5768, pp. 1740–1743. ISSN: 0036-8075. DOI: 10.1126/science.1122225. URL: http://www.sciencemag.org/cgi/doi/10.1126/science.1122225.

Maillet, J-B, V Lachet, and Peter V Coveney (1999). "Large scale molecular dynamics simulation of self-assembly processes in short and long chain cationic surfactants". In: *Physical Chemistry Chemical Physics* 1.23, pp. 5277–5290.

Mani, Ethayaraja et al. (2012). "Sheet-like assemblies of spherical particles with point-symmetrical patches". In: *The Journal of chemical physics* 136.14, p. 144706.

Mattoon, RW, RS Stearns, and WD Harkins (1947). "Structure for soap micelles as indicated by a previously unrecognized X-ray diffraction band". In: *The Journal of Chemical Physics* 15.4, pp. 209–210.

Mazumdar, Payal, Sunita Rattan, and Monalisa Mukherjee (2015). "Polymer nanocomposites using click chemistry: novel materials for hydrogen peroxide vapor sensors". In: *RSC Advances* 5.85, pp. 69573–69582.

McBain, JW (1913). "Colloids and their viscosity". In: *Trans Faraday Soc* 9.99, p. 120.

McCoy, Jonathan H et al. (2008). "Self-organization of topological defects due to applied constraints". In: *Physical review letters* 101.25, p. 254102.

Meijer, Evert Jan and Daan Frenkel (1994). "Colloids dispersed in polymer solutions. A computer simulation study". In: *The Journal of chemical physics* 100.9, pp. 6873–6887.

Mezzenga, R. (2003). "Templating Organic Semiconductors via Self-Assembly of Polymer Colloids". In: *Science* 299.5614, pp. 1872–1874. ISSN: 00368075. DOI: 10.1126/science.1081334. URL: http://www.sciencemag.org/cgi/doi/10.1126/science.1081334.

Miller, Georgia (2006). *Nanomaterials, sunscreens and cosmetics: small ingredients big risks*. Friends of the Earth.

Miyashita, Tokuji (2004). "Fabrication of soft nano-devices using polymer nano-sheets". In: *Nettowaku Porima* 25.1, pp. 34–43.

Moreno-Razo, JA et al. (2012). "Liquid-crystal-mediated self-assembly at nanodroplet interfaces". In: *Nature* 485.7396, p. 86.

Mori, Tanaka and K Tanaka (1973). "Average stress in matrix and average elastic energy of materials with misfitting inclusions". In: *Acta metallurgica* 21.5, pp. 571–574.

Mouriño, V. (2016). "8 - Polymer nanocomposites for drug delivery applications in bone tissue regeneration". In: *Nanocomposites for Musculoskeletal Tissue Regeneration*. Ed. by Huinan Liu. Oxford: Woodhead Publishing, pp. 175 –186. ISBN:

978-1-78242-452-9. DOI: https://doi.org/10.1016/B978-1-78242-452-9.00008-X. URL: https://www.sciencedirect.com/science/article/pii/B978178242452900008X.

Muševič, Igor and Miha Škarabot (2008). "Self-assembly of nematic colloids". In: *Soft Matter* 4.2, pp. 195–199.

Nagarajan, R (1982). "Are large micelles rigid or flexible? A reinterpretation of viscosity data for micellar solutions". In: *Journal of Colloid and Interface Science* 90.2, pp. 477–486.

— (1993). "Modelling solution entropy in the theory of micellization". In: *Colloids and Surfaces A: Physicochemical and Engineering Aspects* 71.1, pp. 39–64.

Nagarajan, R and E Ruckenstein (1991). "Theory of surfactant self-assembly: a predictive molecular thermodynamic approach". In: *Langmuir* 7.12, pp. 2934–2969.

Nagel, Sidney R. (2017). "Experimental soft-matter science". In: *Rev. Mod. Phys.* 89 (2), p. 025002. DOI: 10.1103/RevModPhys.89.025002. URL: https://link.aps.org/doi/10.1103/RevModPhys.89.025002.

Naor, Ayal, Sudhakar Puvvada, and Daniel Blankschtein (1992). "An analytical expression for the free energy of micellization". In: *The Journal of Physical Chemistry* 96.19, pp. 7830–7832.

Napper, Donald H (1977). "Steric stabilization". In: *Journal of Colloid and Interface Science* 58.2, pp. 390–407.

OCW, MIT. https://ocw.mit.edu/courses/materials-science-and-engineering/3-063-polymer-physics-spring-2007/lecture-notes/lec3_07.pdf.

Ohayon, David et al. (2001). "Methods for pore size engineering in ZSM-5 zeolite". In: *Applied Catalysis A: General* 217.1-2, pp. 241–251. ISSN: 0926860X. DOI: 10.1016/S0926-860X(01)00611-1.

Ohshima, Hiroyuki, Thomas W Healy, and Lee R White (1982). "Accurate analytic expressions for the surface charge density/surface potential relationship and double-layer potential distribution for a spherical colloidal particle". In: *Journal of Colloid and Interface Science* 90.1, pp. 17–26.

Onsager, L. (1949). "The Effects of Shape on the Interaction of Colloidal Particles". In: *Annals of the New York Academy of Sciences* 51, pp. 627–659. DOI: 10.1111/j.1749-6632.1949.tb27296.x.

Ooshika, Yuzuru (1954). "A theory of critical micelle concentration of colloidal electrolyte solutions". In: *Journal of Colloid Science* 9.3, pp. 254–262.

Opelt, Carlos V and Luiz AF Coelho (2016a). "Reinforcement and toughening mechanisms in polymer nanocomposites–Reinforcement effectiveness and nanoclay nanocomposites". In: *Materials Chemistry and Physics* 169, pp. 179–185.

— (2016b). "Reinforcement and toughening mechanisms in polymer nanocomposites–Reinforcement effectiveness and nanoclay nanocomposites". In: *Materials Chemistry and Physics* 169, pp. 179–185.

Orski, Sara V et al. (2011). "Fabrication of nanostructures using polymer brushes". In: *Journal of Materials Chemistry* 21.37, pp. 14135–14149.

Overbeek, J Th G (1977). "Recent developments in the understanding of colloid stability". In: *Journal of Colloid and Interface Science* 58.2, pp. 408–422.

Ozin, Geoffrey A et al. (2009a). "Nanofabrication by self-assembly". In: *Materials Today* 12.5, pp. 12–23.

— (2009b). "Nanofabrication by self-assembly". In: *Materials Today* 12.5, pp. 12–23.

Palma, Carlos-Andres, Marco Cecchini, and Paolo Samorì (2012). "Predicting self-assembly: from empirism to determinism". In: *Chemical Society Reviews* 41.10, pp. 3713–3730.

Pandey, Rakesh K et al. (2016). "Proton Conductive Nanosheets Formed by Alignment of Metallo-Supramolecular Polymers". In: *ACS Applied Materials & Interfaces* 8.21, pp. 13526–13531.

Park, Sung Ha et al. (2004). "Electronic nanostructures templated on self-assembled DNA scaffolds". In: *Nanotechnology* 15.10, S525.

Park, Sungho, Sung-Wook Chung, and Chad A Mirkin (2004). "Hybrid Organic-Inorganic, Rod-Shaped Nanoresistors and Diodes". In: *Journal of the American Chemical Society* 126.38, pp. 11772–11773.

Parviz, B Amir, Declan Ryan, and George M Whitesides (2003). "Using self-assembly for the fabrication of nano-scale electronic and photonic devices". In: *IEEE transactions on advanced packaging* 26.3, pp. 233–241.

Patel, Hasmukh A et al. (2006). "Nanoclays for polymer nanocomposites, paints, inks, greases and cosmetics formulations, drug delivery vehicle and waste water treatment". In: *Bulletin of Materials Science* 29.2, pp. 133–145.

Patel, Prakash D and William B Russel (1989). "An experimental study of aqueous suspensions containing dissolved polymer: A. Phase separation". In: *Journal of colloid and interface science* 131.1, pp. 192–200.

Peter, Christine and Kurt Kremer (2009). "Multiscale simulation of soft matter systems–from the atomistic to the coarse-grained level and back". In: *Soft Matter* 5.22, pp. 4357–4366.

Pham, Khoa N., Damian Fullston, and Kwesi Sagoe-Crentsil (2007). "Surface charge modification of nano-sized silica colloid". In: *Australian Journal of Chemistry* 60.9, pp. 662–666. ISSN: 00049425. DOI: 10.1071/CH07138.

Philippoff, W (1950). "Micelles and X-rays". In: *Journal of Colloid Science* 5.2, pp. 169–191.

— (1951). "Colloidal and polyelectrolytes. The micelle and swollen micelle on soap micelles". In: *Discussions of the Faraday Society* 11, pp. 96–107.

Piazza, R and G Di Pietro (1994). "Phase separation and gel-like structures in mixtures of colloids and surfactant". In: *EPL (Europhysics Letters)* 28.6, p. 445.

Pitsa, Despoina and Michael G Danikas (2011). "Interfaces features in polymer nanocomposites: A review of proposed models". In: *Nano* 6.06, pp. 497–508.

Pochan, Darrin J et al. (2004). "Toroidal triblock copolymer assemblies". In: *Science* 306.5693, pp. 94–97.

Poon, W. (2004). "PHYSICS: Colloids as Big Atoms". In: *Science* 304.5672, pp. 830–831. ISSN: 0036-8075. DOI: 10.1126/science.1097964. URL: http://www.sciencemag.org/cgi/doi/10.1126/science.1097964.

Poon, W C K (2002). "The physics of a model colloid polymer mixture". In: *Journal of Physics: Condensed Matter* 14.33, R859–R880. ISSN: 0953-8984. DOI: 10.1088/0953-8984/14/33/201. URL: http://stacks.iop.org/0953-8984/14/i=33/a=201?key=crossref.5ef073c28c2f78b6edbd72b000c1701d.

Poon, WCK et al. (1993). "An experimental study of a model colloid-polymer mixture". In: *Journal de Physique II* 3.7, pp. 1075–1086.

Poulin, Philippe et al. (1997). "Novel colloidal interactions in anisotropic fluids". In: *Science* 275.5307, pp. 1770–1773.

Prévost, Sylvain, Michael Gradzielski, and Thomas Zemb (2017). "Self-assembly, phase behaviour and structural behaviour as observed by scattering for classical and non-classical microemulsions". In: *Advances in colloid and interface science* 247, pp. 374–396.

Pryamtisyn, Victor et al. (2009). *Modeling the anisotropic self-assembly of spherical polymer-grafted nanoparticles*.

Pusey, Peter N and W Van Megen (1986). "Phase behaviour of concentrated suspensions of nearly hard colloidal spheres". In: *Nature* 320.6060, p. 340.

Puvvada, Sudhakar and Daniel Blankschtein (1990). "Molecular-thermodynamic approach to predict micellization, phase behavior and phase separation of micellar solutions. I. Application to nonionic surfactants". In: *The Journal of chemical physics* 92.6, pp. 3710–3724.

Qi, Haisong (2017). *Novel Functional Materials Based on Cellulose*. Springer.

Qu, Guangmiao et al. (2010). "Synthesis, Characterization and Surface Properties of Series Sulfobetaine Surfactants". In: *Journal of Surfactants and Detergents* 14.1, pp. 31–35. DOI: 10.1007/s11743-010-1212-9. eprint: https://onlinelibrary.wiley.com/doi/pdf/10.1007/s11743-010-1212-9. URL: https://onlinelibrary.wiley.com/doi/abs/10.1007/s11743-010-1212-9.

Quaresimin, M, M Salviato, and M Zappalorto (2015). "Toughening mechanisms in nanoparticle polymer composites". In: *Toughening Mechanisms in Composite Materials*, p. 113.

Rahedi, Andrew J, Jack F Douglas, and Francis W Starr (2008). "Model for reversible nanoparticle assembly in a polymer matrix". In: *The Journal of chemical physics* 128.2, p. 024902.

Raj, Silpa et al. (2012). "Nanotechnology in cosmetics: Opportunities and challenges". In: *Journal of Pharmacy & Bioallied Sciences* 4.3, p. 186.

Ramos, L et al. (2000). "Light scattering with swollen hexagonal phases". In: *The European Physical Journal E: Soft Matter and Biological Physics* 1.4, pp. 285–299.

Ramos, Laurence et al. (1999). "Surfactant-mediated two-dimensional crystallization of colloidal crystals". In: *Science* 286.5448, pp. 2325–2328.

Ravnik, Miha and Slobodan Žumer (2009). "Nematic colloids entangled by topological defects". In: *Soft Matter* 5.2, pp. 269–274.

Ray, Sudip et al. (2006). "The potential use of polymer-clay nanocomposites in food packaging". In: *International Journal of Food Engineering* 2.4. Retrieved 31 Mar. 2018, from doi:10.2202/1556-3758.1149.

Ray, Suprakas Sinha and Mosto Bousmina (2006). *Polymer nanocomposites and their applications*. American Scientific.

Rhim, Jong-Whan, Hwan-Man Park, and Chang-Sik Ha (2013). "Bio-nanocomposites for food packaging applications". In: *Progress in Polymer Science* 38.10, pp. 1629–1652.

Rozenberg, BA and R Tenne (2008). "Polymer-assisted fabrication of nanoparticles and nanocomposites". In: *Progress in Polymer Science* 33.1, pp. 40–112.

Ruckenstein, E. and Z. F. Li (2005). "Surface modification and functionalization through the self-assembled monolayer and graft polymerization". In: *Advances in Colloid and Interface Science* 113.1, pp. 43–63. ISSN: 00018686. DOI: 10.1016/j.cis.2004.07.009.

Rusanov, AI (2016). "Refining the ionic surfactant micellization theory based on the law of mass action". In: *Colloid Journal* 78.5, pp. 669–673.

Sahabi, Hussein and Matthias Kind (2011). "Experimentally Justified Model-Like Description of Consolidation of Precipitated Silica". In: *Polymers* 3.4, pp. 2156–2171.

Sallen, L et al. (1995). "Surface tension and elasticity of hexagonal columnar mesophases". In: *Journal de Physique II* 5.7, pp. 937–961.

Sambarkar, PP, SL Patwekar, and BM Dudhgaonkar (2012). "Polymer nanocomposites: An overview". In: *International Journal of Pharmacy and Pharmaceutical Sciences* 4.2, pp. 60–65.

Scalora, M et al. (1998). "Transparent, metallo-dielectric, one-dimensional, photonic band-gap structures". In: *Journal of Applied Physics* 83.5, pp. 2377–2383.

Scheraga, Harold A and John K Backus (1951). "Flow Birefringence in Solutions of n-Hexadecyltrimethylammonium Bromide1, 2". In: *Journal of the American Chemical Society* 73.11, pp. 5108–5112.

Schramm, Laurier L (2002). "Colloids". In: *Encyclopedia of Polymer Science and Technology* 9. DOI: 10.1002/0471440264.pst066. URL: http://dx.doi.org/10.1002/0471440264.pst066.

Segala, Karen and Angela S. Pereira (2012). "From Ruthenium Complexes to Novel Functional Nanocomposites: Development and Perspectives". In: *New Polymers for Special Applications*. Ed. by Ailton De Souza Gomes. Rijeka: InTech. Chap. 07. DOI: 10.5772/46244. URL: http://dx.doi.org/10.5772/46244.

Self-Assembled Structures Part 1 (Nanotechnology):webpage. http://what-when-how.com/nanoscience-and-nanotechnology/self-assembled-structures-part-1-nanotechnology/.

Semenov, AN and Alexei Removich Khokhlov (1988). "Statistical physics of liquid-crystalline polymers". In: *Physics-Uspekhi* 31.11, pp. 988–1014.

Senyuk, Bohdan et al. (2013). "Topological colloids". In: *Nature* 493.7431, p. 200.

Seul, Michael and David Andelman (1995). "Domain shapes and patterns: the phenomenology of modulated phases". In: *Science* 267.5197, p. 476.

Sharma, Kamendra P, Vinod K Aswal, and Guruswamy Kumaraswamy (2010). "Adsorption of nonionic surfactant on silica nanoparticles: structure and resultant interparticle interactions". In: *The Journal of Physical Chemistry B* 114.34, pp. 10986–10994.

Sharma, Kamendra P et al. (2009a). "Self-assembly of silica particles in a nonionic surfactant hexagonal mesophase". In: *The Journal of Physical Chemistry B* 113.11, pp. 3423–3430.

— (2009b). "Self-assembly of silica particles in a nonionic surfactant hexagonal mesophase". In: *The Journal of Physical Chemistry B* 113.11, pp. 3423–3430.

Sharma, Kamendra P et al. (2011). "Self-standing three-dimensional networks of nanoparticles with controllable morphology by dynamic templating of surfactant hexagonal domains". In: *Chemistry of Materials* 23.6, pp. 1448–1455.

Sharma, Kamendra P et al. (2013). "Exclusion from hexagonal mesophase surfactant domains drives end-to-end enchainment of rod-like particles". In: *The Journal of Physical Chemistry B* 117.41, pp. 12661–12668.

Shaw, Duncan J (1980). "Introduction to colloid and surface chemistry. 1992". In: *Butterworth-Heinemann, Oxford, ISBN 0* 7506.1182, p. 0.

Shay, Jennifer S, Srinivasa R Raghavan, and Saad A Khan (2001). "Thermoreversible gelation in aqueous dispersions of colloidal particles bearing grafted poly (ethylene oxide) chains". In: *Journal of Rheology* 45.4, pp. 913–927.

Shchukin, Vitaliy A and Dieter Bimberg (1999). "Spontaneous ordering of nanostructures on crystal surfaces". In: *Reviews of Modern Physics* 71.4, p. 1125.

Shenhar, Roy, Tyler B Norsten, and Vincent M Rotello (2005). "Polymer-Mediated Nanoparticle Assembly: Structural Control and Applications". In: *Advanced Materials* 17.6, pp. 657–669.

Shi, Jing et al. (2015). "Recent advances of pore system construction in zeolite-catalyzed chemical industry processes". In: *Chem. Soc. Rev.* 44.24, pp. 8877–8903. ISSN: 0306-0012. DOI: 10.1039/C5CS00626K. URL: http://xlink.rsc.org/?DOI=C5CS00626K.

Singh, Shubra et al. (2010). "Synthesis and Formation Mechanism of ZnO Nanobrushes". In: *AIP Conference Proceedings*. Vol. 1276. AIP, pp. 37–42.

Škarabot, Miha et al. (2008). "Hierarchical self-assembly of nematic colloidal superstructures". In: *Physical Review E* 77.6, p. 061706.

Smith, WR and D Henderson (1970). "Analytical representation of the Percus-Yevick hard-sphere radial distribution function". In: *Molecular Physics* 19.3, pp. 411–415.

Sorrentino, Andrea, Giuliana Gorrasi, and Vittoria Vittoria (2007). "Potential perspectives of bio-nanocomposites for food packaging applications". In: *Trends in Food Science & Technology* 18.2, pp. 84–95.

Sozer, Nesli and Jozef L Kokini (2009). "Nanotechnology and its applications in the food sector". In: *Trends in Biotechnology* 27.2, pp. 82–89.

Spaeth, Justin R, Ioannis G Kevrekidis, and Athanassios Z Panagiotopoulos (2011). "Dissipative particle dynamics simulations of polymer-protected nanoparticle self-assembly". In: *The Journal of chemical physics* 135.18, p. 184903.

Spenley, NA, ME Cates, and TCB McLeish (1993). "Nonlinear rheology of wormlike micelles". In: *Physical review letters* 71.6, p. 939.

Srinivasan, Vibha and Daniel Blankschtein (2005). "Prediction of conformational characteristics and micellar solution properties of fluorocarbon surfactants". In: *Langmuir* 21.4, pp. 1647–1660.

STAHL, G ALLAN. "A Short History of Polymer Science". In: *Polymer Science Overview*. Chap. 3, pp. 25–44. DOI: 10.1021/bk-1981-0175.ch003. URL: http://pubs.acs.org/doi/abs/10.1021/bk-1981-0175.ch003.

— "A Short History of Polymer Science". In: *Polymer Science Overview*. Chap. 3, pp. 25–44. DOI: 10.1021/bk-1981-0175.ch003. URL: http://pubs.acs.org/doi/abs/10.1021/bk-1981-0175.ch003.

Stark, Holger (2001). "Physics of colloidal dispersions in nematic liquid crystals". In: *Physics Reports* 351.6, pp. 387–474.

Starr, Francis W, Jack F Douglas, and Sharon C Glotzer (2003). "Origin of particle clustering in a simulated polymer nanocomposite and its impact on rheology". In: *The Journal of chemical physics* 119.3, pp. 1777–1788.

Stern, O (1924). "Z. Physik 7, 249 (1921); Gerlach W. and Stern O., Z. Physik 8, 110 and 9, 349 (1922)". In: *Ann. Physik* 74, p. 673.

Striccoli, M, ML Curri, and R Comparelli (2009). "Nanocrystal-Based Polymer Composites as Novel Functional Materials". In: *Toward Functional Nanomaterials*. Springer, pp. 173–192.

Sun, HaiZhu and Bai Yang (2008). "In situ preparation of nanoparticles/polymer composites". In: *Science in China Series E: Technological Sciences* 51.11, pp. 1886–1901.

Sun, Shouheng et al. (2002). "Polymer mediated self-assembly of magnetic nanoparticles". In: *Journal of the American Chemical Society* 124.12, pp. 2884–2885.

Tanford, Charles (1972). "Micelle shape and size". In: *The Journal of Physical Chemistry* 76.21, pp. 3020–3024.

— (1974). "Thermodynamics of micelle formation: prediction of micelle size and size distribution". In: *Proceedings of the National Academy of Sciences* 71.5, pp. 1811–1815.

— (1978). "The hydrophobic effect and the organization of living matter". In: *Science* 200.4345, pp. 1012–1018.

Tang, Zhiyong et al. (2006). "Self-assembly of CdTe nanocrystals into free-floating sheets". In: *Science* 314.5797, pp. 274–278.

Tatum, John P and Robert C Wright (1988). *Organoclay materials*. US Patent 4,752,342.

Thompson, Russell B et al. (2002). "Block copolymer-directed assembly of nanoparticles: Forming mesoscopically ordered hybrid materials". In: *Macromolecules* 35.3, pp. 1060–1071.

Tkalec, U et al. (2009). "Vortexlike topological defects in nematic colloids: chiral colloidal dimers and 2D crystals". In: *Physical review letters* 103.12, p. 127801.

Torrie, GM and JP Valleau (1982). "Electrical double layers. 4. Limitations of the Gouy-Chapman theory". In: *The Journal of Physical Chemistry* 86.16, pp. 3251–3257.

Traube, J (1925). "Konzentrierung von kautschukmilchsften". In: *Gummi Zeitung* 434.

Tuinier, R. et al. (2008). "Phase diagram for a mixture of colloids and polymers with equal size". In: *EPL (Europhysics Letters)* 82.June, p. 68002. ISSN: 0295-5075. DOI: 10.1209/0295-5075/82/68002.

Turberfield, Andrew (2003). "DNA as an engineering material". In: *Physics World* 16.3, p. 43.

Turner, MS and ME Cates (1990). "The relaxation spectrum of polymer length distributions". In: *Journal de Physique* 51.4, pp. 307–316.

Umar, Ahmad, Sang Hoon Kim, and Yoon-Bong Hahn (2008). "Formation of hierarchical ZnO nanostructures "nanocombs": Growth mechanism, structural and optical properties". In: *Current Applied Physics* 8.6, pp. 793–797.

Van Der Schoot, P and ME Cates (1994). "The isotropic-to-nematic transition in semiflexible micellar solutions". In: *EPL (Europhysics Letters)* 25.7, p. 515.

Van Workum, Kevin and Jack F Douglas (2006). "Symmetry, equivalence, and molecular self-assembly". In: *Physical Review E* 73.3, p. 031502.

Verlet, Loup and Jean-Jacques Weis (1972). "Equilibrium theory of simple liquids". In: *Physical Review A* 5.2, p. 939.

Verwey, Evert Johannes Willem, J Th G Overbeek, and Jan Theodoor Gerard Overbeek (1999). *Theory of the stability of lyophobic colloids*. Courier Corporation.

Vincent, Brian (2012). *Early (pre-DLVO) studies of particle aggregation*. DOI: 10.1016/j.cis.2011.12.003.

Vrij, A (1976). "Polymers at interfaces and the interactions in colloidal dispersions". In: *Pure and Applied Chemistry* 48.4, pp. 471–483.

Vyborna, Yuliia et al. (2017). "Morphological diversity of supramolecular polymers of DNA-containing oligopyrenes–formation of chiroptically active nanosheets". In: *Chemical Communications* 53.89, pp. 12128–12131.

Wang, Cuiqing, Dairong Chen, and Xiuling Jiao (2009). "Lyotropic liquid crystal directed synthesis of nanostructured materials". In: *Science and technology of advanced materials* 10.2, p. 023001.

Wang, Ke et al. (2005). "Epoxy nanocomposites with highly exfoliated clay: mechanical properties and fracture mechanisms". In: *Macromolecules* 38.3, pp. 788–800.

Wang, Y Z et al. (2010). "Universal scaling description of the strain-softening behavior in the semidilute uncross-linked polyacrylamide-water solution". In: *Soft Matter* 6.14, pp. 3318–3324. DOI: 10.1039/C001342K. URL: http://dx.doi.org/10.1039/C001342K.

Wang, Zhong Lin (2013). *Nanowires and nanobelts: materials, properties and devices. Volume 1: Metal and Semiconductor Nanowires*. Springer Science & Business Media.

Whitesides, G. M. (2002). "Self-Assembly at All Scales". In: *Science* 295.5564, pp. 2418–2421. ISSN: 00368075. DOI: 10.1126/science.1070821. arXiv: arXiv:1011.1669v3. URL: http://www.sciencemag.org/cgi/doi/10.1126/science.1070821.

Whitesides, George M, John P Mathias, and Christopher T Seto (1991). "Molecular self-assembly and nanochemistry: a chemical strategy for the synthesis of nanostructures". In: *Science* 254.5036, pp. 1312–1319.

Whitmer, Jonathan K et al. (2013a). "Liquid-crystal mediated nanoparticle interactions and gel formation". In: *The Journal of chemical physics* 138.19, p. 194903.

Whitmer, Jonathan K et al. (2013b). "Nematic-field-driven positioning of particles in liquid crystal droplets". In: *Physical review letters* 111.22, p. 227801.

Wolf-Gladrow, Dieter A (2004). *Lattice-gas cellular automata and lattice Boltzmann models: an introduction*. Springer.

Wood, W Wo and JD Jacobson (1957). "Preliminary results from a recalculation of the Monte Carlo equation of state of hard spheres". In: *The Journal of Chemical Physics* 27.5, pp. 1207–1208.

Xu, Nuoxin et al. (2017). "In-situ preparation of hierarchical flower-like TiO2/carbon nanostructures as fillers for polymer composites with enhanced dielectric properties". In: *Scientific Reports* 7, p. 43970.

Xu, Qiang (2013). *Nanoporous materials: synthesis and applications*. CRC Press.

Y Gao Q Guo, Y Guo P Wu W Meng T Jia (2017). "Investigation on Reinforced Mechanism of Fiber Reinforced Asphalt Concrete Based on Micromechanical Modeling". In: *Advances in Materials Science and Engineering*. DOI: 10.1155/2017/4768718. URL: https://doi.org/10.1155/2017/4768718.

Yakovlev, Dmitry S and Edo S Boek (2007). "Molecular dynamics simulations of mixed cationic/anionic wormlike micelles". In: *Langmuir* 23.12, pp. 6588–6597.

Yamakawa, Hiromi (1971). *Modern theory of polymer solutions*. Harper & Row.

Ying, Jackie Y, Christian P Mehnert, and Michael S Wong (1999). "Synthesis and applications of supramolecular-templated mesoporous materials". In: *Angewandte Chemie International Edition* 38.1-2, pp. 56–77.

Yodh, a. G. et al. (2001). "Entropically driven self-assembly and interaction in suspension". In: *Philosophical Transactions of the Royal Society A: Mathematical, Physical and Engineering Sciences* 359.1782, pp. 921–937. ISSN: 1364-503X. DOI: 10.1098/rsta.2000.0810. URL: http://rsta.royalsocietypublishing.org/content/359/1782/921.

Zaccarelli, Emanuela et al. (2008). "Gelation as arrested phase separation in short-ranged attractive colloid–polymer mixtures". In: *Journal of Physics: Condensed Matter* 20.49, p. 494242.

Zapotocky, Martin et al. (1999). "Particle-stabilized defect gel in cholesteric liquid crystals". In: *Science* 283.5399, pp. 209–212.

Zeng, Q.H., A.B. Yu, and G.Q. Lu (2008). "Multiscale modeling and simulation of polymer nanocomposites". In: *Progress in Polymer Science* 33.2, pp. 191–269. ISSN: 00796700. DOI: 10.1016/j.progpolymsci.2007.09.002. URL: http://linkinghub.elsevier.com/retrieve/pii/S0079670007001049.

Zerda, Adam S and Alan J Lesser (2001). "Intercalated clay nanocomposites: morphology, mechanics, and fracture behavior". In: *Journal of Polymer Science Part B: Polymer Physics* 39.11, pp. 1137–1146.

Zhang, Mingfu, Markus Drechsler, and Axel HE Müller (2004). "Template-controlled synthesis of wire-like cadmium sulfide nanoparticle assemblies within core- shell cylindrical polymer brushes". In: *Chemistry of materials* 16.3, pp. 537–543.

Zhang, Tian Hui and Xiang Yang Liu (2014). "Experimental modelling of single-particle dynamic processes in crystallization by controlled colloidal assembly". In: *Chem. Soc. Rev.* 43.7, pp. 2324–2347. DOI: 10.1039/C3CS60398A. URL: http://dx.doi.org/10.1039/C3CS60398A.

Zhang, Zhenli and Sharon C Glotzer (2004). "Self-assembly of patchy particles". In: *Nano Letters* 4.8, pp. 1407–1413.

Zhao, Xiu S., G. Q. (Max) Lu, and Graeme J. Millar (1996). "Advances in Mesoporous Molecular Sieve MCM-41". In: *Industrial & Engineering Chemistry Research* 35.7, pp. 2075–2090. ISSN: 0888-5885. DOI: 10.1021/ie950702a. URL: http://pubs.acs.org/doi/abs/10.1021/ie950702a.

Zhou, Chunfeng, Pengtao Yue, and James J Feng (2008). "Dynamic simulation of droplet interaction and self-assembly in a nematic liquid crystal". In: *Langmuir* 24.7, pp. 3099–3110.

Zoeller, Nancy, Leo Lue, and Daniel Blankschtein (1997). "Statistical-thermodynamic framework to model nonionic micellar solutions". In: *Langmuir* 13.20, pp. 5258–5275.